Ignition of Ionic Liquids (Volume 2)

Ghanshyam Vaghjiani
Steve Chambreau (ERC)

AFRL/RZSP
10 E. Saturn Blvd.
Edwards AFB, CA 93524-7680

Final Report

September 2010

**AIR FORCE RESEARCH LABORATORY
PROPULSION DIRECTORATE**

■ **Air Force Materiel Command**   ■ **United States Air Force**   ■ **Edwards Air Force Base, CA 93524**

UNCLASSIFIED

NOTICE AND SIGNATURE PAGE
(STINFO COPY)

Qualified requestors may obtain copies of this report from the Defense Technical Information Center (DTIC) (http://www.dtic.mil).

AFRL-RZ-ED-TR-2010-0048 HAS BEEN REVIEWED AND IS APPROVED FOR PUBLICATION IN ACCORDANCE WITH ASSIGNED DISTRIBUTION STATEMENT.

FOR THE DIRECTOR:

/ s /   / s /

_____   _____
WAYNE M. KALLIOMAA   LATRAVIA R. DOBSON, Capt, USAF
Project Manager   Chief
 Propellants   Branch
              / s /

_____
ROBERT C. CORLEY
Technical Advisor
Space and Missile Propulsion Division

This report is published in the interest of scientific and technical information exchange, and its publication does not constitute the Government's approval or disapproval of its ideas or findings.

REPORT DOCUMENTATION PAGE

Form Approved
OMB No. 0704-0188

Public reporting burden for this collection of information is estimated to average 1 hour per response, including the time for reviewing instructions, searching existing data sources, gathering and maintaining the data needed, and completing and reviewing this collection of information. Send comments regarding this burden estimate or any other aspect of this collection of information, including suggestions for reducing this burden to Department of Defense, Washington Headquarters Services, Directorate for Information Operations and Reports (0704-0188), 1215 Jefferson Davis Highway, Suite 1204, Arlington, VA 22202-4302. Respondents should be aware that notwithstanding any other provision of law, no person shall be subject to any penalty for failing to comply with a collection of information if it does not display a currently valid OMB control number. **PLEASE DO NOT RETURN YOUR FORM TO THE ABOVE ADDRESS.**

1. REPORT DATE *(DD-MM-YYYY)* September 2010	2. REPORT TYPE In-House Final Report (Vol 2 of 2)	3. DATES COVERED *(From - To)* 29 Oct 2003 – 30 Sep 2010
4. TITLE AND SUBTITLE Ignition of Ionic Liquids (Volume 2)		**5a. CONTRACT NUMBER**
		5b. GRANT NUMBER
		5c. PROGRAM ELEMENT NUMBER 61102F
6. AUTHOR(S) Vaghjiani, Ghanshyam; Chambreau, Steve		**5d. PROJECT NUMBER**
		5e. TASK NUMBER
		5f. WORK UNIT NUMBER 23030423
7. PERFORMING ORGANIZATION NAME(S) AND ADDRESS(ES) Air Force Research Laboratory (AFMC) AFRL/RZSP 10 E. Saturn Blvd. Edwards AFB CA 93524-7680		**8. PERFORMING ORGANIZATION REPORT NO.**
9. SPONSORING / MONITORING AGENCY NAME(S) AND ADDRESS(ES) Air Force Research Laboratory (AFMC) AFRL/RZSP 10 E. Saturn Blvd Edwards AFB CA 93524-7680		**10. SPONSOR/MONITOR'S ACRONYM(S)**
		11. SPONSOR/MONITOR'S REPORT NUMBER(S) **AFRL-RZ-ED-TR-2010-0048**

12. DISTRIBUTION / AVAILABILITY STATEMENT
Approved for public release; distribution unlimited. Public Affairs # 10694.

13. SUPPLEMENTARY NOTES

14. ABSTRACT
This report summarizes the experimental and theoretical research effort undertaken to study and identify some of the chemical pathways involved in the hypergolic ignition of mixtures consisting of room temperature ionic liquids (ILs) and suitable oxidizers such as nitric acid. Our aim in this work was to provide accurate mechanistic data on recently discovered hypergolic ILs that can be used to build a chemical kinetics ignition model to simulate the ignition delay time, a quantity of significant imiportance in the design and implementation of hypergolic rocket engines. The mechanistic information can also be used for developing reactive molecular dynamics models and correlation algorithms to create "first-principle" design tools to predict new hypergolic combinations prior to any effort to synthesize the fuel molecules. Availability of such computational tools would provide a mitigation strategy for the risks (cost and time) currently involved in the trial-and-error approach to first synthesize the IL and then test it to verify its behavior. An added feature of hypergolic IL fuels is their inherent low vapor pressures. Implementation of such fuels would result in lowering of vapor toxicity exposures and reduction in emissions to the environment. Consequently, fielding of such "green" IL fuels in future propulsion systems will provide significant logistical, operational and supportability cost savings to the DoD.

15. SUBJECT TERMS
Energetic ionic liquids; ionic molecular structure; energetic heterocycles; cations; anions

16. SECURITY CLASSIFICATION OF:			17. LIMITATION OF ABSTRACT	18. NUMBER OF PAGES	19a. NAME OF RESPONSIBLE PERSON Wayne Kalliomaa
a. REPORT **Unclassified**	**b. ABSTRACT** **Unclassified**	**c. THIS PAGE** **Unclassified**	SAR	55	**19b. TELEPHONE NO** *(include area code)* 661 275-6442

Standard Form
298 (Rev. 8-98)
Prescribed by ANSI
Std. 239.18

This Page Intentionally Left Blank

TABLE OF CONTENTS

LIST OF FIGURES

Figure No.   **Page No.**

LIST OF TABLES

GLOSSARY

AFRL	Air Force Research Laboratory
ALS	Advanced Light Source (facility)
ATR	attenuated total refelection
CN	carbon-nitrogen
DNB	1,5-dinitrobiuret
DoD	Department of Defense
EOARD	European Office of Aerospace Research and Development
FTIR	Fourier Transform Infrared
ID	ignition delay
IHPRPT	Integrated High Payoff Rocket Propulsion Technology
IL	ionic liquid
IR	infrared
IRC	intrinsic reaction coordinate
MD	molecular dynamics
PE	potential energy
PIE	photoionization efficiency
RRKM	Rice-Ramsperager-Kassel-Marcus
TOFMS	time-of-flight-mass-spectrometry
TS	transition state
VUV	vacuum ultraviolet
ZPE	zero-point energy

This Page Intentionally Left Blank

1.0 EXECUTIVE SUMMARY

This report summarizes the experimental and theoretical research effort undertaken to study and identify some of the chemical pathways involved in the hypergolic ignition of mixtures consisting of room temperature ionic liquids (ILs) and suitable oxidizers such as nitric acid. Hypergolicity is defined as the auto-ignition of a binary chemical system under ambient conditions of pressure and temperature. The research was motivated by the recognition that higher performing hypergolic propellants need to be developed to meet future DoD space propulsion capabilities as outlined in the IHPRPT (Integrated High Payoff Rocket Propulsion Technology) Program. The popularity of ILs as a class of energetic substances for DoD applications arises from the fact that a combination of different anions and cations in the IL will lead to a large (~10^8) number of compounds with tailorable physical and thermochemical properties. While many physical and thermodynamic properties of propellants are now being predicted theoretically with reasonable reliability using quantum *ab initio* computations and molecular dynamics simulations, the same is not true for *a priori* predictions of hypergolic reactivity. Our aim in this work was to provide accurate mechanistic data on recently discovered hypergolic ILs that can be used to build a chemical kinetics ignition model to simulate the ignition delay time, a quantity of significant importance in the design and implementation of hypergolic rocket engines. The mechanistic information can also be used for developing reactive molecular dynamics models and correlation algorithms to create "first-principle" design tools to predict new hypergolic combinations prior to any effort to synthesize the fuel molecules. Availability of such computational tools would provide a mitigation strategy for the risks (cost and time) currently involved in the trial-and-error approach to first synthesize the IL and then test it to verify its behavior. An added feature of hypergolic IL fuels is their inherent low vapor pressures. Implementation of such fuels would result in lowering of vapor toxicity exposures and reduction in emissions to the environment. Consequently, fielding of such "green" IL fuels in future propulsion systems will provide significant logistical, operational and supportability cost savings to the DoD.

The details of our findings can be found in Appendix A[1-4] and in various publications[5-8] as well as in symposia proceedings.[9-11] Below is a brief synopsis of ongoing unpublished work.

2.0 THEORETICAL EFFORT
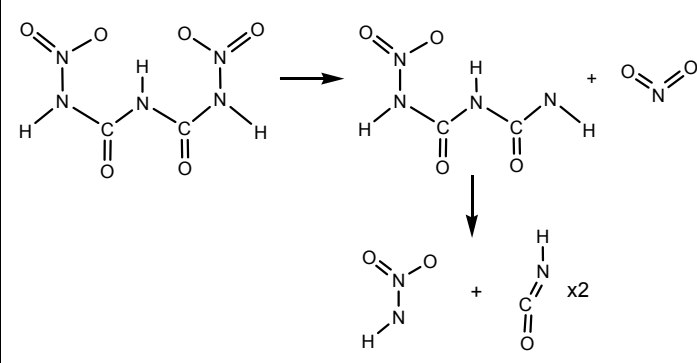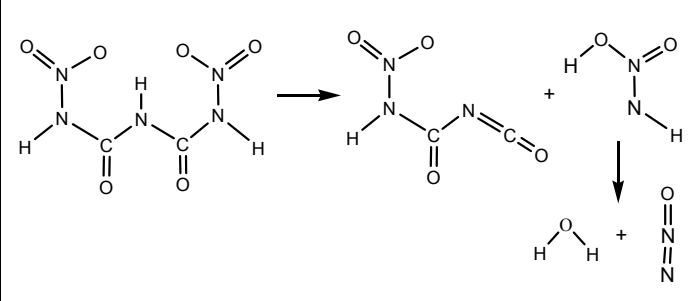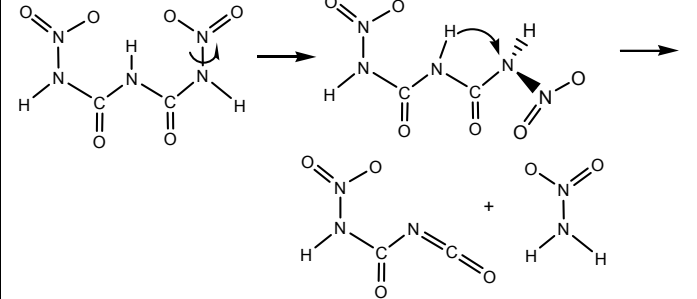
2.1 Direct Dynamics Trajectory Studies

Based on experimental investigations of the end product analysis, a possible reaction mechanism, involving the 1,5-dinitrobiuret (DNB) intermediate, in the hypergolic ignition of dicyanamide-based ILs and nitric acid system was published.[1] To further understand the chemistry of this nitrogen-rich explosive compound, *ab initio* electronic structure calculations and direct dynamics simulations were carried out to map the reaction coordinates for decomposition of DNB, including energies and structures of all stationary points (i.e., intermediate complexes, transition states (TSs), and products). For complex molecules, especially for those with high internal energy content, the use of chemical intuition to predict reaction paths is unreliable. There may be concerted reactions that are difficult to predict, and once energy stored in the molecule begins to release, the system does not necessarily follow the minimum energy reaction path, i.e., the

subsequent behavior is controlled by dynamics. Even for steps in the reaction that are controlled by statistical factors, standard transition state locating methods may be difficult to apply, because the molecular transformations are too complex. A useful approach to treating such a system is quasi-classical, direct dynamics trajectory simulations, where the motion of the molecule is followed, allowing the molecule to "show us" what the preferred reaction paths are. The direct dynamics method dispenses with the potential energy surface. Instead, it calculates the energies, force constants, and Hessian "on the fly" using *ab initio* methods. This method becomes computationally attractive when the dimensionality of the system increases, particularly for the DNB molecule which contains 13 heavy atoms. Dynamics simulations partition the energy generated by the exothermic reaction to vibrational, rotational a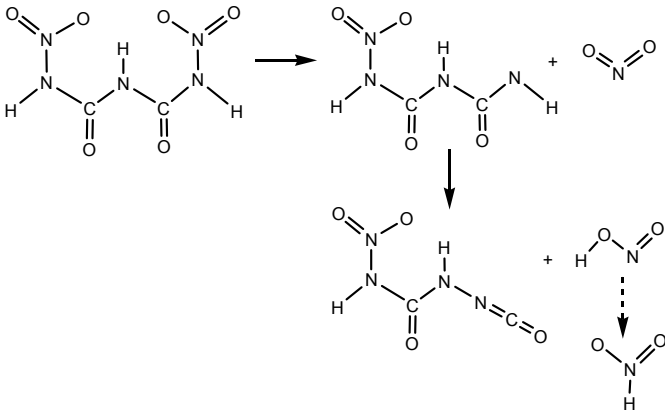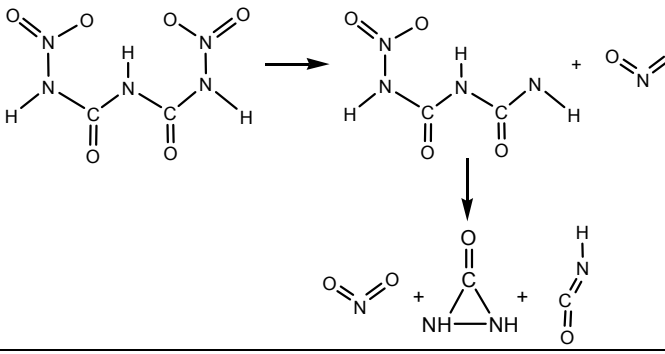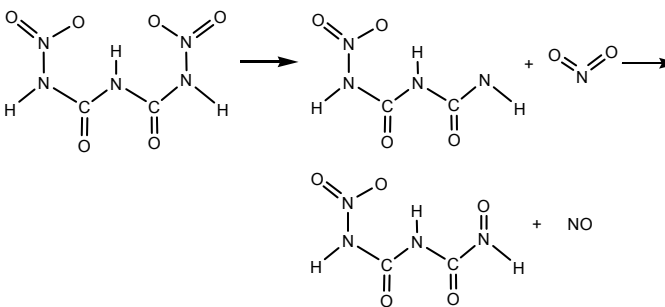nd translational modes, increasing the chance of locating new reaction paths. In addition, by following the variation of the potential energy during the trajectory rather than relying on intuition, we can identify better geometries for TS searching.

In this study, direct dynamics trajectory simulations were conducted for two purposes: 1) examining decomposition behavior of DNB at various temperatures and discovering new decomposition paths; and 2) locating key transition states for the dissociation paths identified in dynamics simulations, when the standard TS-searching methods (i.e., TS, QST2, and QST3 methods in Gaussian 03[12]) fail. Trajectory simulations were started at the equilibrium geometry of DNB. A general chemical dynamics program VENUS[13] was used to set up the trajectory initial conditions, and the Bakken Hessian-based method implemented in Gaussian 03 was used to propagate each trajectory with Hessians recalculated every five steps. The integrators were performed with a step size of ~ 0.4 fsec, which conserved total energy to better than 10^{-4} Hartree. The scf = xqc option was used during trajectory integration so that a quadratically convergent Hartree-Fock (qc-scf) method was used in case the usual, but much faster scf method did not converge within the allotted number of cycles. B3LYP/6-31G* level of theory was chosen for the main set of trajectories. For most of the trajectories calculated in the vibrational temperature range 4000-6000 K, the time at which the DNB began to dissociate was between 0.5 and 3 psec, which is much longer than the periods of most DNB vibrational modes. At a vibrational temperature of 4000 K, 10% of trajectories maintain the original molecular structure before trajectory termination. The dissociative trajectories can be grouped into six classes, as illustrated in Table 1.

Table 1. Direct Dynamics Simulation Results for Thermal Decomposition of DNB

Dissociation Channels	ΔH [a] /eV	Barrier of possible TS / eV	Branching % [b]		
			4000K	5000K	6000K
Path 1: note: some trajectories dissociate simultaneously	1.81 2.72	TS1, 0.63	36	41	37
Path 2:	1.15 -0.59	TS2, 1.22	24	12	7
Path 3:	0.66	TS3, 0.36 (TS3 corresponds to twisting CN bond before H-transfer)	10	3	3

Table 1. continued.

Dissociation Channels	ΔH [a] /eV	Barrier of possible TS / eV	Branching % [b]		
			4000K	5000K	6000K
Path 4:	1.81				
	0.97		8	7	3
Path 5:	1.81				
	3.23		6	17	30
Path 6:	1.81				
	0.98		-	5	-
Non-reactive within 4 psec simulation period	0		10	-	-
Sum of other minor dissociation paths	-		6	15	20

[a]Values of ΔH were calculated relative to DNB at the B3LYP/6-31G* level of theory.
[b]Branching ratios were calculated based on 50, 60 and 30 trajectories simulated at 4000, 5000, and 6000 K, respectively.

Ab initio electronic structure calculations were performed at the B3LYP/6-31G* level of theory, using the Gaussian 03 suite of programs. Geometries were optimized by calculating the force constants at every step. Vibrational frequencies and zero-point energies (ZPEs) were scaled by a factor of 0.9613 and 0.9804, respectively, and when necessary intrinsic reaction coordinate (IRC) calculations were used to determine which minima are connected by particular TSs. All transition states found were verified to be first-order saddle points by frequency calculation. Optimized geometries of DNB and various dissociation products identified in the direct dynamics simulations are depicted in Fig. 1, and those of transition states for the three major dissociation paths are depicted in Fig. 2.
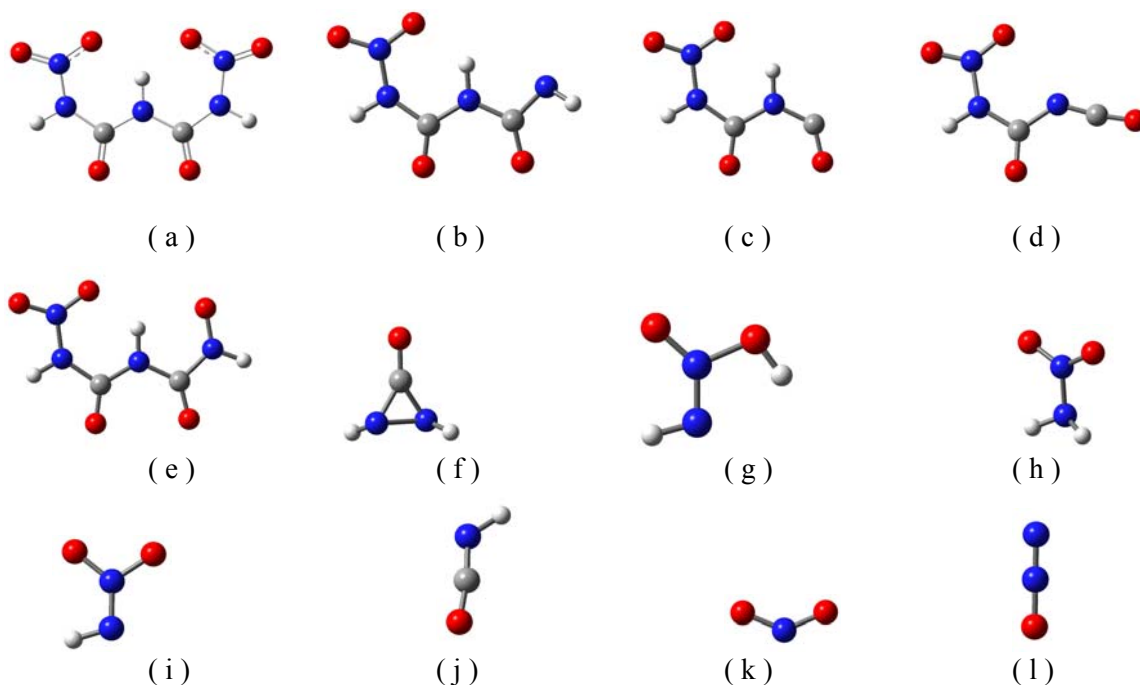
Fig. 1: B3LYP/6-31G* optimized geometries of the reactant and products identified in trajectory simulations: a) DNB, b) O$_2$N-NHCO-NHCO-NH, c) O$_2$N-NHCO-NHCO, d) O$_2$N-NHCO-NCO, e) O$_2$N-NHCO-NHCO-NO-H, f) cyclic [HN-CO-NH], g) HNN(OH)O, h) H$_2$NNO$_2$, i) HNNO$_2$, j) HNCO, k) NO$_2$, and l) N$_2$O.

TS1   TS2   TS3
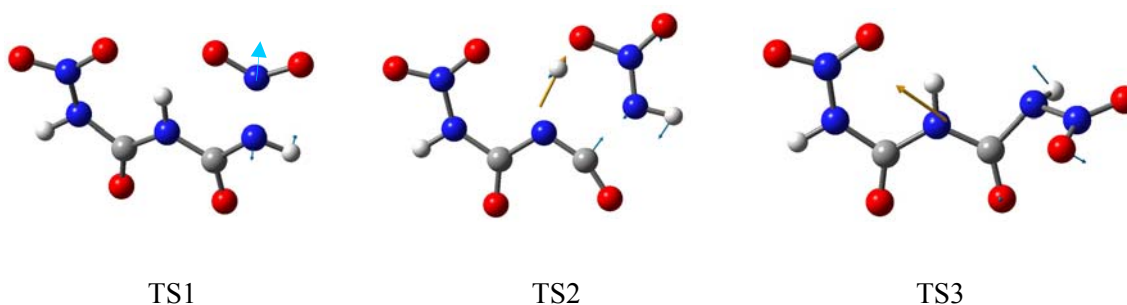
Fig. 2: B3LYP/6-31G* optimized geometries of transition states. Vibrational modes corresponding to the imaginary frequencies were indicated by displacement vectors.

By far the most common outcome of DNB decomposition is Path 1, where elimination of NO_2 occurs first, followed by sequential dissociation of the remaining unit to isocyanic acid HNCO and $HNNO_2$. A typical Path 1 trajectory (calculated at 4000 K vibrational temperature) is illustrated in Fig. 3, showing the change of potential energy (PE) during the trajectory. The oscillations in the PE reflect the vibration of the DNB molecule, including ZPE. The trajectory shows three dissociation steps, eliminating NO_2 followed by elimination of two HNCO molecules. Elimination of NO_2 occurs at ~ 150 fsec, and the time for which the decomposition lasts is ~ 650 fsec.
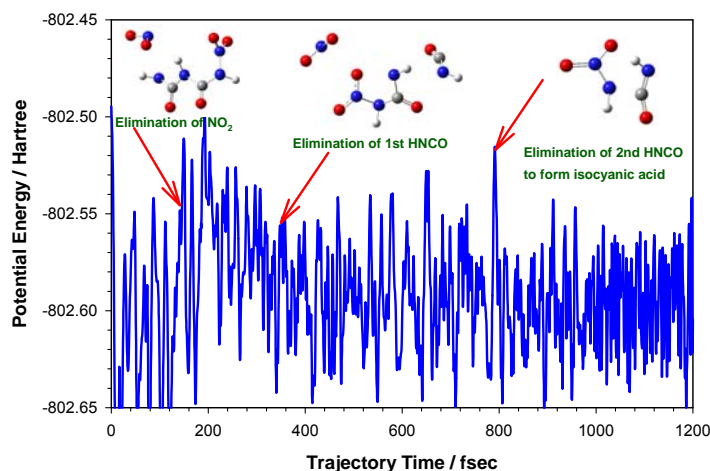
Fig. 3: A representative trajectory of dissociation Path 1 at 4000 K, simulated at B3LYP/6-31G*. Plot shows the variation of potential energy during the trajectory, and three dissociation steps are indicated.

In Path 2, HNN(OH)O is produced via an intra-molecular hydrogen atom transfer followed by dissociation of an amide bond. HNN(OH)O further decomposes to N_2O and water. A trajectory

representative of dissociation Path 2 is illustrated in Fig. 4, indicating two energy barriers associated with two activated dissociation steps.
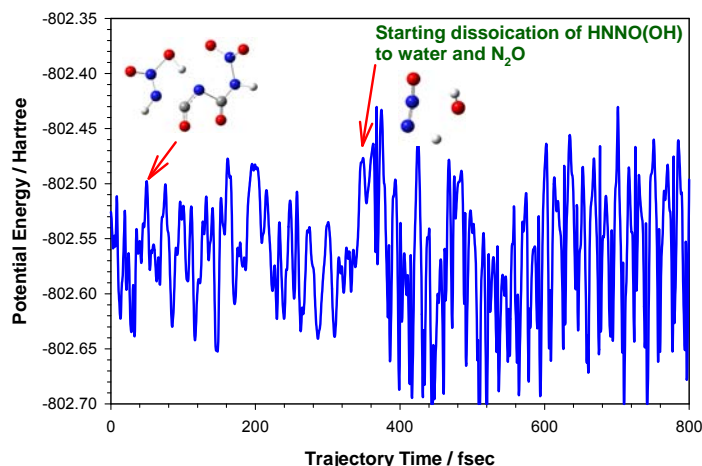
Fig. 4: A representative trajectory of dissociation Path 2 at 4000 K, calculated at B3LYP/6-31G*. Plot shows two dissociation steps and the variation of potential energy during the trajectory.

The other common dissociation channel is Path 3 where DNB first twists along a CN bond through TS3 (see Fig. 2), then undergoes an intra-molecular hydrogen atom transfer (i.e., transfer of an H-atom from the central nitrogen atom to the neighboring N) followed by elimination of H_2NNO_2 (Fig. 5). This decomposition path was proposed in the literature[1] based on our experimental products analysis. Alternatively, DNB could first decompose to O_2N-NHCO-NHCO and $HNNO_2$, then subsequently undergo an inter-molecular hydrogen atom transfer between two fragments to produce nitramide. However, this path involves breaking a CN bond with an energy barrier of at least 3.90 eV, and thus is energetically unfavorable.
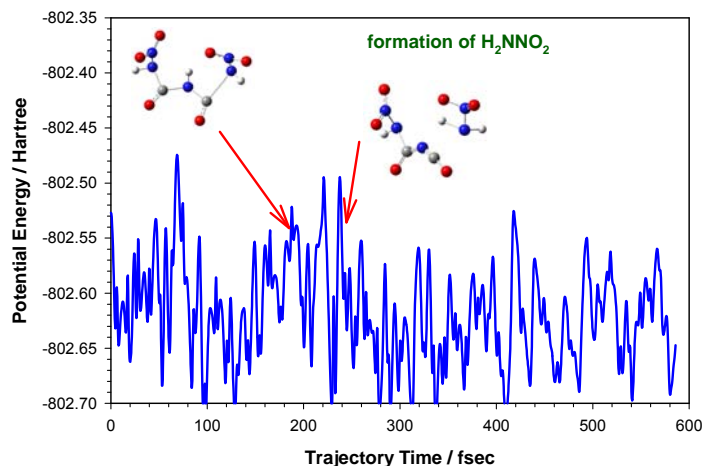
Fig. 5: A representative trajectory of dissociation Path 3 at 4000 K, calculated at B3LYP/6-31G*. Plot shows two activated steps and the variation of potential energy during the trajectory.

A transition-state-theory-based statistical model, Rice-Ramsperager-Kassel-Marcus (RRKM) theory was applied to examine the properties of the reactant and transition states as a function of the internal temperature. RRKM dissociation rates for initial decomposition for the various paths are shown in Table 2 for temperatures ≤ 1500 K. RRKM calculations predict that, at temperatures below 1000 K, Paths 1 and 2 are negligible due to the high and tight transition states; only formation of H_2N-NO would be expected. At 1500 K (i.e., the maximum DNB denotation temperature), decomposition is still dominated by Path 3 but the contribution of Path 1 becomes significant. Note that the calculated TS3 corresponds to the first step of decomposition Path 3, i.e., twist of the O_2N-NH unit before H transfer (see Fig. 2 and Table 1). We were unable to locate other TSs associated with the following intra-molecular H transfer. Therefore, the RRKM predicted reaction rate for Path 3 is an *upper limit*. Assuming that these three decomposition paths account for most DNB dissociation at temperatures less than 1500 K, the product branching ratios can be estimated using the RRKM rates. It turns out that Path 3 accounts for more than 80% of DNB decomposition at 1500 K.

Table 2. Calculated RRKM dissociation rates and branching ratios for DNB[*]

Temperature	500 K		1000 K		1500 K	
	$k\ (s^{-1})$	branching	$k\ (s^{-1})$	branching	$k\ (s^{-1})$	branching
Path 1	0	0	9.2×10^8	0.03	2.8×10^{10}	0.18
Path 2	0	0	1.0×10^5	~0	5.5×10^8	~ 0
Path 3	5.1×10^7	0.01	2.6×10^{10}	0.07	1.3×10^{11}	0.82

[*]The branching ratios were estimated when only three major dissociation paths were included.

The present work demonstrates that dynamics simulations, in conjunction with electronic structure and RRKM calculations, are able to help extract decomposition mechanisms and dynamics of complex energetic molecules, product branching ratios, and how they vary with temperature. The trajectories have been found to reproduce the major decomposition products of DNB observed in the pyrolysis experiment.[14] The trajectories revealed many different dissociation paths. According to RRKM analysis, at least two of these paths, i.e., elimination of NO_2 and formation of nitramide, are important in the denotation/hypergolic experiments. In conclusion, these results, several of which were difficult to anticipate in advance, demonstrate the utility of direct dynamics trajectory simulations as a useful and necessary step for investigating the decomposition mechanism and dynamics of complex molecular dissociation, and constructing kinetics models.[15]

For the future, it would be useful to carry out further trajectory simulations on the subsequent dissociation of remaining units (such as $O_2N-NHCO-NHCO-NH$ and $O_2N-NHCO-NCO$) generated in the initial decomposition in order to get a complete picture of DNB decomposition.

2.2 Chemical Kinetics Modeling

Our FTIR spectroscopic measurements[1] in dicyanamide-based ILs and nitric acid systems showed the formation of HNCO, HNO_3, N_2O, NO_2, CO_2 and H_2O as major pre-ignition products. Thermodynamic equilibrium calculations on various mixtures of these species were carried out to verify that such mixtures can sustain a flame under ambient experimental conditions. To further investigate which chemical pathways control the hypergolic ignition process in these mixtures, the thermal decomposition of HNCO, HNO_3 and N_2O was written in detail to explicitly account for all of the subsequent reactions of the species produced and their corresponding rate constants specified from available thermo-kinetics databases. The detailed chemical kinetics model constructed consisted of 61 species and 377 reactions and was implemented into SENKIN.[16] The fate of various homogeneously premixed $HNCO/CO_2/H_2O/N_2O/HNO_3/NO_2$ gaseous mixtures was simulated. The model was able to simulate ignition at relatively low temperatures.[8] As shown in Fig. 6, for a mixture at a constant volume and at an initial temperature of 480 K and initial pressure of 1 atmosphere, an ignition delay (ID) of 19 s was predicted. Here, ignition is numerically defined as the time delay in the system at which point the temperature profile has reached a value of 50% of the maximum. For the composition considered in Fig. 6, sensitivity analysis showed that the presence of NO_2 in the system had a significant effect on the predicted value of the ignition delay. Brute-force sensitivity analysis suggested that the reaction, $HNO_3 \rightarrow OH + NO_2$, is an important source for NO_2 in the system. Typically, detailed chemical kinetics models are validated against measured experimental parameters such as ignition delays, species profiles, and fundamental flame speeds that are obtained under "ideal" laboratory setups with homogeneous mixtures at known conditions of temperature and pressure. However, for hypergolic systems, as is the case here, it is very difficult to determine the precise experimental composition, pressure and temperature of the gas phase in which ignition is observed due to the inherent inhomogeneity of the transiently formed mixtures, and therefore it is not easy to validate the detailed chemical kinetics model under consideration. Even in the case for premixed homogeneous systems, such a validation effort in many circumstances is not trivial. The present detailed chemical kinetics model to predict

ignition delays in ILs is the first of its kind. Although the predictions are off by 2 orders of magnitude, the present effort represents a valuable initial step towards understanding hypergolicity in IL/HNO$_3$ systems.
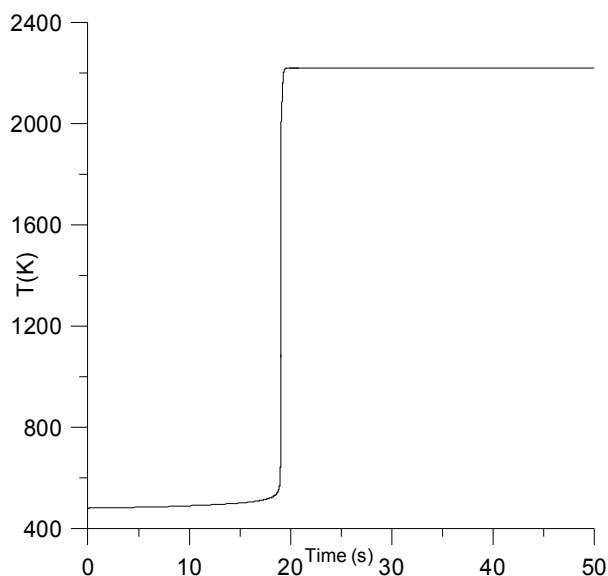
Fig. 6: Computed temperature profile against time for the mixture HNCO/NO$_2$/N$_2$O/CO$_2$/H$_2$O/HNO$_3$: 1/1/2/1/1/1. The system is considered adiabatic and at constant volume. P = 1 atm, T = 480 K, ignition delay: 19 s.

Future refinements to the model will be carried out through an EOARD grant. This will include a comprehensive sensitivity analysis both to construct a reduced-kinetics model as well as to include experimentally determined new reaction paths and mechanistic information regarding NO$_2$ kinetics. Methods to implement the reduced-kinetics model into a computational fluid code, such as FLUENT, will be explored. Techniques to validate the resulting model against realistic experimental parameters that describe transient composition, pressure, and temperature profiles during hypergolic ignition of IL/HNO$_3$ mixtures will be assessed. The ultimate capability we seek in this modeling and simulation effort is the ability to accurately predict ID times in known IL/oxidizer combinations as well as to be able to numerically identify hitherto unknown hypergol combinations.

<p style="text-align:center">3.0 EXPERIMENTAL EFFORTS</p>

3.1 FTIR Spectroscopic Investigations

To understand the initiation processes that occur in the condensed phase during the reaction of an IL with various oxidizers, transmission FTIR spectroscopic investigations were performed to elucidate how the oxidizer initially ionizes upon contact with the IL. Subsequent reactions of these ionized species with the ionic components of the IL were followed by recording the temporal behavior of the IR absorptions of the IL in the condensed phase.

Experiments were performed by preparing a thin-film of the IL on a Ge disc and exposing it to an excess of the oxidizing gas under anhydrous conditions. Simple ionization of both NO_2 ($\leftrightarrow$ $\frac{1}{2}N_2O_4$) and HNO_3, respectively, to $NO^+ + NO_3^-$ and $H^+ + NO_3^-$ was observed to occur at the ionic surface as seen in Fig. 7. Transient formation of NO^+ was inferred from FTIR observation of the N_2O product when the ionic liquid, $R^+N_3^-$ was treated with N_2O_4, where the reaction $N_3^- + NO^+$ leads to $N_2O + N_2$ formation.

The difference in the heterogeneous chemistry of NO_2 and HNO_3 towards a thin-film of 1-butyl-3-methyl-imidazolium dicyanamide ($BMIM^+N(CN)_2^-$) is shown, respectively, in Figs. 8 and 9. The spectrum of unreacted $BMIM^+N(CN)_2^-$ (blue trace, Figure 8) is shown with characteristic $N(CN)_2^-$ fundamental and combination bands identified. These bands disappear upon reaction of $BMIM^+N(CN)_2^-$ with gaseous NO_2 (red trace, Figure 8), providing direct spectroscopic confirmation that the anion initiates the reaction with the oxidizing species. All of the cationic bands in the blue trace are also present in the red trace, and in addition, the appearance of new product bands is noted. This suggests that the IL-cation merely acts as a spectator during initiation, until after ignition has occurred, whereupon it would then participate in further high temperature oxidative processes during steady-state combustion of the IL.
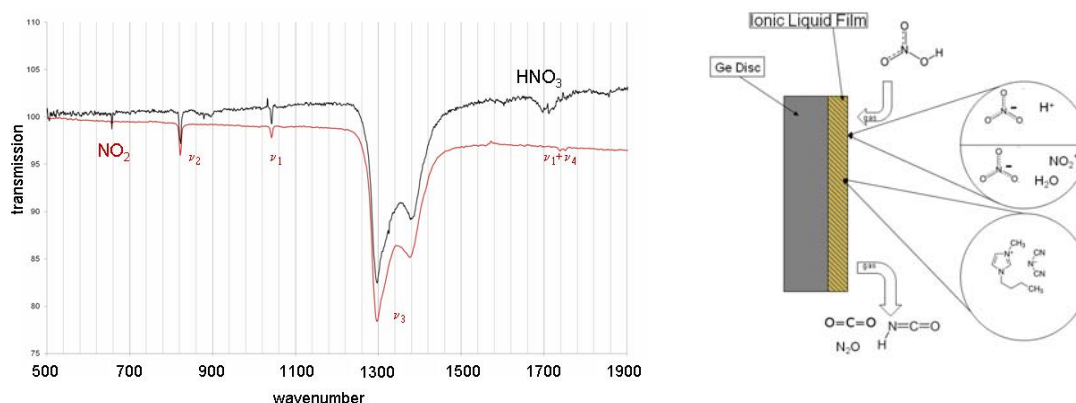

Fig. 7: NO_3^- absorption bands in the ionization of NO_2 (red) and HNO_3 (black) at an IL surface.

The product spectrum of $BMIM^+N(CN)_2^-$ after exposure to gaseous HNO_3 (purple trace in Fig. 9) also indicates that the anion is initially involved in the reaction. However, different product bands are noted in this trace compared to that in the red trace of Fig. 8. Comparison to the experimentally recorded biuret spectrum suggests that amide-III like features (peaks 19 and 20) are also present in this product spectrum (peaks 32, 35, and 36). Characteristic features of N-H stretching in the purple trace were also noted.
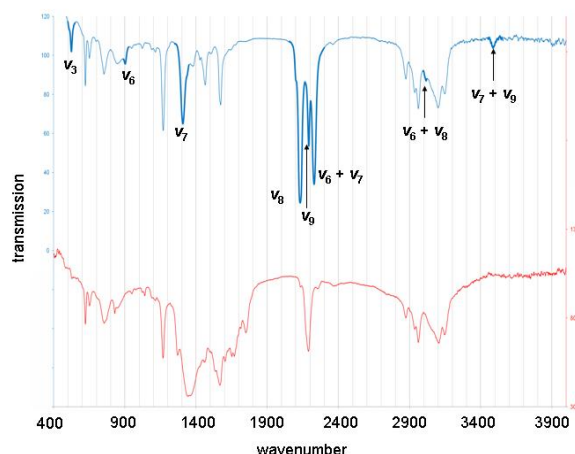
Fig. 8: Spectrum of neat thin-film of BMIM$^+$N(CN)$_2^-$ (blue trace) and after reaction with NO$_2$ (red trace).
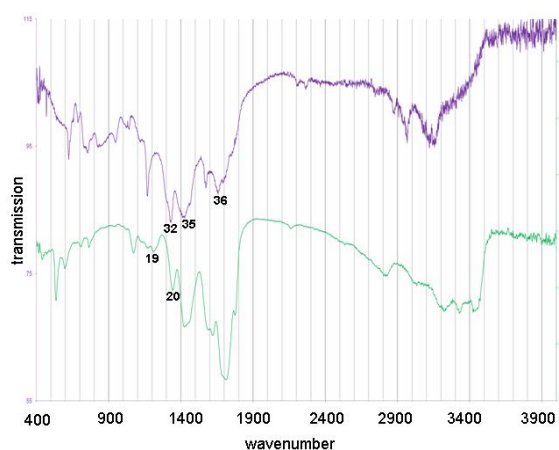
Fig. 9: Product spectrum of thin-film of BMIM$^+$N(CN)$_2^-$ after reaction with gaseous HNO$_3$ (purple trace) and of neat biuret (green trace).

To confirm the possibility that the 1,5-dinitrobiuret (DNB) intermediate is being formed and trapped in the thin-film, *ab initio* computations of the DNB infrared spectrum as well as of other possible intermediates in BMIM$^+$N(CN)$_2^-$/NO$_2$ and BMIM$^+$N(CN)$_2^-$/HNO$_3$ are currently underway.[17] Our preliminary analysis of computed spectra at the B3LYP/6-31+G(d,p) level of theory are consistent with DNB formation.

Our future goal in the experimental FTIR spectroscopy is to significantly expand our understanding of the heterogeneous phase chemistry through detailed kinetics measurements of product and reactant temporal profiles at ionic liquid-oxidizer gas interfaces. We plan to do this by employing an attenuated total reflection (ATR) cell in which there will be temperature control of the ionic liquid thin-film as well as pressure and concentration control of the oxidizer. All three oxidizers, HNO$_3$, N$_2$O$_4$ and H$_2$O$_2$ will be investigated. This will allow reaction orders to be calculated as well as Arrhenius parameters for the products formed in each case. The ATR cell will provide a capability to elucidate the effect of impurities on initiation processes in the IL. This information is of particular importance in ignition model development; since often the purity of ionic liquid fuel can vary considerably, which can significantly affect its ability to hypergolically ignite. For instance, the influence of water impurity will be investigated by introducing a known amount of water both directly into the ionic liquid as well as an added vapor component in the oxidizer gas.

3.2 Ignition Delay Measurements

The search for new igniting room temperature IL/oxidizer combinations continued with the discovery of substituted imidazolium thiocyanate-based ILs and HNO$_3$ hypergols using our fast-videography ignition delay (ID) apparatus.[1] Future studies of the reaction chemistry of the SCN$^-$ anion with HNO$_3$ would be of interest to contrast the proposed initiation process in N(CN)$_2^-$/HNO$_3$ system.

The role of complex ionization of the HNO_3 when mixed with various ionic liquids is also being investigated. The extent of nitronium ion (NO_2^+) formation in the process: $2H^+ + 2NO_3^-$ $\Leftrightarrow 2HNO_3 \Leftrightarrow NO_2^+ + H_2O + NO_3^-$ can be controlled by the addition of excess H_2SO_4 to the nitric acid: $2H_2SO_4 + HNO_3 \Leftrightarrow NO_2^+ + H_3O^+ + 2HSO_4^-$. The effect of $[NO_2^+]$ on both the ignition delay as well as the composition of the pre-ignition products in $BMIM^+N(CN)_2^-/H_2SO_4/HNO_3$ mixtures is currently being studied using our rapid-scan FTIR machine.

3.3 Vacuum Ultraviolet (VUV) Spectroscopic Investigations

The above work was further complemented by carrying out more detailed investigations of room temperature IL vaporization and pyrolysis processes. A thorough understanding of the relative role of vaporization, pyrolysis and oxidation when ILs hypergolically react with HNO_3 is important for constructing high fidelity kinetics models to predict ID times. Vaporization studies were performed at the Chemical Dynamics Beamline at the Advanced Light Source (ALS) facility of the Lawrence Berkeley National Laboratory in collaboration with Professor Steve Leone. This work was carried out under ALS beam-access Grant # 02756. The Chemical Dynamics Beamline at the ALS is capable of producing high-intensity continuous vacuum ultraviolet (VUV) light in the range of 7.4-15 eV, which, when coupled to a time of flight mass spectrometer, is appropriate for determining photoionization efficiency (PIE) curves. PIE data allows for the determination of photoion appearance energies and ionization potentials which provide a powerful means to identify the gas-phase species present when ILs are heated in vacuum.

Experiments were carried out to identify the vapors evolved when ILs are heated. Since ILs have extremely low vapor pressures, identification of the vapors evolved has been difficult to perform experimentally. Our research indicates there exist three regimes important in ionic liquid vaporization, depending on the IL heats of vaporization (ΔH_{vap}) relative to their lowest activation barrier process to thermal decomposition (E_a): 1) $\Delta H_{vap} << E_a$; 2) $\Delta H_{vap} \sim E_a$; and 3) $\Delta H_{vap} >> E_a$. In Case 1, the vapors are solely from vaporization of the ionic liquid, typically as intact cation-anion ion pairs.[2,3] In Case 3, since the heat of vaporization is much higher than the barrier to thermal decomposition, the vapors will consist exclusively of the volatile IL thermal decomposition products. In Case 2, there will be a competition between vaporization of the IL and thermal decomposition of the IL, and the vapor will consist of a combination of vaporized IL and volatile IL thermal decomposition products. Examples of each case are as follows: 1) $EMIM^+NTf_2^-$; 2) $EMIM^+Br^-$; and 3) $EMIM^+SCN^-$. The nucleophilicity of the anion could also play an important role in the thermal stability of these ILs.[18]

Our ALS studies have demonstrated: 1) the influence of molecular structure on the photoion appearance energies of isolated ion pairs; 2) heats of vaporization of ILs can be determined via VUV time-of-flight-mass-spectrometry (TOFMS); 3) the nature of thermal decomposition pathways of several ionic liquids; and 4) the occurrence of new dissociative photoionization processes for some gas phase ionic liquids. Also, studies with aprotic ILs containing strongly nucleophilic anions (N_3^-, Br^-, $N(CN)_2^-$, SCN^-) indicate a variety of reactions occurring when heated: polymerization, proton or alkyl transfer to the anion, and addition of the anion to the cation followed by molecular elimination.

The extremely low vapor pressures of room temperature ILs present a challenge to experimental design for studying their reactivity, as they are not conducive to mass spectrometric study. However, by generating IL aerosols we can circumvent this issue. The process by which gaseous IL species, in the form of aerosolized particles, oxidize in HNO_3 is currently the subject of investigations under a new ALS beam-access Grant # 03341. Recently, generation of ionic liquid aerosols (see Fig. 10) has been achieved by standard aerosol techniques.[19] Optimization studies of the highly thermally stable ionic liquid, $EMIM^+NTf_2^-$, indicates that 0.5 g/l of IL in water is a good choice for producing ~150 nm IL aerosols which are expected to be essentially solvent free. Less thermally stable ILs relevant to Air Force interests have been shown to form aerosols as well. Preliminary work is underway at the Air Force Research Laboratory to determine safe operating conditions for reacting $BMIM^+N(CN)_2^-$ aerosols with various oxidizing vapors.
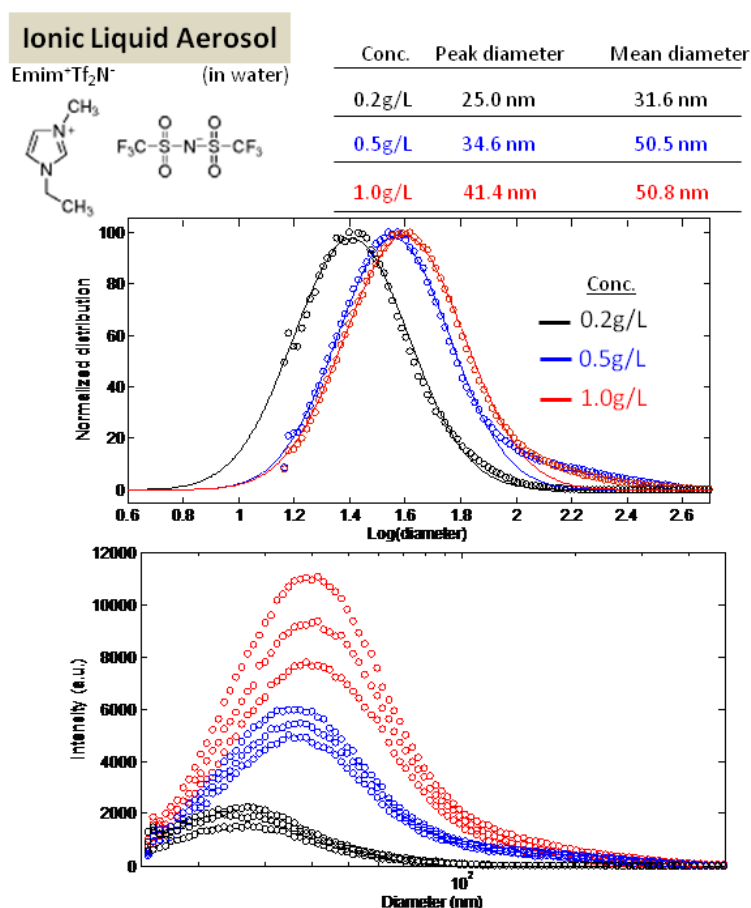
Fig. 10: Size distributions for ionic liquid aerosols generated from varying concentrations in water.

These experimental conditions will be reproduced at the aerosol end-station available at ALS Beamline 9.0.2. Initial experiments will characterize the IL aerosols, including aerosol size distributions, remaining solvent content, and evaluate the photoionization mass spectra in the

absence of oxidizer to establish a baseline. Then, the dicyanamide-based room temperature IL aerosols will be reacted under dilute HNO_3 conditions and the PIE of the gaseous products will be measured. Finally, analysis of the reacted aerosol particles, where the particles are impinged on a hot surface to vaporize the products, will allow for the identification of condensed phase products. Comparison of oxidation products with those in the proposed pre-ignition mechanism[1] will be carried out. Expected products include HNCO (mass 43, IP=11.6 eV), N_2O (mass 44, IP=12.9 eV), CO_2 (mass 44, IP=13.8 eV), NH_3 (mass 17, IP=10.07 eV), and H_2NNO_2 (mass 62). By fixing the photoionization energy and varying other experimental parameters such as temperature, oxidizer concentration, aerosol particle diameter, and mixing time in the flow tube, kinetics measurements will be performed to determine the reactive uptake coefficients and activation energies involved. The investigations will be extended to alternative oxidizers such as NO_2 and H_2O_2.

4.0 FUTURE OUTLOOK

Upon successfully carrying out the oxidation reactions on the dicyanamide-based ionic liquids, we will systematically extend our studies to new classes of high performance hypergolic room temperature ILs where the pre-ignition mechanisms are not known or have not been investigated experimentally. Elucidation of the oxidative mechanisms in these new compounds and comparison to the dicyanamide-based room temperature ILs will provide valuable information regarding their dramatically different ignition characteristics that we have recently observed at the Air Force Research Laboratory (AFRL).   The development of fast chemical (hypergolic) ignition methods for these room temperature ILs is of high importance to the Air Force for designing new energetic bipropellants for space propulsion applications.   A detailed understanding of the oxidation and pre-ignition chemistry that will be possible at the AFRL Propellants Branch and ALS facilities, along with the previously studied competing thermal decomposition processes that are inevitable as the temperature of the room temperature IL is raised during hypergolic combustion, will, for the first time, allow us to construct chemical kinetics models to predict the ignition behavior of these fuels. These proposed laboratory aerosol-oxidizer studies are one step closer to real-world conditions within a propulsion system, where IL fuels are better represented by sprays or liquid droplets mixing with vaporized oxidizer under high temperatures and pressures.

5.0 CONCLUSIONS

New hypergolic IL fuels continue to be discovered by the trial-and-error method of first synthesis and then test approach.[20-22] Our desire to understand the fundamental chemistry of initiation and ignition in IL hypergols provides an opportunity to construct numerical models for designing fuels which have the required reactivity using "first principle" theoretical tools prior to synthesis. We have seen preliminary success of our efforts in a chemical kinetics model,[8] quantitative-structure-property-relationship correlation model,[10] and MD simulations.[9,15] Continued investigations to understand the interplay between physical phenomena, i.e., mixing and interfacial transport, and chemical kinetics. i.e., key initiation reactions, pre-ignition

intermediates and the ignition event, will greatly facilitate the efficient discovery of new hypergols of importance to the IHPRPT Program.

6.0 REFERENCES

1. S. D. Chambreau, S. Schneider, M. Rosander, T. Hawkins, C. J. Gallegos, M. F. Pastewait, and G. L. Vaghjiani, *"Fourier Transform Infrared Studies in Hypergolic Ignition of Ionic Liquids,"* J. Phys. Chem., **A212**, 7816 (2008).

2. S. D. Chambreau, G. L.Vaghjiani, A. To, C. Koh, D. Strasser, O. Kostko, and S. R. Leone, *"Heats of vaporization of room temperature ionic liquids by tunable vacuum ultraviolet photoionization,"* J. Phys. Chem. Phys. **B114**, 1361 (2010).

3. D. Strasser, F. Goulay, L. Belau, O. Kostko, C. Koh, S. D. Chambreau, G. L.Vaghjiani, M. Ahmed, and S. R. Leone, *"Tunable Wavelength Soft Photoionization of Ionic Liquid Vapors,"* J. Phys. Chem. Phys. **A114**, 879 (2010).

4. A. Osmont, L. Catoire, T. M. Klapotke, G. L. Vaghjiani, and M. T. Swihart, *"Thermochemistry of Species Potentially Formed During NTO/MMH Hypergolic Ignition,"* Propellants, Explosives & Pyrotechnics, **33,** 209 (2008).

5. S. Schneider, T. Hawkins, M. Rosander, G. Vaghjiani, S. Chambreau, G. Drake, *"Ionic Liquids as Hypergolic Fuels,"* Energy & Fuels, **22**, 2871 (2008).

6. S. Schneider, T. Hawkins, M. Rosander, J. Mills, G. Vaghjiani, and S. Chambreau, *"Liquid Azide Salts and Their Reactions with Common Oxidizers IRFNA and N_2O_4,"* Inorg. Chem., **47**, 6082 (2008).

7. A. J. Alfano, J. D. Mills, and G. L. Vaghjiani, *"Highly Accurate Ignition Delay Apparatus for Hypergolic Fuel Research,"* Reviews of Scientific Instruments, **77**, 45109 (2006).

8. L. Catoire, S. D. Chambreau, and G. L. Vaghjiani, *"Chemical Kinetics Interpretation of Hypergolicity of Some Ionic Liquid-Based Systems,"* Combustion & Flame, **submitted** (2010).

9. D. Sengupta, J. V. Cole, and G. L. Vaghjiani, *"Quantum Molecular Dynamics Simulations of Hypergolic Reactions Between an Energetic Ionic Liquid and Nitric Acid,"* 57th JANNAF PM / 5th LPS / 4th SPS and 7th MSS Joint Meeting, 2010.

10. D. Sengupta, M. Pindera, J. V. Cole, and G. L. Vaghjiani, *"QSPR and Artificial Neural Network Predictions of Hypergolic Ignition Delays for Energetic Ionic Liquids,"* 57th JANNAF PM / 5th LPS / 4th SPS and 7th MSS Joint Meeting, 2010.

11. M. Rosander, S. Schneider, T. Hawkins, J. Mill, G. L. Vaghjiani, and S. D. Chambreau, *"Ionic Liquids as 'Green' Replacements for Hydrazines in Bipropellant Rocket Applications,"* ACS Div. Fuel Chem. Preprints, **54**, 167 (2009).

12. M. J. Frisch, G. W. Trucks, H. B. Schlegel, G. E. Scuseria, M. A. Robb, J. R. Cheeseman, J. J. A. Montgomery, T. Vreven, K. N. Kudin, J. C. Burant, J. M. Millam, S. S. Iyengar, J. Tomasi, V. Barone, B. Mennucci, M. Cossi, G. Scalmani, N. Rega, G. A. Petersson, H. Nakatsuji, M. Hada, M. Ehara, K. Toyota, R. Fukuda, J. Hasegawa, M. Ishida, T. Nakajima, Y. Honda, O. Kitao, H. Nakai, M. Klene, X. Li, J. E. Knox, H. P. Hratchian, J. B. Cross, C. Adamo, J. Jaramillo, R. Gomperts, R. E. Stratmann, O. Yazyev, A. J. Austin, R. Cammi, C. Pomelli, J. W. Ochterski, P. Y. Ayala, K. Morokuma, G. A. Voth, P. Salvador, J. J. Dannenberg, V. G. Zakrzewski, S. Dapprich, A. D. Daniels, M. C. Strain, O. Farkas, D. K. Malick, A. D. Rabuck, K. Raghavachari, J. B. Foresman, J. V. Ortiz, Q. Cui, A. G. Baboul, S. Clifford, J. Cioslowski, B. B. Stefanov, G. Liu, A. Liashenko, P. Piskorz, I. Komaromi, R. L. Martin, D. J. Fox, T. Keith, M. A. Al-Laham, C. Y. Peng, A. Nanayakkara, M. Challacombe, P. M. W. Gill, B. Johnson, W. Chen, M. W. Wong, C. Gonzalez, and J. A. Pople *Gaussian 03, Revision C.01*, Gaussian, Inc., Wallingford, CT (2004).

13. W. L. Hase, K. Bolton, P. de Sainte Claire, R. J. Duchovic, X. Hu, A. Komornicki, G. Li, K. Lim, D. Lu, G. H. Peslherbe, K. Song, K. N. Swamy, S. R. Vande Linde, A. Varandas, H. Wang, and R. J. Wolf, *"VENUS99: A General Chemical Dynamics Computer Program,"* (1999).

14. J. Geith, G. Holl, T. M. Klapötke, and J. J. Weigand, *"Pyrolysis Experiments and Thermochemistry of Mononitrobiuret (MNB) and 1,5-dinitrobiuret (DNB),"* Combustion and Flame, **139**, 358 (2004).

15. J. Liu, S. D. Chambreau, and G. L. Vaghjiani, *"Direct Dynamics Trajectory Study of Thermal Decomposition of 1, 5-Dinitrobiuret (DNB),"* **manuscript in preparation** (2010).

16. R. J. Kee, F. M. Rupley, J. A. Miller, M. E. Coltrin, J. F. Grcar , E. Meeks, H. K. Moffat, A. E. Lutz, G. Dixon-Lewis, M. D. Smooke, J. Warnatz, G. H. Evans, R. S. Larson, R. E. Mitchell, L. R. Petzold, W. C. Reynolds, M. Caracotsios, W. E. Stewart, P. Glarborg, C. Wang, and O. Adigun, *"Chemkin Collection, Release 3.6.2,"* Reaction Design, Inc., San Diego, CA (2001).

17. G. L. Vaghjiani, S. D. Chambreau, E. Mitchell, and C-S. Kim, *"Transmission FTIR Spectroscopic Investigations of the Interaction Between Ionic Liquid Thin-films and Gaseous HNO_3 and NO_2,"* **manuscript in preparation** (2010).

18. S. D. Chambreau, G. L. Vaghjiani, C. Koh, O. Kostko, A. Golan, D. Strasser, and S. R. Leone, *"Volatility of 1-alkyl-3-methylimidazolium-based ionic liquids studied by tunable vacuum ultraviolet spectroscopy,"* **manuscript in preparation** (2010).

19. J. H. Kroll, J. D. Smith, D. L. Che, S. H. Kessler, D. R. Worsnop, and K. R. Wilson, *"Measurement of Fragmentation and Functionalization Pathways in the Heterogeneous Oxidation of Oxidized Organic Aerosol,"* Phys. Chem. Chem. Phys., **11**, 8005 (2009).

20. H. Gao, Y-H. Joo, B. Twamley, Z. Zhou, and J. M. Shreeve, *"Hypergolic Ionic Liquids with the 2,2-Dialkyltriazanium Cation,"* Angew. Chem. Int. Ed., **48**, 2792 (2009).

21. Y-H. Joo, H. Gao, Y. Zhang, and J. M. Shreeve, *"Inorganic or Organic Azide-Containing Hypergolic Ionic Liquids,"* Inorg. Chem., **49**, 3282 (2010).

22. L. He, G-H. Tao, D. A. Parrish, and J. M. Shreeve, *"Nitrocyanamide-Based Ionic Liquids and Their Potential Applications as Hypergolic Fuels,"* Chem. Eur. J., **16**, 5736 (2010).

Appendix

Fourier Transform Infrared Studies in Hypergolic Ignition of Ionic Liquids

**Steven D. Chambreau,[†] Stefan Schneider,[†] Michael Rosander,[†] Tom Hawkins,[‡]
Christopher J. Gallegos,[‡] Matthew F. Pastewait,[‡] and Ghanshyam L. Vaghjiani[‡,*]**

*Space and Missile Propulsion Division, Propulsion Directorate, Air Force Research Laboratory, AFRI/RZSP,
10 E Saturn Boulevard, Edwards AFB, California 93524*

Received: April 28, 2008; Revised Manuscript Received: June 2, 2008

A class of room-temperature ionic liquids (RTILs) that exhibit hypergolic activity toward fuming nitric acid is reported. Fast ignition of dicyanamide ionic liquids when mixed with nitric acid is contrasted with the reactivity of the ionic liquid azides, which show high reactivity with nitric acid, but do not ignite. The reactivity of other potential salt fuels is assessed here. Rapid-scan, Fourier transform infrared (FTIR) spectroscopy of the preignition phase indicates the evolution of N_2O from both the dicyanamide and azide RTILs. Evidence for the evolution of CO_2 and isocyanic acid (HNCO) with similar temporal behavior to N_2O from reaction of the dicyanamide ionic liquids with nitric acid is presented. Evolution of HN_3 is detected from the azides. No evolution of HCN from the dicyanamide reactions was detected. From the FTIR observations, biuret reaction tests, and initial ab initio calculations, a mechanism is proposed for the formation of N_2O, CO_2, and HNCO from the dicyanamide reactions during preignition.

Introduction

There continues to be a growing effort to synthesize task-specific ionic liquids (ILs). Ionic liquids are salts with melting points below 100 °C. Lately, the design and choice of many ionic liquids is focused on physical properties such as miscibility, conductivity, viscosity, solubility, and melting points.[1] An interesting and important property of ionic liquids is that they have very low vapor pressures, with high heats of vaporization (approaching ~60 kcal mol^{-1}).[2] The details of how the chemical structure of the ionic liquid affects these various physical characteristics are now beginning to emerge.[3-6] Less understood, but now of great interest, are the associated chemical properties that manifest in the condensed phase such as relative basicity (or acidity), oxidative (or reductive) capacity, thermal stability, electrochemical reactivity, and catalytic or combustion efficiency of the component ions.[7-9]

Recent interest in room temperature ionic liquids has grown immensely, as their synthetic routes have been optimized. The number of publications involving ionic liquid chemistry has grown exponentially in the past decade.[1,10,11] The number of possible different cation—anion combinations to form ILs is enormous, and so it is important to understand trends in reactivity and to have theoretical tools to screen for the best IL candidates for a given use. Typical cations for ionic liquids considered here include asymmetrically substituted imidazoliums and triazoliums, since symmetric cations tend to produce solid salts at room temperature.[6] However, for a given cationic system, the choice of the anion is also important in tailoring the liquidus range of the salt.[12] Similarly, the chemical and thermal stabilities of the resulting IL can depend both on the physical (structural) and chemical properties of the individual component ions.[9,13,14] For instance, in the case of imidazolium ionic liquids, studies have shown that the overall thermal stability of the IL correlates with the anion's size,[15] its nucleophilicity (or its Lewis

basicity),[13,16,17] and its hydrophilicity,[18] etc. On the other hand, for a given anionic system, cationic size has little effect on the IL stability,[18,19] while increased substitution of the imidazolium ring at the C(2)-site by straight-alkyl chains increases the stability but secondary or tertiary alkyl groups at the N-site decreases the stability.[13]

Recently, several groups have shown that some classes of ionic liquids can be distilled in a vacuum.[20] These ILs tend to have aprotic cations and non-nucleophilic anions, and studies have shown that the gas-phase species exist (in high vacuum) as neutral ion pairs and do not tend to vaporize as gas-phase clusters.[21-23] For protic ionic liquids, however, the formation of neutral molecules in the gas phase has also been reported.[22] An important thermochemical property which is difficult to obtain accurately for ionic liquids is the condensed phase heat of formation. Due to the ionic nature and liquid phase of ILs, theoretical calculations of the condensed phase heats of formation are difficult and have large uncertainties associated with them. Recent experimental measurements of heats of combustion and heats of vaporization of ILs have begun to accurately determine the condensed phase heat of formation for a few ionic liquids.[24,25]

Here, we present the results of our efforts to tailor ionic liquids for utilization in bipropellant rocket engines. We desire not only to improve the performance (i.e., density specific impulse) over the current, state-of-the-art, monomethyl hydrazine/nitrogen tetroxide (MMH/NTO) system, but also to be able to increase the ambient reactivity of the component ions toward common oxidizers, such that hypergolic ignition (spontaneous ignition upon mixing) is attained, comparable to MMH/NTO ignition times. To calculate performance characteristics of propellants, the condensed phase heat of formation value is critical.[26,27] To successfully implement such ionic liquids into viable working systems, their physical properties such as viscosity and the liquid temperature range must also be tailored within required operational ranges.[1,8] Furthermore, the inherent low vapor pressure of ionic liquids should significantly reduce the ambient toxicity and environmental emissions and therefore

* To whom correspondence should be addressed. E-mail: ghanshyam.vaghjiani@edwards.af.mil.
† ERC Inc.
‡ Propellants Branch.

Appendix
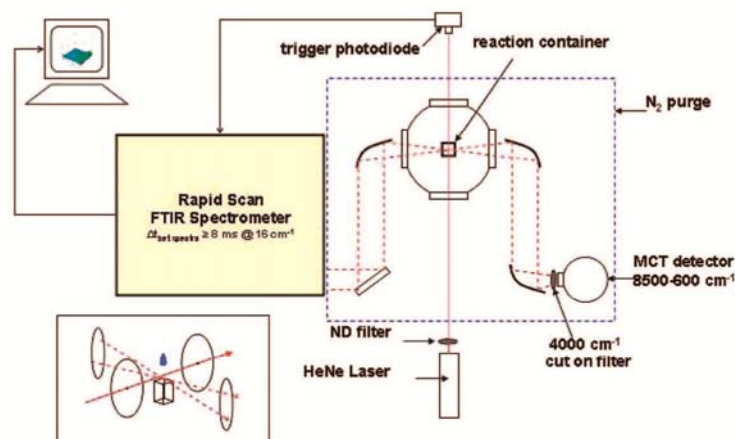
Figure 1. Schematic of the FTIR apparatus. The inset illustration in the lower left corner shows the relative positions of the HeNe laser beam, the IR beam, and the falling oxidizer droplet.

the associated cost of handling and fielding of these new replacement fuels. The extremely low vapor pressure of ionic liquids at ambient temperature and pressure is a major benefit of hypergolic ionic liquid fuels versus MMH, which is highly volatile. The high vapor toxicity of MMH increases the safety precautions required, and the logistics of handling it safely while loading the space-vehicle can be very expensive.

Understanding of chemical pathways and reaction mechanisms when fuels/ILs react with strong oxidizers is critical to designing new fuels. The current MMH/NTO hypergolic system has been used successfully for decades,[28,29] and much theoretical work on the MMH/NTO system has been performed.[30–35] However, little experimental work exists[36–40] to confirm these results. Therefore, replacing the volatile, highly toxic, and carcinogenic MMH with a safer fuel is not a straightforward task. One of the challenges is that the mechanism involves highly reactive transient species which are difficult to probe experimentally.[41,42] The identification of common reactive species in different hypergolic systems will play a significant role in future fuel design. There are two different regimes involved in hypergolic systems: first, the low-temperature preignition phase, where gaseous reactive species are produced and the temperature of the system increases as thermolytic and oxidative processes in the condensed phase begin to decompose both the fuel and the oxidizer. Once the temperature and concentrations of key species reach a critical level, ignition occurs in the gas phase,[38,43] the temperature increases dramatically, and combustion occurs. To construct accurate numerical combustion models for IL hypergols, detailed chemical mechanistic information is needed on how fuel vaporization/pyrolysis processes compete with and augment concurrent and subsequent oxidative processes of the reactive fragments that are being produced.

Initial attempts by the Air Force Research Laboratory to design ILs with highly strained or unsaturated functional groups were made to introduce "trigger groups" onto the cation in the hope of inducing hypergolicity. These cations may be paired with oxygen-containing anions (NO_3^-) for oxygen balance or high heats of formation (N_3^-) to promote hypergolic ignition when treated with a suitable oxidizer.[44] The discovery that the anion can play a critical role in inducing hypergolicity is described here. The fact that a common anion can induce hypergolicity when paired with numerous different cations to form ionic liquids allows for the tailoring of the cation for

various desirable properties such as high heat of formation, low viscosity, a wide liquid temperature range, environmental safety, and thermal and shock stability. This paper describes the investigation of the preignition phase of hypergolic ignition of ionic liquids, a critical anion needed to induce hypergolic reactivity, and the influence of cation structure on the reactivity. This investigation focuses on white fuming nitric acid (WFNA) as the oxidizer.

Experimental Technique

Fourier-transform infrared (FTIR) absorption spectroscopy was performed using a rapid-scan spectrometer. Typical spectra were acquired in the range 590–3850 cm^{-1} with a spectral resolution of 2 cm^{-1} and approximately every 30 ms. The interferograms were recorded in split double-sided, split forward–backward mode. The reaction was carried out within a closed stainless steel chamber under constant nitrogen purge and therefore was carried out in an oxygen-free environment. Figure 1 shows the schematic of our experimental setup. The infrared beam was focused into the chamber above the reaction cell by means of gold mirrors and KRS-5 windows. A drop of oxidizer was introduced from a gastight syringe through a septum at the top of the chamber. The drop fell into a small cuvette containing a small amount (0.1–1.0 mL) of ionic liquid fuel. The spectrometer was triggered via a HeNe laser and photodiode positioned above the reaction cell. As the drop of oxidizer passes through the HeNe beam, the drop in signal from the photodiode triggers the spectrometer. Data was collected before the ignition flash occurs and is hereafter referred to as the preignition phase data.

To observe and measure the actual ignition delay (ID), a small fuel sample (10–50 μL) was instead dropped into the cuvette containing an excess amount (1.0 mL) of the oxidizer. A high-speed, complementary metal-oxide semiconductor (CMOS) video imager was used to record the time duration from the moment the fuel comes in contact with the liquid surface of the oxidizer and the first sign when a visible flame is formed, which invariably was always in the gas phase above the liquid surface. In the present work, the CMOS video settings of 1000 frames/sec and 168 × 512 pixel resolution were chosen. Figure 2 depicts typical observations for MMH/NTO, MMH/WFNA, and 1-propargyl-3-methyl-imidazolium dicyanamide/WFNA hypergolic ignitions for which the ID times were determined to

Appendix
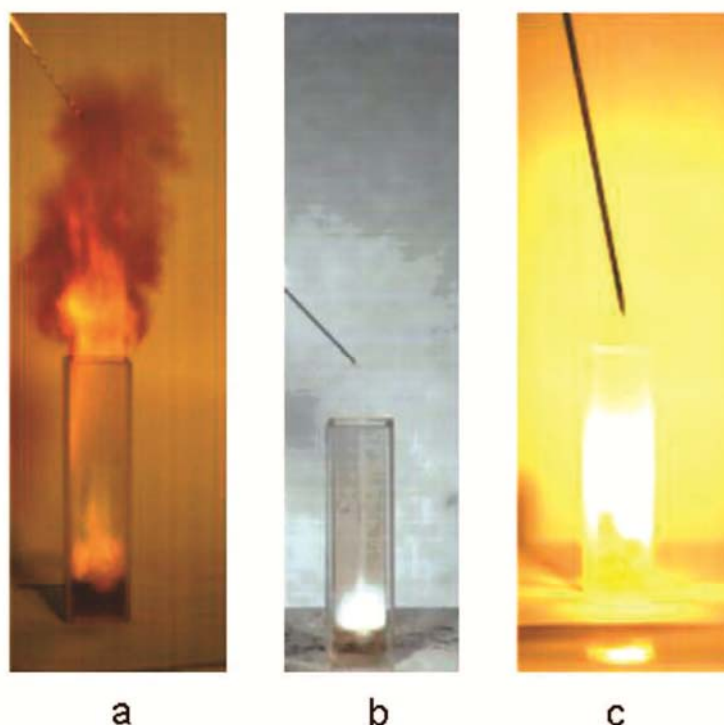
Figure 2. Hypergolic ignition of (a) MMH/NTO, ID = 1 ms; (b) MMH/WFNA, ID = 9 ms; and (c) 1-propargyl-3-methyl-imidazolium dicyanamide/WFNA, ID = 15 ms.

TABLE 1: Theoretical Reaction Enthalpies Calculated at the Hartree−Fock and Density Functional Theory Levels

reaction	ΔH_{0K} kcal/mol (zpe corrected)	method
$NO_3^- + H^+ \rightarrow HNO_3$	−318.5	B3-LYP 6-31G(+)(d,p)
$N(CN)_2^- + H^+ \rightarrow HN(CN)_2$	−302.8	B3-LYP 6-31G(+)(d,p)
$N(CN)_2^- + H^+ \rightarrow (NC)N(CNH)$	−310.4	B3-LYP 6-31G(+)(d,p)
$HN(CN)_2 + H^+ \rightarrow H_2N(CN)_2^+$	−130.9	B3-LYP 6-31G(+)(d,p)
$(NC)N(CNH) + H^+ \rightarrow (NC)NH(CNH)^+$	−166.2	B3-LYP 6-31G(+)(d,p)
$N(NO_2)_2^- + H^+ \rightarrow HN(NO_2)_2$	−303.8	RHF 6-31G(+)(d,p)
$N(NO_2)_2^- + H^+ \rightarrow HN(NO_2)_2$	−303.6	B3-LYP 6-31G(+)(d,p)
$N(NO_2)_2^- + H^+ \rightarrow (O_2N)N(NO_2H)$	−297.0	RHF 6-31G(+)(d,p)
$HN(NO_2)_2 + H^+ \rightarrow H_2N(NO_2)_2^+$	−169.9	B3-LYP 6-31G(+)(d,p)
$(O_2N)N(NO_2H) + H^+ \rightarrow H_2O + N_2O + NO_2^+$	−212.4	RHF 6-31G(+)(d,p)
$HN(NO_2)_2 + H^+ \rightarrow H_2O + N_2O + NO_2^+$	−205.5	RHF 6-31G(+)(d,p)
$(NC)N(NO_2)^- + H^+ \rightarrow (NC)NH(NO_2)$	−307.8	RHF 6-31G(+)(d,p)
$(NC)N(NO_2)^- + H^+ \rightarrow (HNC)N(NO_2)$	−297.9	RHF 6-31G(+)(d,p)
$(NC)N(NO_2)^- + H^+ \rightarrow (NC)N(NO_2H)$	−321.6	RHF 6-31G(+)(d,p)
$(NC)N(NO_2H) + H^+ \rightarrow (NC)N(NO_2H_2)^+ \rightarrow H_2O + NCNNO^+$	−122.6	RHF 6-31G(+)(d,p)
$(NC)N(NO_2H) + H^+ \rightarrow H_2O + N_2O + CN^+$	28.2	RHF 6-31G(+)(d,p)
$(NC)NH(NO_2) + H^+ \rightarrow H_2O + N_2O + CN^+$	14.4	RHF 6-31G(+)(d,p)
$(HNC)N(NO_2) + H^+ \rightarrow H_2O + N_2O + CN^+$	4.5	RHF 6-31G(+)(d,p)
$(NC)N(NO_2H) + H^+ \rightarrow (NC)NH(NO_2H)^+$	−148.1	RHF 6-31G(+)(d,p)
$(NC)N(NO_2H) + H^+ \rightarrow (HNC)N(NO_2H)^+$	−166.2	RHF 6-31G(+)(d,p)
$(HNC)N(NO_2) + H^+ \rightarrow (HNC)NH(NO_2)^+$	−182.5	RHF 6-31G(+)(d,p)
$(NC)NH(NO_2) + H^+ \rightarrow (HNC)NH(NO_2)^+$	−172.6	RHF 6-31G(+)(d,p)
$(HNC)N(NO_2) + H^+ \rightarrow (HNC)N(NO_2H)^+$	−189.9	RHF 6-31G(+)(d,p)
$NC\text{-}N\text{-}CNH + NO_3^- \rightarrow NC\text{−}N\text{−}C(NO_3)NH^-$	−5.4	B3-LYP 6-31G(+)(d,p)
$NC\text{−}N\text{−}C(NO_3)NH^- \rightarrow NC\text{−}N\text{−}C(=O)N(NO_2)H^-$	−34.5	B3-LYP 6-31G(+)(d,p)
$NC\text{−}N\text{−}C(=O)N(NO_2)H^- + H^+ \rightarrow HNC\text{−}N\text{−}C(=O)N(NO_2)H$	−305.2	B3-LYP 6-31G(+)(d,p)
$HNC\text{−}N\text{−}C(=O)N(NO_2)H + H^+ \rightarrow HNC\text{-}NH\text{-}C(=O)N(NO_2)H^+$	−178.0	B3-LYP 6-31G(+)(d,p)

be ~1, 9 and 15 ms, respectively. For the interested reader we provide Supporting Information as a mpg-file that shows hypergolic ignition.

On the basis of a common understanding of how certain energetic materials are known to decompose to stable products, and the similarity in the products we observed here, a suitable method to identify the nature of at least one of the possible intermediates was carried out as follows. The reaction of ILs with nitric acid can be slowed down using 34 wt % HNO₃ solutions instead of WFNA. This allows for the possibility to trap reaction intermediates by quenching and then suitably identifying their nature. Here, we performed the biuret test using

Appendix

the method of Lowry[45] to identify the presence of peptide-like functionality in the reaction intermediate using Cu^{2+} solutions. Confirmation of the presence of such a functionality together with the observed and theoretical evaluations of all the systematically substituted anions studied here would provide strong evidence for the proposed mechanism (see Discussion).

Materials. The following chemicals were synthesized and characterized: 1-butyl-3-methyl-imidazolium azide (>97%), 1-allyl-3-methyl-imidazolium azide (>97%), 1-butyl-3-methyl-imidazolium dicyanamide (>97%), 1-allyl-3-methyl-imidazolium dicyanamide (>97%), 1-propargyl-3-methyl-imidazolium dicyanamide (>97%), 1-methyl-4-amino-1,2,4,-triazolium dicyanamide (>97%), 1-(3-butenyl)-3-methyl-imidazolium dicyanamide (>97%), 1-(2-pentynyl)-3-methyl-imidazolium dicyanamide (>97%), 1-methyl-4-amino-1,2,4,-triazolium nitrocyanamide (>97%), 1-allyl-4-amino-1,2,4-triazolium nitrocyanamide (>97%), and silver nitrocyanamide (>97%). The characterization data of the above azides is reported elsewhere.[44] The purities of the above compounds were determined by elemental analysis. Potassium dinitramide (>97%) was kindly supplied by SRI. The following chemicals were purchased from Merck: 1-butyl-3-methyl-imidazolium dicyanamide (>99%), 1-butyl-1-methyl-pyrolidinium dicyanamide (>99%), and n-butyl-3-methyl-pyridinium dicyanamide (>99%). 1-ethyl-3-methyl-imidazolium dicyanamide (>98%) was purchased from Fluka. Sodium azide (>99.5%), sodium dicyanamide (>96%), and silver cyanate (>99%) were purchased from Sigma Aldrich, and white fuming nitric acid (>99.5%) was purchased from Fluka. All chemicals purchased were used without further purification.

Ab Initio Calculations. To predict the proton affinities and reaction enthalpies involved in this study, ab initio calculations were carried out on the Gaussian 03 suite of programs.[46] Molecular geometries were preoptimized at the Hartree−Fock 3-21G level of theory, and vibrational frequencies were calculated to confirm that a (local) energy minimum had been reached. Subsequent optimization, energy, and vibrational frequency calculations were performed at Hartree−Fock 6-31+G(d,p) level or density functional theory (DFT) level with the hybrid functional, B3LYP 6-31+G(d,p), and these vibrational frequencies confirmed that the optimized structures were minima on the potential energy surface. The HF zero-point vibrational energies (ZPVE) were scaled by 0.9153 and the DFT zero-point energies were scaled by 0.9806.[47] The corrected zero-point energies were added to the stationary point energies. No thermal corrections were made to determine the reaction enthalpies at 298 K, and the values reported here are at 0 K. Reaction enthalpies at 0 K were calculated by subtracting the sum of the heats of formation of the reactants from the sum of the heats of formation of the products. Table 1 shows the predicted proton affinities and reaction enthalpies at 0 K of the various reaction steps considered here. A more detailed ab initio study will be the subject of a future publication.

Results

FTIR absorption spectra of the gas-phase species evolved when ILs react with white fuming nitric acid can be seen in Figures 3−6. In Figure 3, product peaks in the reaction of 1-butyl-3-methyl-imidazolium azide with WFNA, which does not ignite, are shown. To improve the signal-to-noise ratio, an average of 11 scans (obtained in the time range 270−620 ms) was taken after the spectrometer was triggered. One distinct N_2O and two HN_3 peaks are detected with origins at 2223.5, 2139.6, and 1149.4 cm^{-1}, respectively. The expected HN_3 absorption peak at ~3336 cm^{-1} is too weak to be discerned
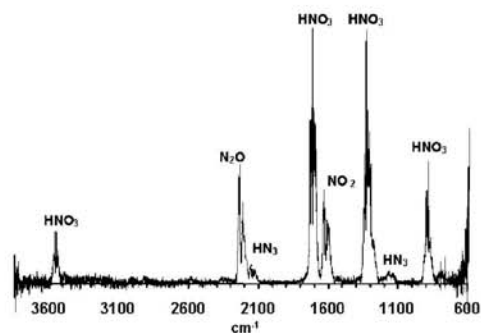

Figure 3. IR product spectrum of 1-butyl-3-methyl-imidazolium (BMIM) azide reacting with WFNA.
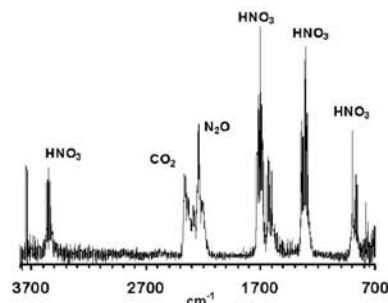
Figure 4. IR product spectrum of BMIM dicyanamide reacting with WFNA.
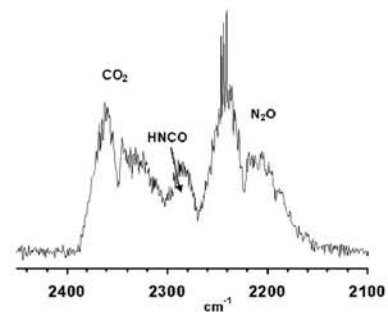
Figure 5. IR product spectrum of BMIM dicyanamide reacting with WFNA. The evolution of CO_2, N_2O, and HNCO is shown here.

from the recorded spectral noise.[48] All other peaks in the spectrum have been assigned to gaseous HNO_3 and NO_2. When 1-butyl-3-methyl-imidazolium dicyanamide is reacted with WFNA, both CO_2 (origin = 2348.4 cm^{-1}) and N_2O (origin = 2222.6 cm^{-1}) are evolved before ignition, as seen in Figure 4. Upon closer inspection, a peak is seen which appears in between the CO_2 and N_2O peaks (Figure 5). Figure 6 shows the result of subtracting the N_2O and CO_2 contributions to the spectrum in Figure 5, after having normalized the N_2O peak data with Figure 3 and the CO_2 peak with an ambient spectrum. The residual absorption feature has an origin at approximately 2269 cm^{-1} and is identified as isocyanic acid (HNCO). Absent in the spectra of the preignition vapor phase are any other gaseous combustion products; HCN, HONO, NO, and CO. Absorptions by H_2O, which is possible according to our mechanism as discussed later, can be observed in Figure 4 near ~1600 and ~3750 cm^{-1}.

The time profile of the isocyanic acid product tracks with the N_2O and CO_2 products, as seen in Figure 7. Upon systematic

substitution of cyano groups by nitro groups on the dicyanamide anion, comparison of the reactivity of sodium dicyanamide (NaN(CN)$_2$), silver nitrocyanamide (AgN(CN)NO$_2$), and potassium dinitramide (KN(NO$_2$)$_2$) with WFNA was carried out. Sodium dicyanamide reacts violently with WFNA, producing CO$_2$, N$_2$O, and HNCO (see Figure 8) before igniting (ID = ~825 ms), as did all the heterocyclic dicyanamide ILs with their own characteristic ID times which we report elsewhere.[49] The observed gas-phase species time profiles in the reaction of NaN(CN)$_2$ salt and WFNA were similar to that in Figure 7. The nitrocyanamide salt does not ignite and FTIR measurements showed that the nitrocyanamide anion did not react to produce any detectable gaseous products (in fact, only the initial HNO$_3$ and NO$_2$ constituents of the WFNA are observed). The dinitramide salt reacted slowly without ignition to evolve N$_2$O.

In comparing the spectra of all dicyanamides, only the CO$_2$, N$_2$O, and isocyanic acid are common products. The observed CO$_2$/N$_2$O product signal ratio in IL-dicyanamide reactions with WFNA were similar to that in sodium dicyanamide's reaction, suggesting minimal influence of the cation on the reaction temperature for which the data was collected. However, for both 1-propargyl-3-methyl-imidazolium dicyanamide and 1-allyl-3-methyl-imidazolium dicyanamide, a new peak emerges which is centered at 1800 cm^{-1} (Figure 9). The appearance of this species occurs only just before ignition (within 15 to 43 msec) and could possibly be a fragment product coming from reaction at the unsaturated functional group of the cation.

The main findings of the biuret reaction test were as follows. When the reaction of NaN(CN)$_2$ (90 mg) with 34 wt % HNO$_3$ (1 drop) was quenched after a minute using excess 2% KOH solution, a cloudy deep purple-pink complex resulted on the addition of 2−4 drops of 1% CuSO$_4$ solution, which turned cloudy pink within a few minutes and remained stable for many hours. A similar result was also obtained for 1-butyl-3-methyl-imidazolium dicyanamide/34 wt % HNO$_3$ system. Blank runs in which no acid was added but the same amount of KOH was used produced no change in the coloration upon Cu^{2+} addition. These solutions remained light blue. The pink color change for the dicyanamide/HNO$_3$ systems indicates a positive biuret test in which the reaction intermediate (which has a biuret or peptide-like functionality) reacts with the Cu(II) ions to form a Cu(I)-coordination complex. When the same tests were performed for the HNO$_3$ reaction with 1-methyl-4-amino-1,2,4,-triazolium nitrocyanamide and 1-allyl-4-amino-1,2,4,-triazolium nitrocyanamide, no pink coloration was observed.

Discussion

All of the azides when treated with WFNA or inhibited red fuming nitric acid (IRFNA) failed to ignite. Displacement by the weaker acid on excess addition of nitric acid leads to evolution of HN$_3$ into the gas phase. The observed N$_2$O (with coproduct N$_2$) arises as a result of decomposition of the NON$_3$ intermediate[50] formed in the condensed-phase interaction of N$_3^-$ with NO$^+$. The source of NO$^+$ is the autoionization reaction, (N$_2$O$_4$ ↔ NO$^+$ + NO$_3^-$) which is possible since small amounts of NO$_2$ can be present in WFNA and up to ~14% is dissolved in WFNA to form the IRFNA. The initial heat release from the N$_3^-$ ion decomposition to form N$_2$ and N$_2$O is not sufficient in our tests to further decompose the heterocyclic countercation to cause ignition, even when (partial) oxidation of the cation may concurrently contribute to the heat release.[44] CAUTION: The product, hydrazoic acid (HN$_3$) is a highly toxic pungent smelling compound whose vapor can cause violent headaches. HN$_3$ acts as a noncumulative poison. A low but potentially fatal

dosage of NO$_2$ by inhalation can lead to lung edema. Low concentration (4 ppm) exposures can anesthetize the nose, thus creating a potential for overexposure. It must also be emphasized that WFNA and IRFNA are violently reactive, hazardous, and toxic materials and only small quantities should be used under well-ventilated conditions with carefully planned safety protocols and protective equipment in place. The present experimental setup of Figure 1 (details not shown) allowed for the proper containment and disposal of all the materials tested and their reaction products.
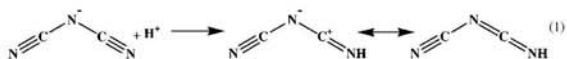
The identification of HNCO by FTIR and the elimination of competing possibilities is now addressed. Because the peak at ~2269 cm^{-1} is also present when sodium dicyanamide salt is reacted with WFNA, it cannot be a product resulting from reaction with the imidazolium cation. This is further evidenced by the lack of high frequency hydrogen stretching modes expected from hydrocarbon products of reaction with the imidazolium cation, and which are also absent for the azide IL with the same cation (Figure 3). Known cyanogen (N≡C−C≡N)[51] absorption features could not be matched with the data of Figure 6, and the presence of cyanamide (H$_2$NC≡N)[52] is also ruled out based on the fact that there was no evidence for absorption at 1055 cm^{-1} due to the ν_4(N−CN) symmetric stretching mode.[52,53] Instead, a match of the data was found with the spectrum for isocyanic acid (HNCO).[54,55] According to Herzberg and Reid,[54] the ν_2(N≡C=O) asymmetric stretching mode centered at ~2274 cm^{-1} (and more recently reported by Steiner and co-workers to be at 2268.9 cm^{-1}[56] and Fisher and co-workers to be at 2259 cm^{-1}[57]) can be identified here to be responsible for the observed strong absorption. HNCO also has two smaller peaks centered at ~797 and ~3531 cm^{-1} with 31% and 24% of the peak height at 2274 cm^{-1}. Even with poor signal-to-noise ratio in the 800 cm^{-1} region, the former peak for the ν_4(H−N=CO) bend is just discernible in Figure 4, while the latter peak for ν_1(H−NCO) stretch remains apparently concealed by the large HNO$_3$ peak at around 3550 cm^{-1}. The other three bands, ν_3, ν_5, and ν_6, respectively at 1322, 577, and 656 cm^{-1} are too weak, and in any case, the former is masked by the strong HNO$_3$ peaks while the latter two are in the detection cutoff vicinity of the present detector. Also, the observed 2269 cm^{-1} feature is not due to the ν_2 stretching features of fulminic acid (HCNO), which is reported to be at ~2196 cm^{-1} (and thus to the red of the N$_2$O absorption),[58,59] or of cyanic acid (HOCN) reported to be at ~2302 cm^{-1}[60] since its corresponding ν_4(HO−CN) stretching absorption at ~1082 cm^{-1} is not seen in our data.[61] Both HCNO and HOCN are higher energy isomers of HNCO and are not expected to be in any significant amounts in the gas phase.[62]

It is well-known that nitriles can undergo acid catalyzed hydration reactions.[63] Because the protonated form is much more receptive to nucleophiles at the nitrile carbon, water adds slowly to the carbon and then rearranges to form an amide. The acid-catalyzed reaction with the dicyanamide anion can occur in a similar fashion, but when reacting with WFNA, the nucleophile is NO$_3^-$ instead of H$_2$O, and the nitrile functional group is subsequently converted to a C(=O)NHNO$_2$ group. Because NO$_3^-$ is a better nucleophile than water,[64] the rate of addition of NO$_3^-$ to the carbon center is expected to be faster than for water in WFNA conditions.

The details of the proposed mechanism for the reaction of the dicyanamide anion with nitric acid are presented here. The first step is to protonate the dicyanamide anion at the nitrile nitrogen, followed by NO$_3^-$ attack at the electrophilic carbon

Appendix

FTIR Studies in Hypergolic Ignition of Ionic Liquids

J. Phys. Chem. A, Vol. 112, No. 34, 2008 **7821**

and NO_2 migration to the terminal nitrogen (see Table 1 for calculated energetics):


(1)

The calculated gas-phase proton affinity of the nitrile nitrogen is about 7.6 kcal mol^{-1} greater than that for the central nitrogen at the B3-LYP/6-31+G(d,p) level of theory. This is consistent with previous experimental observations for the preferred protonation at the nitrile nitrogen in the topochemical solid-state transformation of ammonium dicyanamide into dicyan-diamide.[65] The reduced electron density at the imine-carbon makes it susceptible to nucleophilic attack by NO_3^-, which is calculated to be exothermic by 5.4 kcal mol^{-1}:

(2)
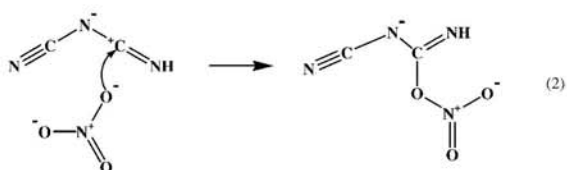
Subsequent 1,3-shift of NO_2 to the terminal nitrogen, can lead to the formation of a C=O double bond and reaction 3 is calculated to be exothermic by 34.5 kcal mol^{-1}:


(3)
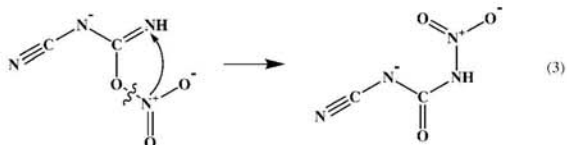
The above reaction sequence is similarly possible starting at the other nitrile nitrogen to form the dinitrobiuret (DNB) anion:

(4)

(5)
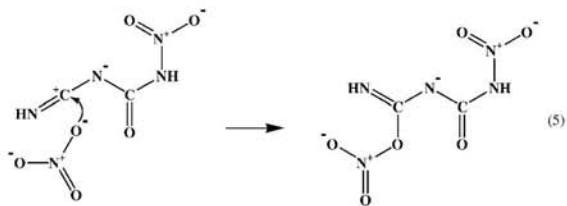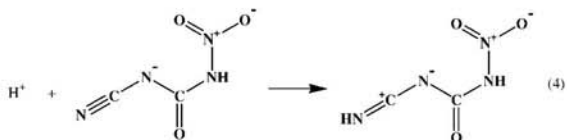
Because of the number of atoms in these molecules, the thermochemistry was not calculated for these species. However, the enthalpies of reactions 4−6 are likely to be comparable to reactions 1−3. Final protonation at the central nitrogen will produce DNB:

The results of the present calculations tabulated in Table 1 show that the crucial NO_3^- addition step of reaction 3 and subsequent rearrangement to form the amide linkage of reaction 4 are

(6)

(7)
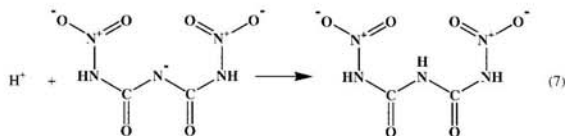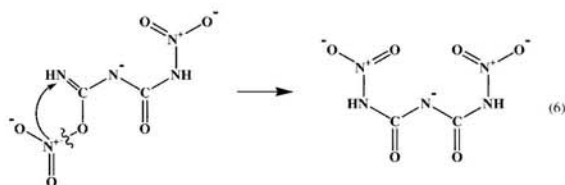
energetically favorable as are many of the protonation steps. Other, alternate and energetically possible mechanistic routes for DNB formation, particularly in nitric acid solutions, could involve either attack by the weaker H_2O nucleophile at the imine-carbon of NCN=C=NH followed by NO_2^+ addition and subsequent deprotonation to form nitrobiuret (NB),[66] or the NCN=C=NH intermediate may first undergo another protonation followed by NO_3^- addition/rearrangement reactions to yield the NB. These possibilities and the reaction dynamics of DNB formation and decomposition are currently being studied using ab initio methods to determine reaction enthalpies, barrier heights, transition state properties, etc.

The thermal decomposition of DNB has previously been shown to produce CO_2, N_2O, and HNCO,[67] the same products that we have observed in this work:

(8)
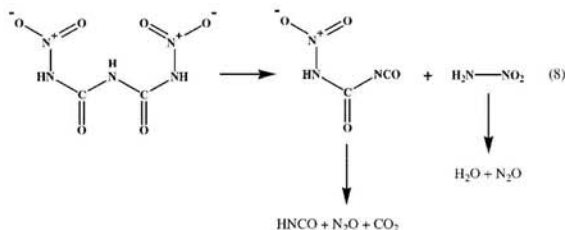
The production of CO_2, N_2O, and HNCO from the derivative intermediate and N_2O and H_2O from the nitramide intermediate in reaction 8 must occur through a multistep process, and the decomposition of these chemically labile species may be acid catalyzed. The proposed dicyanamide/WFNA reaction mechanism is consistent with the lack of any HCN or H_2NCN in our gas-phase FTIR spectra. Observation of only isocyanic acid, HNCO, and not of its higher energy isomers is consistent with their known thermal instabilities above ~100 °C.[68] Treatment of $(NaN(CN)_2)$ with 34% and 68% HNO_3 solutions both resulted in similar product evolution as seen in Figure 5, which is consistent with DNB formation under concentrated acid conditions. Our positive biuret reaction tests provide strong evidence for a peptide like functionality, −HN(O=C)NHC(=O)NH−, in the reaction intermediate. This supports the stance that it is the reaction of dicyanamide anion that initiates the decomposition of the IL salt, and oxidation of the cation becomes important only later after ignition has occurred in WFNA.

HNCO is known to react in the gas phase with water to form CO_2 and ammonia:[68,69]

$$H_2O + HNCO \rightarrow NH_3 + CO_2 \qquad (9)$$
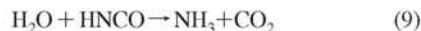
Ammonia can react very rapidly with the nitric acid to form NH_4NO_3 which could be why it was not detected in our FTIR

Appendix
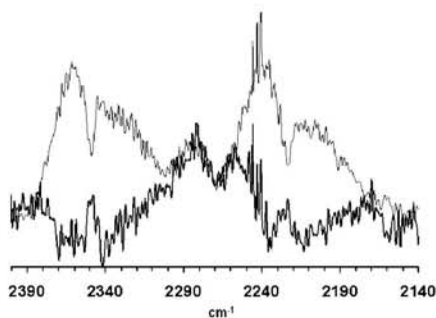
Figure 6. Difference product spectrum of BMIM dicyanamide reacting with WFNA. The dark line is the spectrum of HNCO when the CO_2 and N_2O contributions are subtracted out.
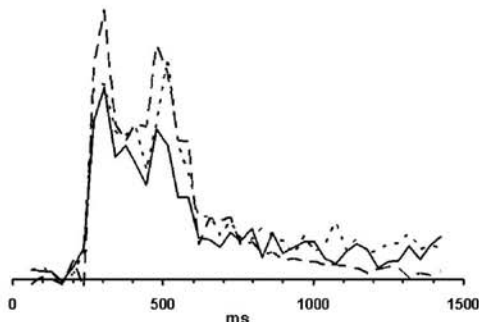
Figure 7. Product time profiles in the reaction of BMIM dicyanamide with WFNA: CO_2 (solid), HNCO (dashed), and N_2O (dotted). Data shown is for case when mixture did not ignite.
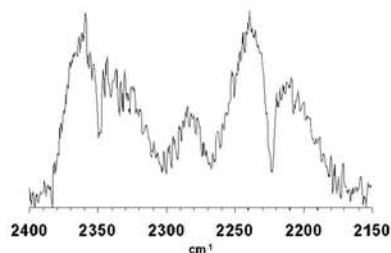
Figure 8. IR product spectrum of sodium dicyanamide reacting with WFNA. Note that the evolution of CO_2, N_2O, and HNCO is similar to Figure 5.

setup. Here, corresponding hydrolytic decomposition in the condensed phase, $H_3O^+ + HNCO \rightarrow NH_4^+ + CO_2$, would also be consistent with lack of NH_3 gas-phase signals. Thermal decomposition of NH_4NO_3 is known to be accelerated in strong mineral acids and can lead to additional N_2O formation.[70] Thus, in the case if HNCO reacts to completion in nitric acid solution, the maximum $[CO_2]/[N_2O]$ ratio possible would be 2/3 as shown below:

$$NaN(CN)_2 + 4HNO_3 \rightarrow 2CO_2 + 3N_2O + 2H_2O + NaNO_3$$

$$(10)$$
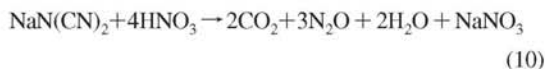
Gas-phase detection of HNCO in our drop-test experiments would suggest that the observed CO_2/N_2O signal represents a ratio less than 2/3 during the preignition phase and that possibly further reactions of HNCO and/or other vapors from DNB decomposition lead to the gas-phase ignition of the IL fuels and salts studied here as seen in Figure 2c.[67,71] The difference
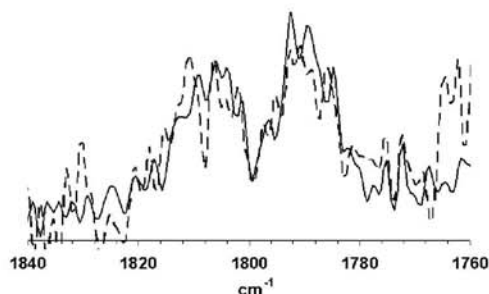
Figure 9. IR product spectrum of 1-propargyl-3-methyl imidazolium dicyanamide (solid) and 1-allyl-3-methyl-imidazolium dicyanamide (dashed) reacting with WFNA showing possible unsaturated species peak near 1800 cm^{-1}.
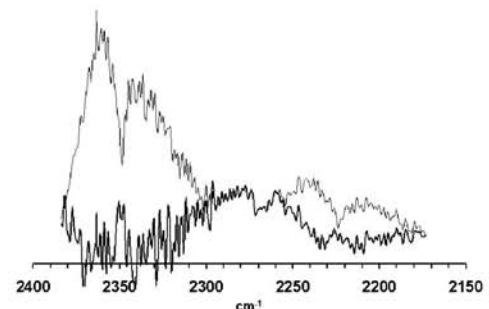
**Figure 10.** IR product spectrum of silver cyanate (AgOCN) reacting with WFNA. Note that the evolution of CO_2 and HNCO is similar to that shown in Figure 5, but N_2O production is less. The dark line is the difference spectrum for HNCO.

spectrum in Figure 6 shows the infrared spectrum of HNCO formed in the reaction of WFNA with 1-butyl-3-methyl-imidazolium dicyanamide, Figure 8 shows product spectrum for WFNA with sodium dicyanamide, and Figure 10 shows the difference spectrum when silver cyanate (AgOCN) is reacted with WFNA. The ratio of intensities of CO_2/N_2O in Figure 10 is different from that in Figure 8 indicating a different reaction stoichiometry than for the dicyanamides, with less N_2O formation since its source can only be from hydrolysis of HNCO formed in the exothermic condensed phase reaction of AgOCN with nitric acid. Observation of only HNCO in the gas phase would be consistent with its known stability relative to HOCN or HCNO. The band shape at 2271 cm^{-1} in Figure 10 is similar to that in Figure 8, further confirming that indeed HNCO is released in the dicyanamide/nitric acid systems. No visible flames were observed in AgOCN/WFNA tests.

The effect of nitro-substitution for cyano groups on the dicyanamide anion reactivity with WFNA was investigated by reacting WFNA with silver nitrocyanamide or potassium dinitramide. Significant gaseous products were observed for the dinitramide salt, in which N_2O production results from acid catalyzed (and/or thermal) decomposition of the dinitramic acid[72] without ignition:

$$KN(NO_2)_2 + HNO_3 \rightarrow [HN(NO_2)_2 \text{ or } N(NO_2)NOOH] +$$
$$KNO_3 \quad (11)$$

$$N(NO_2)NOOH + H^+ \rightarrow N_2O + H_2O + NO_2^+ \quad (12)$$

$$H_2O + NO_2^+ \rightarrow H^+ + HNO_3 \quad (13)$$

Appendix

FTIR Studies in Hypergolic Ignition of Ionic Liquids

J. Phys. Chem. A, Vol. 112, No. 34, 2008 **7823**

$$HN(NO_2)_2 + \Delta \rightarrow N_2O + HNO_3 \qquad (14)$$
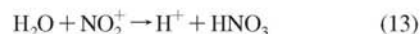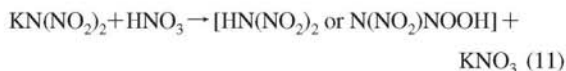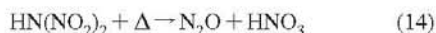
The ab initio calculations indicate that both protonation of the central nitrogen followed by a second protonation on the nitro-oxygen or double protonation on the nitro-oxygen can cause the structure to dissociate to N_2O, H_2O, and NO_2^+.[73] ΔH for this reaction is -205.5 kcal mol^{-1}.

$$HN(NO_2)_2 + H^+ \rightarrow N_2O + H_2O + NO_2^+ \qquad (15)$$
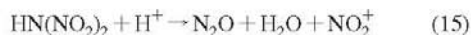
Silver nitrocyanamide, 1-methyl-4-amino-1,2,4-triazolium nitrocyanamide, and 1-allyl-4-amino-1,2,4-triazolium nitrocyanamide failed to ignite in our acid drop tests. From Table 1, the lowest energy gas-phase structure for the protonation of the nitrocyanamide anion is on the nitro-oxygen. If this species is subsequently protonated at the central nitrogen, analogous to the dinitramide decomposition, the products would be H_2O, N_2O, and CN^+:

$$NCN(NO_2H) + H^+ \rightarrow N_2O + H_2O + CN^+ \qquad (16)$$
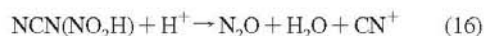
However, the energetics of forming CN^+ versus NO_2^+ is much less favorable, and reaction 16 is higher in energy than reaction 15 by at least 210 kcal mol^{-1}, which is likely why there is no N_2O evolution upon reaction of HNO_3 with nitrocyanamide. In previous work on decomposition of nitrocyanamide in strong mineral acids,[66] no N_2O or any other gaseous products were seen, consistent with our present observations. This suggests that unlike in the above dinitramide case, where double protonation can lead to exothermic decomposition to give N_2O via reaction 15, here this step does not compete with protonation at the -CN site. Previously the mechanism for nitrocyanamide/acid reaction in which protonation at the nitrile nitrogen occurs followed by nucleophilic attack by H_2O at the carbon and subsequent OH migration to form nitrourea (NU) has been proposed.[66] Nitrourea would remain in the condensed phase. Perhaps the amount of heat generated upon formation of nitrourea is insufficient to promote higher energy reactions and cause either gas evolution (i.e., N_2O) or ignition. Also, the decomposition of NU or further nitration of NU to give dinitrourea (DNU) must both be slow in our drop tests, since DNU is thermally unstable and should also give gaseous N_2O and CO_2.

The allyl-, propargyl-, and (3-butenyl)- functionalized methyl-imidazolium dicyanamides display very violent ignitions with WFNA, giving off a white flash, rather than a typically yellow flash, indicating a hotter temperature in the ignition. Evidence of pyrolytic decomposition of the cation was also seen in the high-speed videos in which copious production of sootlike matter upon ignition was detected. Initially, these functional groups were introduced to try and trigger the fuel-rich cation to ignite. However, now that the dicyanamide anion is the trigger for the ignition, the cation can be tailored for the best overall properties of the ionic liquid. For example, the allyl-, propargyl-, and (3-butenyl)- functionalized methyl-imidazolium dicyanamides are liquids at room temperature (rt), while the (2-pentynyl)- analogue is a solid at rt. The anion reacts to give off significant heat in the fast formation of CO_2 and N_2O, which causes subsequent decomposition of the cation. The appearance of an unsaturated C=C stretch might indicate that the addition of unsaturated functional groups causes the production of smaller, unsaturated hydrocarbons in the gas phase which can greatly aid in combustion once the temperature threshold is reached (evidence for this was seen as secondary ignition flashes in the high-speed video recordings). This peak is only seen in the allyl- and propargyl-functionalized methyl-imidazolium

dicyanamide species, and not in the corresponding (3-butenyl)-system, and thus more work is needed to uncover the details of how substitution affects the decomposition/oxidation mechanisms of the heterocyclic cation.

Conclusions

The hypergolic ignition of dicyanamide ionic liquids upon reaction with fuming nitric acid has been demonstrated, and it has been shown that the anion reaction is responsible for initiating the ignition. The evolution of CO_2, N_2O, and HNCO during preignition indicates a complex reaction mechanism, perhaps through dinitrobiuret and nitramide intermediates. Evidence for the former was confirmed in the biuret reaction test which was only positive for the dicyanamide reactions and not with any of the other anions studied here. In this work we have shown that the initial reactivity of the anions, $^-N(CN)_2$, $^-NNO_2(CN)$, and $^-N(NO_2)_2$, with WFNA varies dramatically with NO_2 substitution. Similarly, it may also be possible to affect the cation reactivity by suitable chemical substitutions, so as to tailor its oxidation rate. Further spectroscopic probing of products and intermediates during the preignition and ignition phases and additional ab initio calculations will be valuable in providing mechanistic insight on how IL-dicyanamides undergo combustion when treated with WFNA and IRFNA.

Supporting Information Available: Video (one mpg-file) showing hypergolic ignition of 1-propargyl-3-methyl-imidazolium dicyanamide in WFNA. This material is available free of charge via the Internet at http://pubs.acs.org.

References and Notes

(1) See for example: Smiglak, M.; Metelen, A.; Rogers, R. D. *Acc. Chem. Res.* **2007**, *40*, 1182, and references therein.

(2) Kelkar, M. S.; Maginn, E. J. *J. Phys. Chem. B* **2007**, *111*, 9424.

(3) Deetlefs, M.; Seddon, K. R.; Shara, M. *Phys. Chem. Chem. Phys.* **2006**, *8*, 642.

(4) Eike, D. M.; Brennecke, J. F.; Maginn, E. J. *Green Chem.* **2003**, *5*, 323.

(5) Katritzky, A. R.; Jain, R.; Lomaka, A.; Petrukhin, R.; Karelson, M.; Visser, A. E.; Rogers, R. D. *J. Chem. Inf. Comput. Sci.* **2002**, *42*, 225.

(6) Zhang, S.; Ning, S.; Xuezhong, H.; Xingmei, L.; Xianping, Z. *J. Phys. Chem. Ref. Data* **2006**, *35*, 1475.

(7) Gutowski, K. E.; Holbrey, J. D.; Rogers, R. D.; Dixon, D. A. *J. Phys. Chem. B* **2005**, *109*, 23196.

(8) Hawkins, T. W. *Ionic Liquids and their Applications: Pathways and Bottlenecks to their Use*; AFOSR Contractors Workshop, 2006, Tuscaloosa, AL.

(9) Scammells, P. J.; Scott, J. L. D. S. R. *Aust. J. Chem.* **2005**, *58*, 155.

(10) Rogers, R. D.; Voth, G. A. *Acc. Chem. Res.* **2007**, *41*, 1077. and articles therein on the special issue, "Ionic Liquids"

(11) Wishart, J. F.; Castner, E. W. *J. Phys. Chem. B* **2007**, *111*, 4369. and articles therein on the special issue, "The Physical Chemistry of Ionic Liquids"

(12) Macfarlane, D. R.; Meakin, P.; Sun, J.; Amini, N.; Forsyth, M. *J. Phys. Chem. B* **1999**, *103*, 4164.

(13) Ngo, H. L.; LeCompte, K.; Hargens, L.; McEwen, A. B. *Thermochim. Acta* **2000**, *357*, 97.

(14) Xie, W.; Xie, R.; Pan, W.-P.; Hunter, D.; Koene, B.; Tan, L.-S.; Vaia, R. *Chem. Mater.* **2002**, *14*, 4837.

(15) Fredlake, C. P.; Crosthwaite, J. M.; Hert, D. G.; Aki, S. N. V. K.; Brennecke, J. F. *J. Chem. Eng. Data* **2004**, *49*, 954.

(16) Baranyai, K. J.; Deacon, G. B.; Macfarlane, D. R.; Pringle, J. M.; Scott, J. L. *Aust. J. Chem.* **2004**, *57*, 145.

(17) Macfarlane, D. R.; Pringle, J. M.; Johansson, K. M.; Forsyth, S. A.; Forsyth, M. *Chem. Commun.* **2006**, 1905.

Appendix

(18) Huddleston, J. G.; Visser, A. E.; Reichert, W. M.; Willauer, H. D.; Broker, G. A.; Rogers, R. D. *Green Chem.* **2001**, *3*, 156.

(19) Holbrey, J. D.; Seddon, K. R. *J. Chem. Soc., Dalton Trans.* **1999**, 2133.

(20) Earle, M. J.; Esperanca, J. M. S. S.; Gilea, M. A.; Lopes, J. N. C.; Rebelo, L. P. N.; Magee, J. W.; Seddon, K. R.; Widegren, J. A. *Nature* **2006**, *439*, 831.

(21) Armstrong, J. P.; Hurst, C.; Jones, R. G.; Licence, P.; Lovelock, K. R. J.; Satterley, C. J.; Villar-Garcia, I. J. *Phys. Chem. Chem. Phys.* **2007**, *9*, 982.

(22) Leal, J. P.; Esperanca, J. M. S. S.; Minas de Piedade, M. E.; Lopes, J. N. C.; Rebelo, L. P. N.; Seddon, K. R. *J. Phys. Chem. A* **2007**, *111*, 6176.

(23) Strasser, D.; Goulay, F.; Kelkar, M. S.; Maginn, E. J.; Leone, S. R. *J. Phys. Chem. A* **2007**, *111*, 3191.

(24) Emel'yanenko, V. N.; Verevkin, S. P.; Heintz, A. *J. Am. Chem. Soc.* **2007**, *129*, 3931.

(25) Zaitsau, D. H.; Kabo, G. J.; Strechan, A. A.; Paulechka, Y. U.; Tsersich, A.; Verevkin, S. P.; Heintz, A. *J. Phys. Chem. A* **2006**, *110*, 7303.

(26) Gutowski, K. E.; Rogers, R. D.; Dixon, D. A. *J. Phys. Chem. A* **2006**, *110*, 11890.

(27) Sengupta, D.; Raman, S. *Propellants Explos. Pyrotech.* **2007**, *32*, 338.

(28) Sutton, G. P. *J. Propul. Power* **2003**, *6*, 978.

(29) Sutton, G. P. *J. Propul. Power* **2003**, *6*, 1008.

(30) Catoire, L.; Chaumeix, N.; Paillard, C. *J. Propul. Power* **2004**, *20*, 87.

(31) Frank, I.; Hammer, A.; Klapotke, T. M.; Nonnenberg, C. *Propellants Explos. Pyrotech.* **2005**, *30*, 44.

(32) McQuaid, M. J.; Ishikawa, Y. *J. Phys. Chem. A* **2006**, *110*, 6129.

(33) Osmond, A.; Catoire, L.; Klapotke, T. M.; Vaghjiani, G. L.; Swihart, M. T. *Propellants Explos. Pyrotech.* **2008**, *33*, 209.

(34) Seamans, T. F.; Vanpee, M.; Agosta, V. D. *AIAA J.* **1967**, *5*, 1616.

(35) Nonnenberg, C.; Frank, I.; Klapotke, T. M. *Angew. Chem., Int. Ed.* **2004**, *43*, 4586.

(36) Catoire, L.; Chaumeix, N.; Pichon, S.; Paillard, C. *J. Propul. Power* **2006**, *22*, 120.

(37) Hampton, C. S.; Smith, J. E. J. *The Importance of Carbon, Nitrogen, and Oxygen Atomic Ratios on the Combustion of Hypergolic Bipropellants;* Paper AIAA 2005-740, 43rd AIAA Aerospace Sciences Meeting and Exhibit, Reno, NV, Copyright 2005 by the American Institute of Aeronautics and Astronautics, Inc.

(38) Daimon, W.; Tanaka, M.; Kimura, I. *Proceedings on the 20th Symposium on Combustion;* Pittsburgh, PA, 1984; pp 2065−2071.

(39) de Bonn, O.; Hammerl, A.; Klapotke, T. M.; Mayer, P.; Piotrowski, H.; Zewen, H. *Z. Anorg. Allg. Chem.* **2001**, *627*, 2011.

(40) Klapötke, T. M.; Rienäcker, C. M.; Zewen, H. *Z. Anorg. Allg. Chem.* **2002**, 628.

(41) Patil, D. G.; Jain, R.; Brill, T. B. *Propellants Explos. Pyrotech* **1992**, *17*, 260.

(42) Tuazon, E. C.; Carter, W. P. L.; Brown, R. V.; Winer, A. M.; Pitts, J. M. J. *J. Phys. Chem.* **1983**, *87*, 1600.

(43) Alfano, A.; Mills, J. D.; Vaghjiani, G. L. *Rev. Sci. Instrum.* **2006**, *77*, 45109.

(44) Schneider, S.; Hawkins, T. W.; Rosander, M.; Mills, J. D.; Vaghjiani, G. L.; Chambreau, S. D. *Z. Inorg. Chem.* **2008**, *47*, 6082.

(45) Lowry, O. H.; Rosebrough, N. J.; Farr, A. L.; Randall, R. J. *J. Biol. Chem.* **1951**, *193*, 265.

(46) Frisch, M. J.; Trucks, G. W.; Schlegel, H. B.; Scuseria, G. E.; Robb, M. A.; Cheeseman, J. R.; Montgomery, J. J. A.; Vreven, T.; Kudin, K. N.; Burant, J. C.; Millam, J. M.; Iyengar, S. S.; Tomasi, J.; Barone, V.; Mennucci, B.; Cossi, M.; Scalmani, G.; Rega, N.; Petersson, G. A.; Nakatsuji, H.; Hada, M.; Ehara, M.; Toyota, K.; Fukuda, R.; Hasegawa, J.; Ishida, M.; Nakajima, T.; Honda, Y.; Kitao, O.; Nakai, H.; Klene, M.; Li, X.; Knox, J. E.; Hratchian, H. P.; Cross, J. B.; Bakken, V.; Adamo, C.; Jaramillo, J.; Gomperts, R.; Stratmann, R. E.; Yazyev, O.; Austin, A. J.; Cammi, R.; Pomelli, C.; Ochterski, J. W.; Ayala, P. Y.; Morokuma, K.; Voth, G. A.; Salvador, P.; Dannenberg, J. J.; Zakrzewski, V. G.; Dapprich, S.; Daniels, A. D.; Strain, M. C.; Farkas, O.; Malick, D. K.; Rabuck, A. D.; Raghavachari, K.; Foresman, J. B.; Ortiz, J. V.; Cui, Q.; Baboul, A. G.; Clifford, S.; Cioslowski, J.; Stefanov, B. B.; Liu, G.; Liashenko, A.; Piskorz, P.; Komaromi, I.; Martin, R. L.; Fox, D. J.; Keith, T.; Al-Laham, M. A.; Peng, C. Y.; Nanayakkara, A.; Challacombe, M.; Gill, P. M. W.; Johnson, B.; Chen, W.; Wong, M. W.; Gonzalez, C.; Pople, J. A. *Gaussian 03;* revision C.02; Gaussian, Inc.: Wallingford, CT, 2004.

(47) Scott, A. P.; Radom, L. *J. Phys. Chem.* **1996**, *100*, 16502.

(48) Dows, D. A.; Pimentel, G. C. *J. Chem. Phys.* **1955**, *23*, 1258.

(49) Hawkins, T. W.; Rosander, M.; Vaghjiani, G. L.; Chambreau, S. D.; Drake, G.; Schneider, S. *Energy Fuels* **2008**, *22*, 2871.

(50) Lucien, H. W. *J. Am. Chem. Soc.* **1958**, *80*, 4458.

(51) PNNL Infrared Spectral Library. http://nwir.pnl.gov/ (accessed Sept 2007).

(52) Bark, M.; Winnewisser, M. *Chem. Phys. Lett.* **1986**, *123*, 382.

(53) Wagner, G. D. J.; Wagner, E. L. *J. Chem. Phys.* **1960**, *64*, 1480.

(54) Herzberg, G.; Reid, C. *Discuss. Faraday Soc.* **1950**, *9*, 92.

(55) Nelson, P. F.; Li, C.-Z.; Ledesma, E. *Energy Fuels* **1996**, *10*, 264.

(56) Stiner, D. A.; Polo, S. R.; McCubbin, T. K. *J. Mol. Spectrosc.* **1983**, *98*, 453.

(57) Fischer, G.; Geith, J.; Klapotke, T. M.; Krumm, B. *Z. Naturforsch.* **2002**, *57b*, 19.

(58) Ferretti, E. L.; Rao, K. N. *J. Mol. Spectrosc.* **1974**, *51*, 97.

(59) Grubdorf, J.; Temps, W. H. G. *Ber. Bunsenges. Phys. Chem.* **1997**, *101*, 134.

(60) Su, H.; Kong, F.; Chen, B.; Huang, M.-B.; Lui, Y. *J. Chem. Phys.* **2000**, *113*, 1885.

(61) Crowley, J. N.; Sodeau, J. R. *J. Phys. Chem.* **1989**, *93*, 3100.

(62) Ruscic, B.; Berkowitz, J. *J. Chem. Phys.* **1994**, *100*, 4498.

(63) Streitweiser, A., Jr.; Heathcock, C. H. *Introduction to Organic Chemistry*, 3rd ed.;Macmillan Publishing Co.: New York, 1985.

(64) Edwards, J. O. *J. Am. Chem. Soc.* **1954**, *76*, 1540.

(65) Lotsch, B. V.; Senker, J.; Schnick, W. *Inorg. Chem.* **2004**, *43*, 895.

(66) Astrat'ev, A. A.; Kuznetsov, L. L. *Russ. J. Org. Chem.* **2002**, *38*, 1252.

(67) Geith, J.; Holl, G.; Klapotke, T. M.; Weigand, J. J. *Combust. Flame* **2004**, *139*, 358.

(68) Fisher, G.; Geith, J.; Klapotke, T. M.; Krumm, B. *Z. Naturforsch.* **2002**, *57b*, 19.

(69) Belson, D. J.; Strachan, A. N. *Chem. Soc. Rev.* **1982**, *11*, 41.

(70) See for example: Sun, J.; Sun, Z.; Wang, Q.; Ding, H.; Wang, T.; Jiang, C. *J. Hazard. Mater.* **2005**, *127B*, 204, and references therein.

(71) Geith, J.; Klapotke, T. M. *J. Mol. Struct. (THEOCHEM.)* **2001**, *538*, 29.

(72) Lobbecke, S.; Keicher, T.; Krause, H.; Pfeil, A. *Solid State Ionics* **1997**, *101*, 945.

(73) Politzer, P.; Seminaro, J. P. *Chem. Phys. Lett.* **1993**, *216*, 348.

JP8038175

Appendix

This Page Intentionally Left Blank

Appendix

Tunable Wavelength Soft Photoionization of Ionic Liquid Vapors

Daniel Strasser,[*,†,⊥] **Fabien Goulay,**[†,#] **Leonid Belau,**[‡] **Oleg Kostko,**[‡] **Christine Koh,**[†] **Steven D. Chambreau,**[§] **Ghanshyam L. Vaghjiani,**[∥] **Musahid Ahmed,**[‡] **and Stephen R. Leone**[†,‡]

Departments of Chemistry and Physics, University of California, Berkeley, California 94720, Chemical Sciences Division, Lawrence Berkeley National Laboratory, Berkeley, California 94720, ERC Incorporated and Air Force Research Laboratory, Edwards Air Force Base, California 93524

Received: October 11, 2009; Revised Manuscript Received: November 8, 2009

Combined data of photoelectron spectra and photoionization efficiency curves in the near threshold ionization region of isolated ion pairs from [emim][Tf$_2$N], [emim][Pf$_2$N], and [dmpim][Tf$_2$N] ionic liquid vapors reveal small shifts in the ionization energies of ion-pair systems due to cation and anion substitutions. Shifts toward higher binding energy following anion substitution are attributed to increased electronegativity of the anion itself, whereas shifts toward lower binding energies following cation substitution are attributed to an increase in the cation–anion distance that causes a lower Coulombic binding potential. The predominant ionization mechanism in the near threshold photon energy region is identified as dissociative ionization, involving the dissociation of the ion pair and the production of intact cations as the positively charged products.

Introduction

Room-temperature ionic liquids (ILs) are salts with a melting point near or below ambient temperatures.[1] They are typically based on bulky multiatom cations and anions that restrict the cation–anion distance of closest approach, thus limiting their Coulombic attraction and consequently also lowering their melting temperature even below room temperature. Melting temperatures of room temperature ILs can therefore be much lower than those of salts based on atomic ions, such as NaCl, which has a melting temperature of 1074 K. In addition to having low melting temperatures, ILs have a number of unique properties, including excellent solvation ability, extraordinarily low volatility, and high thermal stability.[1–9] Because the physical and chemical properties of ILs can be varied by the choices of the cation and anion pair,[1] they can be used for many applications such as fuel cells,[3–5] batteries,[6,7] and solar cells.[8,9] Furthermore, ILs are also used in ionic propulsion[10,11] and for hypergolic fuels[12] and various chemical extraction applications.[13] The vast number of possible anion–cation combinations[14] makes it valuable to predict IL properties rationally on the basis of their constituents,[15] and considerable experimental and theoretical work has been performed to predict and measure IL properties.[16] Ab initio calculations, used to predict the structure and interactions of ILs, are typically performed on isolated "gas-phase" systems.[17,18] It is therefore attractive to study isolated ion pairs and to examine basic IL decomposition pathways, such as dissociation or ionization. Because ILs are generally perceived as "green solvents", their decomposition pathways can lead to a variety of products that need to be considered in specific applications. Given recent works[19] demonstrating the distillation of selected families of ILs, we subsequently prepared molecular beams of IL vapor, providing a gas-phase target of isolated ion-pair species to obtain the photoelectron (PE) spectrum of [emim][Tf$_2$N] vapor.[20] The direct comparison of our [emim]-[Tf$_2$N] PE spectrum with previously measured PE spectra of a [bmim][Tf$_2$N] liquid surface[21,22] provided important evidence of the ion-pair nature of IL vapor.[20] Other recent studies aimed at investigating the properties of IL vapor also include line of sight mass spectroscopy,[23,24] IR spectroscopy,[25] and matrix-isolated FTIR spectroscopy.[26] Moreover, mass spectra of cation- and anion-substituted ILs[20] showed that the ionization of these isolated IL ion pairs by absorption of a single 23.2 eV photon, which is >14 eV above the ionization threshold, results in fragmentation with a predominant product of the intact cations. Interestingly, no signal is detected for the ionized parent ion-pair mass; that is, the removal of an electron from the ion-pair system results in the dissociation of the ion pair. Because those results were obtained with a photon energy that is 14.3 eV higher than the energy needed to remove an electron from the ion pair, which could provide ample energy to detach an electron as well dissociate the molecule, near threshold investigations are required. Field-induced IL ionization studies recently provided evidence of the possible formation of undissociated parent ion systems with the combined mass of the cation and anion.[27]

Here we present a study of the near threshold soft photoionization of isolated ion pairs with tunable photon energies between 8.3 and 9.5 eV. Electronic structure changes following cation and anion substitutions are presented and discussed in terms of the observed binding energy shifts. Starting from the commonly used [1-ethyl-3-methylimidazolium][bis(trifluoromethylsulfonyl)imide)] ([emim][Tf$_2$N]) room-temperature IL, shown in Figure 1, the [emim]$^+$ cation is substituted by the bulkier imidazolium-based 1,2-dimethyl-3-propylimidazolium ion ([dmpim]$^+$), and the [Tf$_2$N]$^-$ anion is substituted by the bis(pentafluoroethylsulfonyl)imide ion ([Pf$_2$N]$^-$), which has a higher fluorine content. Single-photon near threshold photoionization mass-spectra and photoionization efficiency (PIE) curves, obtained at the Advanced Light Source chemical dynamics beam line in the near threshold region, are presented for the cation-

* Corresponding author. E-mail: strasser@chem.ch.huji.ac.il.
† University of California.
‡ Lawrence Berkeley National Laboratory.
§ ERC Incorporated, Edwards Air Force Base.
∥ Air Force Research Laboratory, Edwards Air Force Base.
⊥ Present affiliation: Institute of Chemistry, Hebrew University, Jerusalem 91904, Israel.
Present affiliation: Combustion Research Facility, Sandia National Laboratories, Livermore, California 94551.

APPENDIX

J. Phys. Chem. A **2010,** *114,* 879–883

879

Tunable Wavelength Soft Photoionization of Ionic Liquid Vapors

Daniel Strasser,[*,†,⊥] **Fabien Goulay,**[†,#] **Leonid Belau,**[‡] **Oleg Kostko,**[‡] **Christine Koh,**[†] **Steven D. Chambreau,**[§] **Ghanshyam L. Vaghjiani,**[‖] **Musahid Ahmed,**[‡] **and Stephen R. Leone**[†,‡]

Departments of Chemistry and Physics, University of California, Berkeley, California 94720, Chemical Sciences Division, Lawrence Berkeley National Laboratory, Berkeley, California 94720, ERC Incorporated and Air Force Research Laboratory, Edwards Air Force Base, California 93524

Received: October 11, 2009; Revised Manuscript Received: November 8, 2009

Combined data of photoelectron spectra and photoionization efficiency curves in the near threshold ionization region of isolated ion pairs from [emim][Tf_2N], [emim][Pf_2N], and [dmpim][Tf_2N] ionic liquid vapors reveal small shifts in the ionization energies of ion-pair systems due to cation and anion substitutions. Shifts toward higher binding energy following anion substitution are attributed to increased electronegativity of the anion itself, whereas shifts toward lower binding energies following cation substitution are attributed to an increase in the cation−anion distance that causes a lower Coulombic binding potential. The predominant ionization mechanism in the near threshold photon energy region is identified as dissociative ionization, involving the dissociation of the ion pair and the production of intact cations as the positively charged products.

Introduction

Room-temperature ionic liquids (ILs) are salts with a melting point near or below ambient temperatures.[1] They are typically based on bulky multiatom cations and anions that restrict the cation−anion distance of closest approach, thus limiting their Coulombic attraction and consequently also lowering their melting temperature even below room temperature. Melting temperatures of room temperature ILs can therefore be much lower than those of salts based on atomic ions, such as NaCl, which has a melting temperature of 1074 K. In addition to having low melting temperatures, ILs have a number of unique properties, including excellent solvation ability, extraordinarily low volatility, and high thermal stability.[1−9] Because the physical and chemical properties of ILs can be varied by the choices of the cation and anion pair,[1] they can be used for many applications such as fuel cells,[3−5] batteries,[6,7] and solar cells.[8,9] Furthermore, ILs are also used in ionic propulsion[10,11] and for hypergolic fuels[12] and various chemical extraction applications.[13] The vast number of possible anion−cation combinations[14] makes it valuable to predict IL properties rationally on the basis of their constituents,[15] and considerable experimental and theoretical work has been performed to predict and measure IL properties.[16] Ab initio calculations, used to predict the structure and interactions of ILs, are typically performed on isolated "gas-phase" systems.[17,18] It is therefore attractive to study isolated ion pairs and to examine basic IL decomposition pathways, such as dissociation or ionization. Because ILs are generally perceived as "green solvents", their decomposition pathways can lead to a variety of products that need to be considered in specific applications. Given recent works[19] demonstrating the distillation of selected families of ILs, we subsequently prepared molecular

beams of IL vapor, providing a gas-phase target of isolated ion-pair species to obtain the photoelectron (PE) spectrum of [emim][Tf_2N] vapor.[20] The direct comparison of our [emim]-[Tf_2N] vapor PE spectrum with previously measured PE spectra of a [bmim][Tf_2N] liquid surface[21,22] provided important evidence of the ion-pair nature of IL vapor.[20] Other recent studies aimed at investigating the properties of IL vapor also include line of sight mass spectroscopy,[23,24] IR spectroscopy,[25] and matrix-isolated FTIR spectroscopy.[26] Moreover, mass spectra of cation- and anion-substituted ILs[20] showed that the ionization of these isolated IL ion pairs by absorption of a single 23.2 eV photon, which is >14 eV above the ionization threshold, results in fragmentation with a predominant product of the intact cations. Interestingly, no signal is detected for the ionized parent ion-pair mass; that is, the removal of an electron from the ion-pair system results in the dissociation of the ion pair. Because those results were obtained with a photon energy that is 14.3 eV higher than the energy needed to remove an electron from the ion pair, which could provide ample energy to detach an electron as well dissociate the molecule, near threshold investigations are required. Field-induced IL ionization studies recently provided evidence of the possible formation of undissociated parent ion systems with the combined mass of the cation and anion.[27]

Here we present a study of the near threshold soft photoionization of isolated ion pairs with tunable photon energies between 8.3 and 9.5 eV. Electronic structure changes following cation and anion substitutions are presented and discussed in terms of the observed binding energy shifts. Starting from the commonly used [1-ethyl-3-methylimidazolium][bis(trifluoromethylsulfonyl)imide)] ([emim][Tf_2N]) room-temperature IL, shown in Figure 1, the [emim]$^+$ cation is substituted by the bulkier imidazolium-based 1,2-dimethyl-3-propylimidazolium ion ([dmpim]$^+$), and the [Tf_2N]$^-$ anion is substituted by the bis(pentafluoroethylsulfonyl)imide ion ([Pf_2N]$^-$), which has a higher fluorine content. Single-photon near threshold photoionization mass-spectra and photoionization efficiency (PIE) curves, obtained at the Advanced Light Source chemical dynamics beam line in the near threshold region, are presented for the cation-

---

* Corresponding author. E-mail: strasser@chem.ch.huji.ac.il.
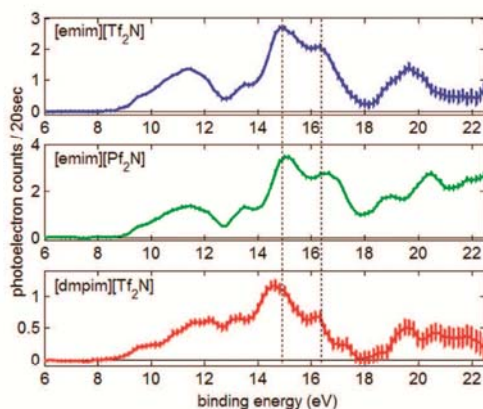† University of California.
‡ Lawrence Berkeley National Laboratory.
§ ERC Incorporated, Edwards Air Force Base.
‖ Air Force Research Laboratory, Edwards Air Force Base.
⊥ Present affiliation: Institute of Chemistry, Hebrew University, Jerusalem 91904, Israel.
Present affiliation: Combustion Research Facility, Sandia National Laboratories, Livermore, California 94551.

Appendix

Figure 3. Photoelectron binding energy spectra of IL vapor taken with 23.2 eV photons (53.7 nm) for [emim][Tf$_2$N], [emim][Pf$_2$N], and [dmpim][Tf$_2$N].
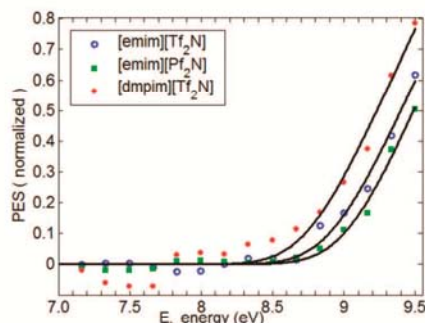
Figure 4. Detail of the PE spectra near the ionization threshold of [emim][Tf$_2$N], [emim][Pf$_2$N], and [dmpim][Tf$_2$N] obtained with 23.2 eV photons (53.7 nm).

[emim][Tf$_2$N] and [emim][Pf$_2$N] on the normalized scale. The solid lines in Figure 4 show fits of the PE spectra in the near threshold region. We use the simplest threshold function to fit the data, which vanishes below the threshold energy and rises linearly, as $\alpha(E - E_0)$, for binding energies beyond the threshold ionization energy. Here E_0 is the fitted threshold energy and α is a fitted overall normalization factor, which depends on the photoionization cross section, photon flux, and sample density. This simple threshold function is convoluted with a 250 meV Gaussian. The width of the Gaussian was also fitted to the data and reflects the combined effect of internal excitation of the hot ion pairs, the bandwidth of the light source, and the experimental response function of the PE spectrometer. We find that a similar trend of binding enrgy shifts observed for peak positions can be identified in the fitted threshold ionization energies. Whereas for [emim][Tf$_2$N], the threshold ionization energy is found to be 8.9 ± 0.2 eV, the threshold for [emim][Pf$_2$N] is shifted to higher binding energies 9.0 ± 0.2 eV, and for [dmpim][Tf$_2$N], the threshold ionization energy is shifted to lower binding energies of 8.7 ± 0.35 eV. The changes in the electronic structure due to the cation and anion substitutions are small and can be mainly characterized by these slight binding energy shifts. The main sources of error in this measurement are the limited resolution of the PE spectrometer for fast electrons emitted near the ionization threshold as well as the noise due to background electrons in this PE region. The trends of the small binding energy shifts suggested by the features of the measured PE spectra are reaffirmed in the
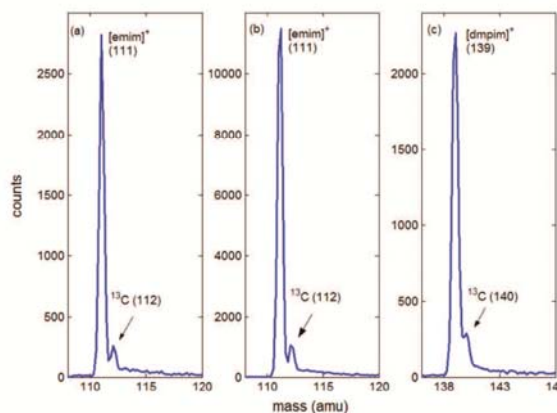

Figure 5. Near-threshold photoionization mass spectra collected with photon energies in the 8.6 to 9.5 eV range for (a) [emim][Tf$_2$N], (b) [emim][Pf$_2$N], and (c) [dmpim][Tf$_2$N].

following by the higher resolution tunable-wavelength PIE spectra measurements.

The photoionization of the IL ion pairs with 23.2 eV photons, which is used to obtain the PE spectra and results in dissociative ionization and a predominant mass peak of the respective intact cation signal in photoionization mass spectra.[20] With the implementation of tunable wavelengths at the ALS chemical dynamics beamline, it is possible to tune the ionizing photon energies near the thresholds of ionization that are revealed by the PE spectra. Therefore, a relatively soft ionization mechanism is used for examining the stability of isolated IL ion pairs. Figure 5 shows near-threshold photoionization mass spectra of [emim][Tf$_2$N], [emim][Pf$_2$N], and [dmpim][Tf$_2$N] IL vapors obtained in the near-ionization threshold region with photon energies between 8.6 and 9.5 eV. Similar to mass spectra obtained with higher photon energies, we find that the predominant positively charged products of the considered ion-pair systems are the respective intact cations, that is, [emim]$^+$ at mass 111 amu and [dmpim]$^+$ at mass 139 amu. It is also possible to observe the corresponding ^{13}C isotope peaks at 112 and 140 amu. The relative yields of the ^{13}C isotope peaks are in agreement with the natural isotope abundance for [emim]$^+$ with eight carbon atoms and [dmpim]$^+$ with ten carbon atoms. Despite the fact that soft photoionization, with near-threshold photon energies, was used, no parent mass peaks were observed (not shown). The excellent level of signal-to-noise allows us to assess an upper limit of better than ∼1:1000 for the relative yield of parent ions at the mass of the undissociated ion pairs compared with the observed yield of dissociated ion pair mass. This indicates that the threshold ionization energies of these isolated ion pairs coincide with the appearance energies of the intact cations produced by dissociative ionization. It is therefore concluded that the removal of the highest occupied molecular orbital (HOMO) electron from the IL ion pairs considered here leads to dissociation and formation of the intact cation.

To provide a more precise determination of the small binding energy shifts at the threshold ionization energies, for the cation and anion substitutions, we record PIE curves as a function of photon energy in the near-threshold ionization region. On the basis of the fact that only dissociative ionization is observed in the ionization threshold region, as identified by PE spectroscopy, we assume that the appearance energy of the intact cation coincides with the ionization energy. Therefore, PIE curves are constructed by recording the yield of the respective intact cation

Appendix
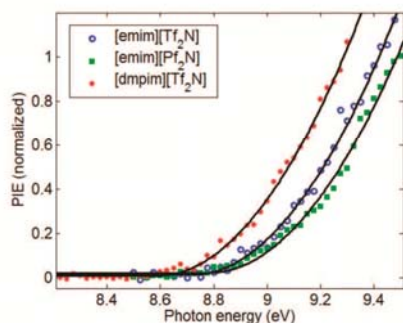
Figure 6. Near-threshold PIE spectra, showing binding energy shifts due to cation and anion substitutions.

signal normalized to the ALS photon flux, as a function of photon energy. Figure 6 shows the near-threshold PIE curves, recorded for [emim][Tf$_2$N], [emim][Pf$_2$N], and [dmpim][Tf$_2$N]. PIE curves can be compared with the integral of the PE spectra. Therefore, we fit the near threshold PIE curves with a function that is the integral of the linear threshold function we successfully used for fitting the near-threshold PE spectra, that is, vanishing yield below the threshold energy and a quadratic rise of the ionization efficiency above the threshold energy. Therefore the functional form is $1/2\alpha(E - E_0)^2$, where α is a fitted overall normalization factor, E is the photon energy, and E_0 is the fitted threshold parameter. Interestingly, this functional form that successfully describes our data is also known as the Fowler law, which was originally developed to describe photoemission from metals[31] but was found to be useful for other systems as well.[32] Similarly to the PE spectrum fitting procedure, this function is convoluted with a Gaussian resolution function, fitted to be narrower, 50 meV, and reflects the better resolution of the monochromator at the 9.0.2.3 beamline. The three data sets shown in Figure 6 are shown to be normalized by their fitted overall normalization factor, α. The solid lines in Figure 6 are the fitted threshold functions, corresponding to threshold ionization energies of 8.72 $\pm$ 0.03, 8.78 $\pm$ 0.04, and 8.59 $\pm$ 0.03 eV for [emim][Tf$_2$N], [emim][Pf$_2$N], and [dmpim][Tf$_2$N], respectively. The fitted threshold ionization energies are in good agreement with the analysis of the PE spectra within the error bars of the PE spectra analysis. Although within the experimental PE error bars of 0.2 eV, the ionization energies obtained by the PE spectra analysis are systematically higher than PIE results, which is possibly due to a small shift on the order of 0.1 eV in the PE spectrometer calibration. The results reaffirm with higher precision the trends of the small binding energy shifts observed in the PE spectra. It is important to note that for the three IL experiments, the reservoir of the ion source is kept at similar temperatures around 500 K, and thus the observed shifts are not expected to be due to different molecular beam temperatures. The substitution of the [Tf$_2$N]$^-$ anion by [Pf$_2$N]$^-$ results in a small +60 meV shift toward higher electron binding energies. We suggest that this trend may be understood in terms of increased electronegativity due to the substitution of the trifluoromethyl by pentafluoroethyl groups, leading to higher binding energy of the electron to the anion. In the case of [emim]$^+$ cation substitution by [dmpim]$^+$, the -130 meV shift is toward lower binding energies. The addition of the 2-methyl group replacing a hydrogen atom and the replacement of 3-ethyl by the bulkier 3-propyl group can act to alter the spacing between the ions, increasing the cation–anion distance and therefore reducing the Coulombic interaction between the cation and the electron of the anion. Therefore, we suggest that this

particular cation substitution can lead to the observed binding energy shift toward lower binding energies of the anions electron.

Conclusions

Isolated ion pairs in the IL vapor of three IL species were studied with a tunable synchrotron light source in the near threshold ionization region, between 8.3 and 9.5 eV photon energies as well as with 23.2 eV photons from a "table-top" high-order harmonic generation light source. The combined PE spectra, near-threshold mass spectra, and PIE curves allow us to determine ionization threshold energies and to detect small binding energy shifts due to cation and anion substitutions. Theoretical calculations are needed to provide further insight into the electronic structure and the observed binding energy shifts of gas-phase IL ion pairs.

Photoionization of the examined IL vapor predominantly leads to dissociative ionization. Photodetachment of the HOMO electron results in the dissociation of the ionized ion-pair system into a neutral fragment and the intact cation that is detected in the mass spectra measurements. Previous works using pulsed field ionization of similar IL species have showed that the ionized [cation][anion]$^+$ mass peak can be detected in positive ion mass spectra.[27] However, in the present work, even with the introduction of soft photoionization, there is no evidence of the undissociated parent system in the recorded mass spectra. One possibility is that the parent system formed by photoionization is unstable and spontaneously dissociates on a time scale that is much faster than the typical tens of microseconds between the quasi-continuous ALS light source and the pulsed TOF ion extraction in our experiments.

References and Notes

(1) *Ionic Liquids in Synthesis*; Wasserscheid, P., Welton, T., Eds.; Wiley-VCH: Weinheim, Germany, 2003.

(2) Blanchard, L. A.; Hancu, D.; Beckman, E. J.; Brennecke, J. F. Green processing using ionic liquids and CO$_2$. *Nature* **1999**, *399*, 28.

(3) Yoshizawa, M.; Xu, W.; Angell, C. A. Ionic liquids by proton transfer: vapor pressure, conductivity, and the relevance of ΔpK$_a$ from aqueous solutions. *J. Am. Chem. Soc.* **2003**, *125*, 15411.

(4) Susan, Md. A. B. H.; Noda, A.; Mitsushima, S.; Watanabe, M. Brønsted acid–base ionic liquids and their use as new materials for anhydrous proton conductors. *Chem. Commun.* **2003**, 938.

(5) de Souza, R. F.; Padilha, J. C.; Gonçalves, R. S.; Dupont, J. Room temperature dialkylimidazolium ionic liquid-based fuel cells. *Electrochem. Commun.* **2003**, *5*, 728.

(6) Shin, J.-H.; Henderson, W. A.; Passerini, S. Ionic liquids to the rescue? Overcoming the ionic conductivity limitations of polymer electrolytes. *Electrochem. Commun.* **2003**, *5*, 1016.

(7) Hu, Y. S.; Li, H.; Huang, X.; Chen, L. Novel room temperature molten salt electrolyte based on LiTFSI and acetamide for lithium batteries. *Electrochem. Commun.* **2004**, *6*, 28.

(8) Wang, P.; Zakeeruddin, S. M.; Comte, P.; Exnar, I.; Grätzel, M. Gelation of ionic liquid-based electrolytes with silica nanoparticles for quasi-solid-state dye-sensitized solar cells. *J. Am. Chem. Soc.* **2003**, *125*, 1166.

(9) Wang, P.; Wenger, B.; Humphry-Baker, R.; Moser, J.-E.; Teuscher, J.; Kantlehner, W.; Mezger, J.; Stoyanov, E. V.; Zakeeruddin, S. M.; Grätzel, M. Charge separation and efficient light energy conversion in sensitized

Appendix

mesoscopic solar cells based on binary ionic liquids. *J. Am. Chem. Soc.* **2005**, *127*, 6850.

(10) Larriba, C.; Castro, S.; de la Mora, F. J.; Lozano, P. Monoenergetic source of kilodalton ions from Taylor cones of ionic liquids. *J. Appl. Phys.* **2007**, *101*, 84303.

(11) Lozano, P. C. Energy properties of an EMI-Im ionic liquid ion source. *J. Phys. D: Appl. Phys.* **2006**, *39*, 126.

(12) Schneider, S.; Hawkins, T.; Rosander, M.; Vaghjiani, G.; Chambreau, S.; Drake, G. Ionic liquids as hypergolic fuels. *Energy Fuels* **2008**, *22*, 2871.

(13) Plechkova, N. V.; Seddon, K. R. Applications of ionic liquids in the chemical industry. *Chem. Soc. Rev.* **2008**, *37*, 123.

(14) Anderson, J. L.; Armstrong, D. W.; Wei, G.-T. Ionic liquids in analytical chemistry. *Anal. Chem.* **2006**, *78*, 2892.

(15) Weingaertner, H. Understanding ionic liquids at the molecular level: facts, problems, and controversies. *Angew. Chem., Int. Ed.* **2008**, *47*, 654.

(16) Krossing, I.; Slattery, J. M. Semi-empirical methods to predict the physical properties of ionic liquids: an overview of recent developments. *Z. Phys. Chem.* **2006**, *220*, 1343.

(17) Krischok, S.; Öttking, R.; Beenken, W. J. D.; Himmerlich, M.; Lorenz, P.; Höfft, O.; Bahr, S.; Kempter, V.; Schaefer, J. A. A comparative study on the electronic structure of the 1-ethyl-3-methylimidazolium bis(trifluoromethylsulfonyl)amide RT-ionic liquid by electron spectroscopy and first principles calculations. *Z. Phys. Chem.* **2006**, *220*, 1407.

(18) Meng, Z.; Dölle, A.; Carper, W. R. Gas phase model of an ionic liquid: semi-empirical and ab initio bonding and molecular structure. *THEOCHEM* **2002**, *585*, 119.

(19) Earle, M. J.; Esperança, J. M. S. S.; Gilea, M. A.; Lopes, J. N. C.; Rebelo, L. P. N.; Magee, J. W.; Seddon, K. R.; Widegren, J. A. The distillation and volatility of ionic liquids. *Nature* **2006**, *439*, 831.

(20) Strasser, D.; Goulay, F.; Kelkar, M. S.; Maginn, E. J.; Leone, S. R. Photoelectron spectrum of isolated ion-pairs in ionic liquid vapor. *J. Phys. Chem. A* **2007**, *111*, 3191.

(21) Höfft, O.; Bahr, S.; Himmerlich, M.; Krischok, S.; Schaefer, J. A.; Kempter, V. Electronic structure of the surface of the ionic liquid [EMIM][Tf₂N] studied by metastable impact electron spectroscopy (MIES), UPS, and XPS. *Langmuir* **2006**, *22*, 7120.

(22) Yoshimura, D.; Yokoyama, T.; Nishi, T.; Ishii, H.; Ozawa, R.; Hamaguchi, H.; Seki, K. Electronic structure of ionic liquids at the surface studied by UV photoemission. *J. Electron Spectrosc. Relat. Phenom.* **2005**, *144*, 319.

(23) Armstrong, J. P.; Hurst, C.; Jones, R. G.; Licence, P.; Lovelock, K. R. J.; Satterley, C. J.; Villar-Garcia, I. J. Vapourisation of ionic liquids. *Phys. Chem. Chem. Phys.* **2007**, *9*, 982.

(24) Lovelock, K. R. J.; Deyko, A.; Corfield, J.-A.; Gooden, P. N.; Licence, P.; Jones, R. G. Vaporisation of a Dicationic Ionic Liquid. *ChemPhysChem* **2009**, *10*, 337.

(25) Zaitsau, D. H.; Kabo, G. J.; Strechan, A. A.; Paulechka, Y. U.; Tschersich, A.; Verevkin, S. P.; Heintz, A. Experimental vapor pressures of 1-alkyl-3-methylimidazolium bis(trifluoromethylsulfonyl) imides and a correlation scheme for estimation of vaporization enthalpies of ionic liquids. *J. Phys. Chem. A* **2006**, *110*, 7303.

(26) Akai, N.; Parazs, D.; Kawai, A.; Shibuya, K. Cryogenic neon matrix-isolation FTIR spectroscopy of evaporated ionic liquids: geometrical structure of cation−anion 1:1 pair in the gas phase. *J. Phys. Chem. B* **2009**, *113*, 4756.

(27) Gross, J. H. Molecular ions of ionic liquids in the gas phase. *J. Am. Soc. Mass Spectrom.* **2008**, *19*, 1347.

(28) Corkum, P. B. Plasma perspective on strong-field multiphoton ionization. *Phys. Rev. Lett.* **1993**, *71*, 1994.

(29) Belau, L.; Wilson, K. R.; Leone, S. R.; Ahmed, M. Vacuum ultraviolet (VUV) photoionization of small water clusters. *J. Phys. Chem. A* **2007**, *111*, 10075.

(30) Nugent-Glandorf, L.; Scheer, M.; Samuels, D. A.; Bierbaum, V.; Leone, S. R. A laser-based instrument for the study of ultrafast chemical dynamics by soft x-ray-probe photoelectron spectroscopy. *Rev. Sci. Instrum.* **2002**, *73*, 1875.

(31) Fowler, R. H. The analysis of photoelectric sensitivity curves for clean metals at various temperatures. *Phys. Rev.* **1931**, *38*, 45.

(32) Wong, K.; Kresin, V. V. Photoionization threshold shapes of metal clusters. *J. Chem. Phys.* **2003**, *118*, 7141.

JP909727F

Appendix

This page intentionally left blank

APPENDIX

J. Phys. Chem. B **2010,** *114,* 1361–1367

1361

Heats of Vaporization of Room Temperature Ionic Liquids by Tunable Vacuum Ultraviolet Photoionization

**Steven D. Chambreau,[†] Ghanshyam L. Vaghjiani,*,[‡] Albert To,[§] Christine Koh,[||]
Daniel Strasser,[||,⊥] Oleg Kostko,[||] and Stephen R. Leone[||]**

*ERC, Incorporated, Edwards Air Force Base, California 93524, Air Force Research Laboratory, Edwards Air
Force Base, California 93524, Department of Civil and Environmental Engineering, University of Pittsburgh,
Pittsburgh, Pennsylvania 15261, Departments of Chemistry and Physics and Lawrence Berkeley National
Laboratory, University of California, Berkeley, California 94720*

Received: September 30, 2009; Revised Manuscript Received: December 7, 2009

The heats of vaporization of the room temperature ionic liquids (RTILs) *N*-butyl-*N*-methylpyrrolidinium
bistrifluorosulfonylimide, *N*-butyl-*N*-methylpyrrolidinium dicyanamide, and 1-butyl-3-methylimidazolium
dicyanamide are determined using a heated effusive vapor source in conjunction with single photon ionization
by a tunable vacuum ultraviolet synchrotron source. The relative gas phase ionic liquid vapor densities in the
effusive beam are monitored by clearly distinguished dissociative photoionization processes via a time-of-
flight mass spectrometer at a tunable vacuum ultraviolet beamline 9.0.2.3 (Chemical Dynamics Beamline) at
the Advanced Light Source synchrotron facility. Resulting in relatively few assumptions, through the analysis
of both parent cations and fragment cations, the heat of vaporization of *N*-butyl-*N*-methylpyrrolidinium
bistrifluorosulfonylimide is determined to be $\Delta H_{vap}(298.15 \text{ K}) = 195 \pm 19 \text{ kJ mol}^{-1}$. The observed heats of
vaporization of 1-butyl-3-methylimidazolium dicyanamide ($\Delta H_{vap}(298.15 \text{ K}) = 174 \pm 12 \text{ kJ mol}^{-1}$) and
N-butyl-*N*-methylpyrrolidinium dicyanamide ($\Delta H_{vap}(298.15 \text{ K}) = 171 \pm 12 \text{ kJ mol}^{-1}$) are consistent with
reported experimental values using electron impact ionization. The tunable vacuum ultraviolet source has
enabled accurate measurement of photoion appearance energies. These appearance energies are in good
agreement with MP2 calculations for dissociative photoionization of the ion pair. These experimental heats
of vaporization, photoion appearance energies, and *ab initio* calculations corroborate vaporization of these
RTILs as intact cation−anion pairs.

Introduction

Ionic liquids are classified as ionic salts that have melting
points at and below $T = 100$ °C. Thus, room temperature ionic
liquids (RTILs) are liquids under ambient conditions. RTILs
represent a new class of solvents that potentially can replace
highly volatile organic solvents and hydrazine-based hypergolic
fuels.[1−4] RTILs typically have large, multiatom cations such as
ammonium, pyrrolidinium, imidazolium, triazolium, and tetra-
zolium ions that have diffuse positive charge distributions and
nonpolar alkyl functional groups (Figure 1). The diffuse nature
of the ionic charges, combined with the large effective
cation−anion distance in RTILs results in relatively low lattice
energies. By contrast, a typical ionic salt, NaCl (melting point
$T = 801$ °C), has very localized charge distributions on each
ion, and the separation between cation and anion is small;
therefore, a strong Coulombic attraction exists between sodium
and chloride ions in the condensed phase. As a result, the lattice
energy of NaCl is much higher than that for RTILs, and the
phase transition from ionic solid to liquid occurs at a much
higher temperature in NaCl than for RTILs.
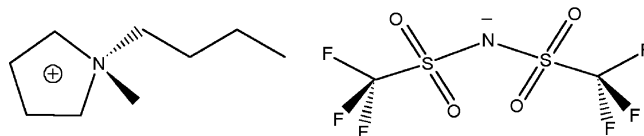
Figure 1. *N*-butyl-*N*-methylpyrrolidinium bistrifluorosulfonylimide
[pyrr$_{14}$]$^+$[NTf$_2$]$^-$, a room temperature ionic liquid.

Due to their ionic nature, RTILs were originally thought to
have essentially no vapor pressure. Recent studies of RTILs in
a vacuum have demonstrated that some RTILs can be distilled
in a vacuum with little thermal degradation,[5−8] as noted in more
detail below. Transpiration and Knudsen methods[9] have also
been applied to vaporize and recover RTIL condensates.[10−13]
To evaluate the thermal stability of a compound, studies such
as differential scanning calorimetry (DSC) and thermal gravi-
metric analysis (TGA) are typically carried out at atmospheric
pressure.[11,12,14−16] Recent TGA studies have shown that signifi-
cant mass loss of RTILs can occur at temperatures well below
the onset decomposition temperatures reported in DSC studies.[16]
Such loss in mass could represent depletion through vaporization
of intact RTILs.

The ionic nature of RTILs may lead to dramatically different
vaporization mechanisms than for molecular liquids. For protic
RTILs (having an H bound to a nitrogen in the cation ring),
typically a proton is transferred to the anion during vaporization
and neutral species are formed:[7]

* Corresponding author. E-mail: ghanshyam.vaghjiani@edwards.af.mil.
Address: AFRL/RZSP, 10 East Saturn Boulevard, Edwards AFB, CA 93524.
Fax: (661) 275-5471.
[†] ERC, Incorporated, Edwards Air Force Base.
[‡] Air Force Research Laboratory, Edwards Air Force Base.
[§] University of Pittsburgh.
[||] University of California, Berkeley.
[⊥] Current address: Institute of Chemistry, Hebrew University, Jerusalem
91904, Israel.

$$[AH]^+[B]^- \rightarrow A + BH \qquad (1)$$

These neutrals can be volatilized, and upon condensation, the RTIL can be reformed by proton exchange to the weaker acid (the reverse of reaction 1 above). The groundbreaking study by Earle et al.[5] demonstrated that when aprotic RTILs (having only alkyl groups bound to the cation ring nitrogens) are heated in a vacuum, recovery of the vapor produced the same RTIL with little or no degradation for several families of RTILs. Vaporization of mixtures of RTILs showed that one component was successfully enriched upon fractional distillation due to the differences in vapor pressure of one RTIL versus another.[7] The thermal stability of certain families of RTILs was attributed to the weak nucleophilicity (tendency to react with carbon) of the anion. Initially, the vaporization mechanism was proposed to be via cluster formation in the gas phase.[5] More recent studies using photoionization,[17] line of sight mass spectrometry,[18−20] Fourier transform ion cyclotron resonance,[6,7] and field desorption/ionization[21] mass spectrometric techniques suggest that vaporization of these thermally stable species is via neutral ion pair formation $[A^+B^-]$ in the gas phase, or, in the case of dicationic ionic liquids, via dication−dianion $[A^{2+}(B^-)_2]$ formation.[20] However, aprotic RTILs with strongly nucleophilic anions can react when heated, and the recovery of pure RTILs by vacuum distillation may not be feasible.

Theoretical modeling of RTILs[22] has been of great interest in order to predict such important properties as heats of formation, heats of vaporization,[11,23] melting and boiling points, viscosity, and thermal decomposition mechanisms.[24] Dynamics calculations have indicated that vaporization to produce an intact ion pair is energetically favored over ion cluster formation (multiple cation−anion pairs), where larger clusters have higher heats of vaporization.[25] The ionic nature of these liquids has made predicting these properties difficult and very few experimental data exist to confirm theoretical heats of formation and heats of vaporization values, quantities that are essential for evaluating RTIL performance as propellants.

The implication that RTILs evaporate as intact ion pairs is based on detection of the intact cation by mass spectrometry using photoionization or electron-impact ionization, as well as photoelectron spectroscopy and calculation. It is accepted that photoionization or electron impact ionization of the neutral ion pair, followed by dissociation, leads to a cation and a neutral, and the cation is then detected by the mass spectrometer:

$$[A^+B^-] + h\nu \rightarrow [A^+B] + e^- \rightarrow A^+ + B + e^- \qquad (2)$$
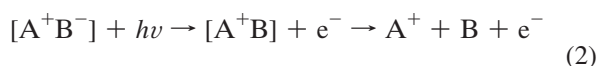
Direct detection of the ion pair has been elusive, most likely because of the use of relatively high energies of the ionizing photons (23.2 eV) or electrons (10−100 eV) versus the energy required to dissociate the ion pair:

$$[BMIM]^+[dca]^- \rightarrow BMIM^+ + dca^-$$
$$\Delta H = 3.59 \text{ eV at } 298 \text{ K (G3MP2)}^{10} \qquad (3)$$
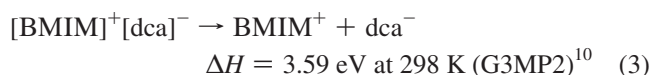
where $[BMIM]^+[dca]^-$ is the RTIL 1-butyl-3-methylimidazolium dicyanamide. However, recent progress has been made toward direct detection of ion pairs.[21]

In this study, a first report is provided for determinations of the heats of vaporization of room temperature ionic liquids by tunable synchrotron photoionization detection. Several ionic
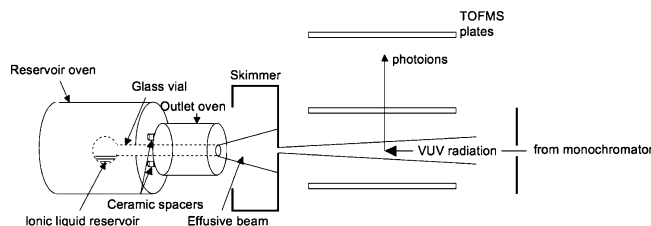

Figure 2. Ionic liquid effusive beam source.

liquids, *N*-butyl-*N*-methylpyrrolidinium bistrifluorosulfonylimide, $[pyrr_{14}]^+[NTf_2]^-$, *N*-butyl-*N*-methylpyrrolidinium dicyanamide, $[pyrr_{14}]^+[dca]^-$, and 1-butyl-3-methylimidazolium dicyanamide, $[BMIM]^+[dca]^-$, are studied by means of an effusive vapor source coupled to a vacuum ultraviolet photoionization time-of-flight mass spectrometer (PI-TOFMS). An analysis of the strengths of the photoionization method is made, which include the ability to study the heats of vaporization of the ionic liquid molecules at the tunable thresholds for dissociative photoionization, good comparisons between the ΔH_{vap} results from several fragment masses, and an ability to assess the temperature dependence of the photoionization cross sections. Furthermore, the comparison of experimental photoion appearance energies with theory supports a dissociative photoionization mechanism. To our knowledge, this study is the first reported measurement of the heat of vaporization of $[pyrr_{14}]^+[NTf_2]^-$. The heats of vaporization of $[BMIM]^+[dca]^-$ and $[pyrr_{14}]^+[dca]^-$ obtained here are in reasonable agreement with previously reported experimental measurements.

Experimental Section

The experiments are performed on the Chemical Dynamics Beamline, a tunable VUV beamline 9.0.2.3 at the Advanced Light Source in Berkeley, California. Product masses are detected as a function of the vaporization temperature of the ionic liquid and tunable photoionization wavelength. The PI-TOFMS repeller is pulsed at 10 kHz, and typically, data are accumulated for 200 000 pulses per mass spectrum. For $[pyrr_{14}]^+[dca]^-$, 200 000 pulses are accumulated at 12.0 eV photon energy at 473, 483, and 493 K. For $[pyrr_{14}]^+[NTf_2]^-$ and $[BMIM]^+[dca]^-$, photoionization efficiency (PIE) data were acquired as the VUV photon energy is scanned from 8.0 to 15.0 eV in 0.2 eV steps (photon energy resolution was 0.025 eV). The effusive beam is oriented counter propagating to the VUV beam. In this first study, PIE data are taken over a limited temperature range, at 468 and 483 K for $[BMIM]^+[dca]^-$ and at 583 and 613 K for $[pyrr_{14}]^+[NTf_2]^-$. In addition, data for $[pyrr_{14}]^+[NTf_2]^-$ are also accumulated at 12.6 and 15.0 eV for longer signal averaging of 9 million pulses per spectrum at both 583 and 613 K.

The RTIL source is a modified version of a source described previously.[17] Briefly, the source uses a Pyrex reservoir that has a narrow outlet tube (Figure 2). Each region is surrounded by a machined aluminum block. Each block is heated separately by four cartridge heaters embedded evenly around the cell axis. The heaters in each region are controlled by separate power supplies (0−40 W per region), and thermal equilibrium within the source is reached before PIE curves are measured. The temperatures in each region are measured using previously calibrated type K thermocouples, and from the uniformity of the heated regions and thermocouple readings, the temperature values reported here are assessed to have an error of ±3 K. Although the temperatures of the reservoir and outlet regions can be controlled separately, for heat of vaporization determina-

APPENDIX

Heats of Vaporization of RTILs

J. Phys. Chem. B, Vol. 114, No. 3, 2010 **1363**
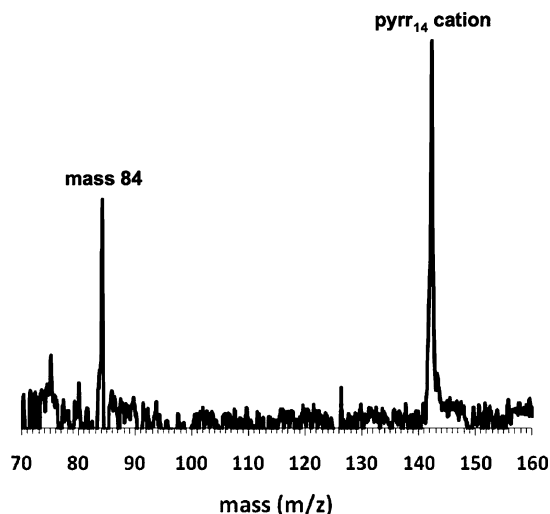
Figure 3. Mass spectrum of $[pyrr_{14}]^+[NTf_2]^-$ at 15.0 eV photon energy and a source temperature of 613 K.

Figure 4. Photoionization efficiency (PIE) curves of $[pyrr_{14}]^+[NTf_2]^-$ for mass 142 at 583 and 613 K and mass 84 at 613 K.

tions, the temperature of the reservoir region is set to be equal to the outlet region. In order to examine pyrolysis of ion pairs in the gas phase, the temperature of the outlet region can be set at a higher temperature than the reservoir region, and pyrolysis experiments will be described in a future publication. The experimental temperatures are selected by performing differential scanning calorimetry (DSC) on the ionic liquids prior to the photoionization experiments. The temperatures are selected to be well below the decomposition temperatures of the ionic liquids to avoid pyrolysis.

The raw mass spectra are corrected for fluctuations in the power of the light source by monitoring the power at a VUV photodiode whose wavelength response curve had previously been characterized. The synchrotron is operated in constant top off mode, and the ring current is kept constant at 500 mA. Low source temperature spectra are scaled and subtracted from the high temperature data to remove any background signals not due to the RTIL. Figure 3 shows a typical corrected mass spectrum. PIE curves are determined by integrating the peak areas of a given mass in each photon energy mass spectrum. Appearance energies were determined by a linear regression of the first five points above the signal-to-noise ratio, with an estimated uncertainty of ±0.2 eV.

1-Butyl-3-methylimidazolium dicyanamide (>98%) and *N*-butyl-*N*-methylpyrrolidinium dicyanamide (>99%) are obtained from EMD Chemicals/Merck. *N*-Butyl-*N*-methylpyrrolidinium bistrifluorosulfonylimide (>98%) is purchased from Aldrich. In order to remove volatile impurities present in the sample, the RTIL samples are heated in high vacuum (base pressure ~10^{-6} Pa) for 12 h prior to the experiments as follows: $[pyrr_{14}]^+[NTf_2]^-$ at 453K, $[pyrr_{14}]^+[dca]^-$ at 378 K, and $[BMIM]^+[dca]^-$ at 358 K.

Ab initio calculations are performed using Gaussian 03 W[26] at the HF/6-31+G(d,p) or B3LYP/6-31+G(d,p) level of theory to preoptimize geometries. Final optimization and energy calculations are performed at the MP2/6-31+G(d,p) and M06/[27] 6-31+G(d,p) levels of theory using GAMESS.[28,29] Resulting MP2 and M06 energies at 0 K are corrected for unscaled zero-point vibrational energies. On the basis of previous calculations of RTIL ionization processes using HF/6-31+G(d,p), B3LYP/6-31+G(d,p), and MP2/6-31+G(d,p) levels of theory, MP2/6-31+G(d,p) is selected as the preferred method due to good agreement with experimental ionization potentials and ionization trends. The MP2/6-31+G(d,p) level
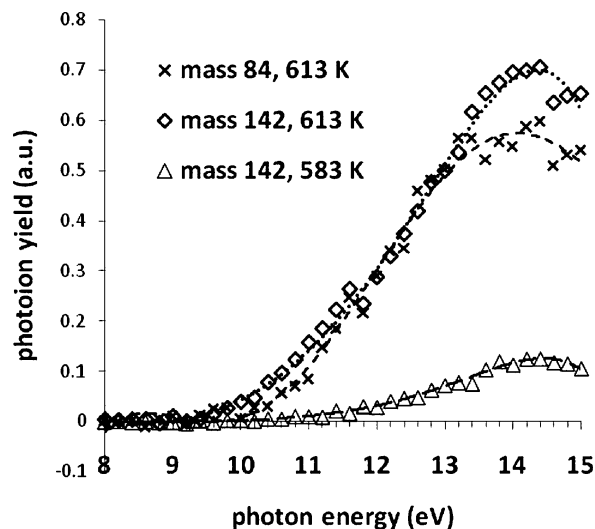
of theory is assigned an uncertainty of ±0.1 eV based on our previous calculations. Due to complications with MP2 for $[pyrr_{14}]^+[dca]^-$ explained below, M06 was used to calculate the ionization energies for $[pyrr_{14}]^+[dca]^-$.

Results and Discussion

As noted, a mass spectrum of $[pyrr_{14}]^+[NTf_2]^-$ taken at 613 K and 15.0 eV photon energy is shown in Figure 3, and the PIE curves for mass 142 at 583 and 613 K and mass 84 at 613 K are shown in Figure 4. Mass 142 represents the $[pyrr_{14}]^+$ parent cation of the ionic liquid ion pair in the gas phase (eq 2). The appearance of mass 84 is due to fragmentation of the internally hot $[pyrr_{14}]^+$ cation, which can be attributed to C_4H_{10} loss. From these curves, the appearance energies of the resulting intact cation and fragment cations can be determined, allowing insight into the energetics of ionization of the ion pair and possible ion fragmentation pathways. The observed appearance energies for masses 142 and 84 are 9.4 ± 0.2 and 10.0 ± 0.2 eV, respectively, which are in excellent agreement with their corresponding MP2 appearance energies of 9.2 ± 0.1 and 10.1 ± 0.1 eV. The thermal contribution due to the small temperature differences in these experiments (≤30 K) should only amount to a few millielectron volts at the temperatures involved, causing a shift to lower appearance energy due to hot bands that is smaller than the resolution of our experiment.

By comparing the intensities of mass 142 peaks, which are proportional to the number densities of the ion pair in the RTIL vapor,[18] at two known source temperatures T_1 and T_2 and applying the Clausius−Clapeyron equation, the heat of vaporization in this temperature range is directly determined:

$$\Delta H_{vap} = -R \ln(I_2/I_1)[(T_1 T_2)/(T_2 - T_1)] \qquad (4)$$

where I is the measured mass 142 peak intensity and R is the gas constant. Over the temperature range of this experiment, the photoionization cross section at a given photon energy is considered to be constant. The branching fractions from the ionized ion pair to intact cation or cation fragments are considered to be constant as well.

The heat of vaporization of $[pyrr_{14}]^+[NTf_2]^-$ is determined using eq 4 and the data in the following ways: (1) using the sum of the intensities of all the points along the mass 142 tunable

APPENDIX

TABLE 1: Heats of Vaporization Data[a]

$[pyrr_{14}]^+[NTf_2]^-$	ΔH_{vap}(PIE)	ΔH_{vap}(12.6 eV)	ΔH_{vap}(15.0 eV)	ΔH_{vap}(average)	
mass 142	180.3	156.6	174.6	170.5	
mass 84	167.9	155.3	165.4	162.9	
			average of six values =	166.7	
			correction to 298.15 K =	28.2	
			ΔH_{vap}(298.15) =	**195 ± 19**	
$[pyrr_{14}]^+[dca]^-$	ΔH_{vap}(483/473 K)	ΔH_{vap}(493/483 K)	ΔH_{vap}(493/473 K)	ΔH_{vap}(average)	ΔH_{vap}(slope)
mass 84, 12.0 eV	145.2	157.1	151.1	151.1	151.0
			correction to 298.15 K =	19.5	
			ΔH_{vap}(298.15) =	**171 ± 12**	
$[BMIM]^+[dca]^-$	ΔH_{vap}(mass 82)	ΔH_{vap}(mass 97)	ΔH_{vap}(mass 124)	ΔH_{vap}(mass 137)	ΔH_{vap}(average)
PIE 483/468 K	148.4	157.4	162.4	154.8	155.8
				correction to 298.15 K =	18.7
				ΔH_{vap}(298.15) =	**174 ± 12**

[a] All values are in kJ/mol. Uncertainties in the present work are twice the standard deviation.

TABLE 2: Experimental and Literature Values for Heats of Vaporization and Temperatures of Decomposition

RTIL	T (K) range	this work ΔH_{vap} (kJ mol^{-1}) (average)	$\Delta C_p \Delta T$ (kJ mol^{-1})	this work ΔH_{vap} (kJ mol^{-1}) (298.15 K)	literature ΔH_{vap} (kJ mol^{-1}) (298.15 K)	$T_{decomposition}$ (K)
$[BMIM]^+[dca]^-$	468−483	156 ± 12	18.7	174 ± 12	157.2 ± 1.1[a]	513[b]
$[pyrr_{14}]^+[dca]^-$	473−493	151 ± 18	19.5	171 ± 12	161.0 ± 2.0[c]	535[d]
$[pyrr_{14}]^+[NTf_2]^-$	583−613	167 ± 19	28.2	195 ± 19		672[d]

[a] Reference 10. [b] Reference 31. [c] Reference 18. [d] References 16 and 31.

wavelength PIE curve (36 points with 7.2 million pulses total per curve) at T_1 and T_2, (2) by individually comparing the intensities at T_1 and T_2 of mass 142 at one specific wavelength, 12.6 eV, and (3) by analyzing the results also at 15.0 eV. A longer signal averaging condition of 9 million pulses is used for the last two cases. T_1 and T_2 are 583 and 613 K, respectively. A similar analysis is performed for mass 84 also. Table 1 summarizes the experimental ΔH_{vap} values obtained. The experimental ΔH_{vap} values have been corrected to 298.15 K using a ΔC_p value of -105.4 J·K^{-1}·mol^{-1} for $[BMIM]^+[dca]^-$ and $[pyrr_{14}]^+[dca]^-$ [18] and a value of -94 J·K^{-1}·mol^{-1} for $[pyrr_{14}]^+[NTf_2]^-$.[10]

$$\Delta H_{vap}(298.15 \text{ K}) = \Delta H_{vap}(T) + \Delta C_p \Delta T \qquad (5)$$

Uncertainties in the ΔC_p values were not reported in ref 10, but their influence on the temperature corrected ΔH_{vap} values was estimated to be negligible within experimental uncertainties, and therefore they are not included here. The uncertainties in Table 1 represent twice the standard deviation of the measurements. The larger uncertainties in these measurements are the result of having fewer data points across similar temperature ranges for determining the heat of vaporization versus the more extensive maps versus temperature in the referenced works.
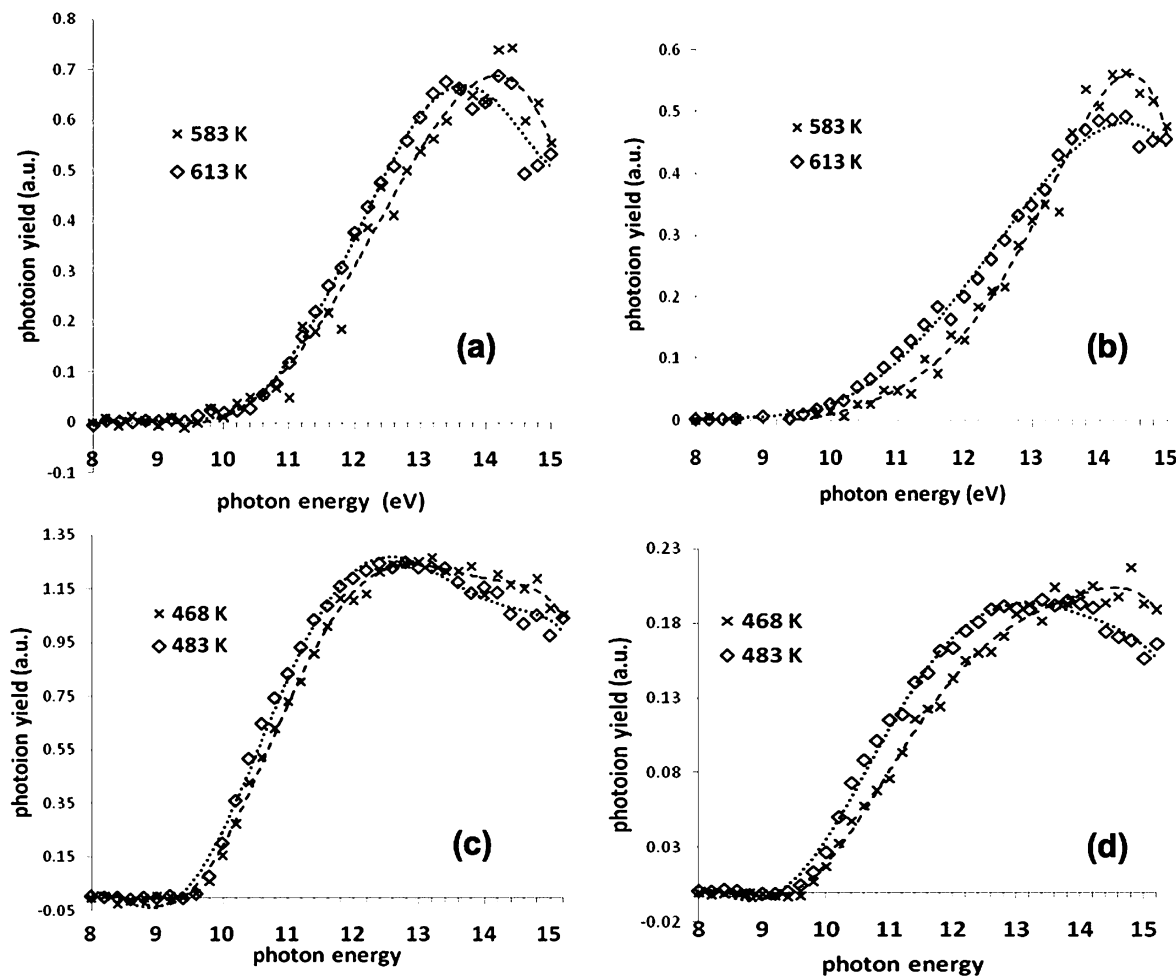
Good agreement for ΔH_{vap} calculated using masses 142 and 84 (170.5 vs 162.9 kJ/mol, Table 1) indicates the possibility of calculating ΔH_{vap} from mass fragments of the cation, and mass 84 is used successfully to determine the ΔH_{vap} of $[pyrr_{14}]^+[dca]^-$. One possibility why mass 84 is usable for determining the heat of vaporization for the $[pyrr_{14}]^+$-containing RTILs may be due to its increased stability from possible resonance structures of the cation.[18] This stability also could explain the significant fragmentation of the intact cation to mass 84 under such soft ionization conditions. An additional Clausius−Clapeyron calculation was performed by plotting ln I versus $1/T$ of mass 84 at three temperatures, namely, 473, 483, and 493 K. The heat

of vaporization determined by the slope of the straight line through these points agrees well with the average value (ΔH_{vap}(slope) vs ΔH_{vap}(average), Table 1). Mass 84 analysis for the heat of vaporization of $[pyrr_{14}]^+[dca]^-$ agrees reasonably well with the reported literature value (Table 2). For $[BMIM]^+[dca]^-$, masses 82, 97, 124, and 137 are used to calculate the heat of vaporization, and the reported heat of vaporization value is slightly higher than the literature value (Table 1). The successful determination of ΔH_{vap} from fragment masses is important because for some RTILs the intact cation may not be detected. In fact, only a very weak parent cation ion peak at mass 142 is detected for $[pyrr_{14}]^+[dca]^-$ and no parent peak at mass 139 is detected for $[BMIM]^+[dca]^-$. The present ΔH_{vap} of $[pyrr_{14}]^+[NTf_2]^-$ is consistent with heats of vaporization determined for other NTf_2^- based RTILs.[6,12,13,23,25,30] The temperatures used in these experiments are well below the reported onset decomposition temperatures (nonzero DSC slope) for these species (Table 2).

To assess the temperature dependence of the photoionization cross section, the relative shapes of the PIE curves obtained at the experimental reservoir temperatures are compared. Figure 5a shows the comparison of the $[pyrr_{14}]^+[NTf_2]^-$ mass 142 PIE curves at 583 and 613 K. In order to try to force the curve shapes to match, rather than simply scaling the PIE curve at 583 K to the PIE curve at 613 K so that the highest points match, the PIE curve at 583 K is scaled iteratively to fit to the 613 K data by a least-squares fit where the sum of the squares of the difference between two points at a fixed photon energy is minimized:

$$(d/dS)\Sigma(SI_{583} - I_{613})^2 = 0 \qquad (6)$$

By this method, if the scaled PIE curves are identical, then $\Sigma(SI_{583} - I_{613})^2$ would necessarily equal zero, and $S = (I_{613}/I_{583})$. However, if the curves do not match exactly, then $\Sigma(SI_{583} - I_{613})^2 > 0$. In Figure 5a and b, for $[pyrr_{14}]^+[NTf_2]^-$, the high

APPENDIX

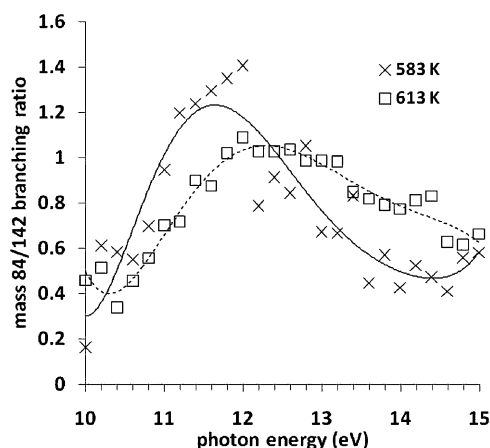Heats of Vaporization of RTILs

J. Phys. Chem. B, Vol. 114, No. 3, 2010 **1365**

Figure 5. Least-squares fit analyses of the PIE curves for (a) $[pyrr_{14}]^+[NTf_2]^-$ of mass 142 at 583 K relative to 613 K, (b) $[pyrr_{14}]^+[NTf_2]^-$ of mass 84 at 583 K relative to 613 K, (c) $[BMIM]^+[dca]^-$ of mass 97 at 468 K relative to 483 K, and (d) $[BMIM]^+[dca]^-$ of mass 137 at 468 K relative to 483 K.

temperature PIE curves for both mass 142 and mass 84 appear to have shifted slightly to higher intensities between 10 and 13.6 eV ($SI_{583} < I_{613}$) and to lower intensities above 13.6 eV ($SI_{583} > I_{613}$) relative to the low temperature PIE curves. Due to this slight shift in the PIE shape at higher temperature, in the region where the PIE intensity increases with temperature, $SI_{583} < I_{613}$ (10−13.6 eV), the Clausius−Clapeyron approach systematically overestimates the heat of vaporization. In the region where the PIE intensity decreases with temperature above 13.6 eV where $SI_{583} > I_{613}$, the Clausius−Clapeyron calculation will underestimate the heat of vaporization. Because there are more points in the PIE summed calculation where $SI_{583} < I_{613}$ (8−13.6 eV, 29 points) than where $SI_{583} > I_{613}$ (13.8−15 eV, 7 points), the PIE summed result from the Clausius−Clapeyron calculation will systematically overestimate the actual heat of vaporization, although these effects will tend to cancel somewhat. If, instead of determining the heat of vaporization of $[pyrr_{14}]^+[NTf_2]^-$ using the ratio of summed PIE intensities ($I_{613}/I_{583} = 6.17$, $\Delta H_{vap} = 180.3$ kJ/mol, Table 1) of mass 142 in the Clausius−Clapeyron equation one uses the curve fitting scaling factor $S = 5.29$ from Figure 5a, the result is $\Delta H_{vap} = 165.0$ kJ/mol, a reduction in the calculated value of ΔH_{vap} by 8.9%. A similar treatment for mass 84 (Figure 5b) and for masses 97 and 137 of $[BMIM]^+[dca]^-$ in Figure 5c and d results in overestimates of 1.1, 6.3, and 1.1%, respectively. The similar shifts in the PIE curves in Figure 5 indicate this is a systematic phenomenon. On the basis of ΔH_{vap} calculated from the measured PIE curve

sum values and comparison with the scaling factor analysis which takes into account the slight temperature shift in PIE curves, the ΔH_{vap} values determined by PIE summed data likely contain a systematic overestimation of 1−10%, depending on how much the PIE curve shifts at the higher temperature. Although the ΔH_{vap} values determined by PIE were included in the reported average value for $[pyrr_{14}]^+[NTf_2]^-$ in Table 1, the uncertainty (±19 kJ/mol, twice the standard deviation) is 9.7% of this value and encompasses this systematic error. An improvement in the accuracy of this method will be to select a photon energy where the scaled PIE curves cross at $S = I_2/I_1$ and competition between photoionization cross section and ion fragmentation cancels each other out. For example, monitoring the vapor density as a function of temperature at ∼13.6 eV and determining ΔH_{vap} from the slope of a plot of ln I versus $1/T$[18] would increase both the accuracy and precision of this method.

The PIE curve shift at higher temperature could be due to several factors. Competition between increased photoionization cross section and increased ion fragmentation at high temperatures may account for this observed shift. Below 13.6 eV, a larger photoionization cross section at high temperatures could explain the shift to higher intensities, and above 13.6 eV, increased ion fragmentation reduces the PIE intensity. A direct comparison of the branching ratios of masses 84/142 at two different temperatures is shown in Figure 6. Above ∼12 eV, the increase in branching ratio at higher temperature indicates increased ion fragmentation with increasing temperature.
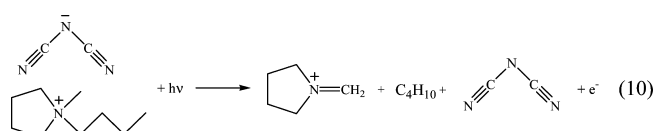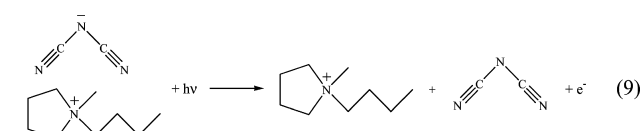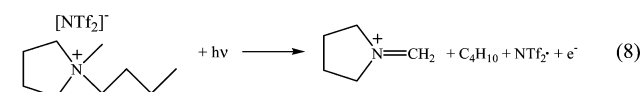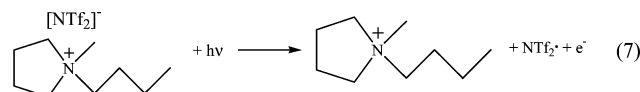
APPENDIX

1366   *J. Phys. Chem. B, Vol. 114, No. 3, 2010*   Chambreau et al.

Figure 6. Mass 84/142 branching ratios for $[pyrr_{14}]^+[NTf_2]^-$ at 583 and 613 K as a function of photon energy.

mentally determined photoion appearance energies. The measured mass 142 appearance energy in Figure 4 (9.4 ± 0.2 eV) agrees well with the *ab initio* value of 9.2 ± 0.1 eV calculated at the MP2/6-31+G(d,p) level of theory (0 K, ZPVE corrected) for the $[pyrr_{14}]^+[NTf_2]^-$ ion pair (eq 7). An appearance energy of 10.1 ± 0.1 eV (experimental value = 10.0 ± 0.2 eV) was calculated for mass 84, assuming elimination of C_4H_{10} from the $pyrr_{14}^+$ cation to form the resonance stabilized cationic structure postulated in a previous publication (eq 8).[18] The electron affinity for the NTf$_2$• radical is calculated to be 5.7 eV at the MP2/6-31+G(d,p) level of theory.

There are several advantages for using photoionization versus electron impact ionization for measuring heats of vaporization for RTILs. The narrow energy spread of the light source (0.025 eV) and soft ionization conditions minimize the effect of fragmentation of the parent cation and allow for appearance energies to be determined accurately. Typical electron impact ionization energies are around 70 eV, where the electron impact ionization cross section curve is large and the shape of the curve is flat for many atomic and molecular species, but molecular fragmentation to smaller species can be extensive. In this work, photoionization measurements yield a branching ratio of masses 84/142 of nearly 1 for $[pyrr_{14}]^+[NTf_2]^-$, indicating the small extent of fragmentation of the $[pyrr]^+$ under the present soft ionization conditions versus electron impact ionization of $[pyrr_{14}]^+[dca]^-$ with a branching ratio of masses 84/142 that is about an order of magnitude higher.[18] Although fragmentation of the parent ion can be minimized by lowering the electron impact energy, the electron impact ionization cross section changes rapidly as a function of electron energy near the ionization threshold,[31,32] and may be highly susceptible to thermal effects near the ionization threshold. Also, the energy spread of a typical electron gun is limited to >0.5 eV, limiting the energy resolution in threshold measurements. Therefore, determining appearance energies of ions by electron impact ionization is difficult and has large associated uncertainties.

From the accurate determination of photoion appearance energies by the present method, comparison with theoretical energy calculations can be made. *Ab initio* calculations of the energetics involved in the dissociative photoionization processes (described below) are in excellent agreement with the experi-

Calculation of the adiabatic ionization potentials of dicyanamide and $[pyrr_{14}]^+[dca]^-$ at the MP2 level was precluded due to the inadequacy of a single configuration reference wave function for the neutral dicyanamine species. (The need for a multiconfigurational reference in dicyanamine is evident from (a) the high degree of spin contamination present in the unrestricted Hartree−Fock (UHF) wave function ($\langle S^2 \rangle = 1.303$, compared to 0.5 for a pure spin doublet) and (b) the presence of multiple unphysical natural orbital occupation numbers (see Gordon, M. S.; Schmidt, M. W.; Chaban, G. M.; Glaesemann, K. R.; Stevens, W. J.; Gonzalez, C. *J. Chem. Phys.* **1999**, *110*, 4199) obtained from the second-order Z-averaged perturbation theory (ZAPT(2)) relaxed density matrix.) However, the electron affinity for the dicyanamide radical has been determined experimentally to be 4.135 eV.[33] Using this value along with the theoretical values in Table 3, the appearance energy for mass 84 in eq 10 is estimated to be 8.73 ± 0.1 eV, and is in excellent

TABLE 3: *Ab initio* **Energies (in Hartrees) of Proposed Species Involved in Dissociative Photoionization of $[pyrr_{14}]^+[NTf_2]^-$ and $[pyrr_{14}]^+[dca]^-$**

species	E_0	zero point energy	total H_0
$[pyrr_{14}]^+[NTf_2]^-$ ion pair	−2232.073761	0.348228	−2231.725533
$[pyrr_{14}]^+[NTf_2•]$ ion pair cation	−2231.758743	0.346514	−2231.412229
$[pyrr_{14}]^+$ cation	−408.215636	0.293093	−407.922543
$[NTf_2]^-$ anion	−1823.729958	0.053730	−1823.676228
NTf$_2$• neutral radical	−1823.518844	0.052807	−1823.466037
$[pyrr_{14}]^+[dca]^-$ ion pair	−648.205863	0.314189	−647.891674
$[pyrr_{14}]^+[dca•]$ ion pair cation (MP2 vertical)	−647.924455	0.314189	−647.610266
$[pyrr_{14}]^+[dca]^-$ ion pair (M06)	−649.732310	0.306353	−649.425957
$[pyrr_{14}]^+[dca•]$ ion pair cation (M06 vertical)	−649.444280	0.306353	−649.137927
$[pyrr_{14}]^+[dca•]$ ion pair cation (M06 adiabatic)	−649.448255	0.034323	−649.143932
$[dca]^-$ anion	−239.854100	0.020016	−239.834084
mass 84 cation	−250.263014	0.151086	−250.111928
butane	−157.912441	0.135673	−157.776768

Appendix

Heats of Vaporization of RTILs

J. Phys. Chem. B, Vol. 114, No. 3, 2010 **1367**

agreement with the experimental appearance energy for mass 84 in the $[pyrr_{14}]^+[dca]^-$ dissociative photoionization of 8.8 ± 0.2 eV. The estimated appearance energy of the intact $[pyrr_{14}]^+$ cation in eq 9 is 7.81 eV. However, the experimental signal-to-noise ratio for this species was not sufficient to determine its appearance energy, although it was detectable at higher energies. From M06 calculations, the vertical and adiabatic ionization potentials of $[pyrr_{14}]^+[dca]^-$ are 7.8 and 7.7 eV, respectively, and the M06 vertical ionization potential agrees well with the MP2 vertical ionization potential of 7.7 eV. Overall, the agreement between theory and experiment supports the dissociative photoionization of isolated cation−anion pairs in the gas phase.

Conclusions

Heats of vaporization for several room temperature ionic liquids have been determined by effusive beam VUV photoionization mass spectrometry. The photoionization cross section is considered to be temperature independent when using the PIE curves for the Clausius−Clapeyron analysis. We estimate a positive systematic error of up to 10% for this assumption. After thermal correction to 298.15 K, the ΔH_{vap} values of $[BMIM]^+[dca]^-$ and $[pyrr_{14}]^+[dca]^-$ reported here are in reasonable agreement with the previously reported experimental values. For $[pyrr_{14}]^+[NTf_2]^-$, $\Delta H_{vap}(298.15$ K$)$ is calculated to be 195 $\pm$ 19 kJ mol^{-1}, which has not been reported previously. Detection of the intact $[pyrr_{14}]^+$ cation is indicative of the presence of neutral cation−anion pairs in the effusive beam which dissociate to form $[pyrr_{14}]^+$ and neutral $NTf_2\bullet$ at low VUV photon energy. A second dissociation pathway detected is the efficient fragmentation of $[pyrr_{14}]^+$ to produce mass 84. Together, these experimental heats of vaporization, photoionization appearance energies, and *ab initio* calculations support a vaporization mechanism for RTILs as intact cation−anion pairs.

References and Notes

(1) Chambreau, S. D.; Schneider, S.; Rosander, M.; Hawkins, T.; Gallegos, C. J.; Pastewait, M. F.; Vaghjiani, G. L. *J. Phys. Chem. A* **2008**, *112*, 7816.

(2) Gao, H.; Joo, Y.-H.; Twamley, B.; Zhou, Z.; Shreeve, J. n. M. *Angew. Chem., Int. Ed.* **2009**, *48*, 2792.

(3) Hawkins, T.; Rosander, M.; Vaghjiani, G. L.; Chambreau, S. D.; Drake, G.; Schneider, S. *Energy Fuels* **2008**, *22*, 2871.

(4) Schneider, S.; Hawkins, T.; Rosander, M.; Mills, J. D.; Vaghjiani, G. L.; Chambreau, S. D. *Z. Inorg. Chem.* **2008**, *47*, 6082.

(5) Earle, M. J.; Esperança, J. M. S. S.; Gilea, M. A.; Canongia Lopes, J. N.; Rebelo, L. P. N.; Magee, J. W.; Seddon, K. R.; Widegren, J. A. *Nature* **2006**, *439*, 831.

(6) Leal, J. P.; Minas da Piedade, M. E.; Canongia Lopes, J. N.; Tomaszowska, A. A.; Esperança, J. M. S. S.; Rebelo, L. P. N.; Seddon, K. R. *J. Phys. Chem. B* **2009**, *113*, 3491.

(7) Leal, J. P.; Esperança, J. M. S. S.; Minas da Piedade, M. E.; Canongia Lopes, J. N.; Rebelo, L. P. N.; Seddon, K. R. *J. Phys. Chem. A* **2007**, *111*, 6176.

(8) Rebelo, L. P. N.; Canongia Lopes, J. N.; Esperança, J. M. S. S.; Filipe, E. *J. Phys. Chem. B* **2005**, *109*, 6040.

(9) Zaitsau, D. H.; Verevkin, S. P.; Paulechka, Y. U.; Kabo, G. J.; Sevruk, V. M. *J. Chem. Eng. Data* **2003**, *48*, 1393.

(10) Emel'yanenko, V. N.; Verevkin, S. P.; Heintz, A. *J. Am. Chem. Soc.* **2007**, *129*, 3930.

(11) Paulechka, Y. U.; Kabo, G. J.; Blokhin, A. V.; Vydrov, O. A.; Magee, J. W.; Frenkel, M. *J. Chem. Eng. Data* **2003**, *48*, 457.

(12) Paulechka, Y. U.; Zaitsau, D. H.; Kabo, G. J.; Strechan, A. A. *Thermochim. Acta* **2005**, *439*, 158.

(13) Zaitsau, D. H.; Kabo, G. J.; Strechan, A. A.; Paulechka, Y. U.; Tscherisch, A.; Verevkin, S. P.; Heintz, A. *J. Phys. Chem. A* **2006**, *110*, 7303.

(14) Dzyuba, S. V.; Bartsch, R. A. *ChemPhysChem* **2002**, *3*, 161.

(15) Ngo, H. L.; LeCompte, K.; Hargens, L.; McEwen, A. B. *Thermochim. Acta* **2000**, *357−358*, 97.

(16) Wooster, T. J.; Johanson, K. M.; Fraser, K. J.; MacFarlane, D. R.; Scott, J. L. *Green Chem.* **2006**, *8*, 691.

(17) Strasser, D.; Goulay, F.; Kelkar, M. S.; Maginn, E. J.; Leone, S. R. *J. Phys. Chem. A* **2007**, *111*, 3191.

(18) Emel'yanenko, V. N.; Verevkin, S. P.; Heintz, A.; Corfield, J.-A.; deyko, A.; Lovelock, K. R. J.; Licence, P.; Jones, R. G. *J. Phys. Chem. B* **2008**, *112*, 11734.

(19) Armstrong, J. P.; Hurst, C.; Jones, R. G.; Licence, P.; Lovelock, K. R. J.; Satterly, C. J.; Villar-Garcia, I. *J. Phys. Chem. Chem. Phys.* **2007**, *9*, 982.

(20) Lovelock, K. R. J.; Deyko, A.; Corfield, J.-A.; Gooden, P. N.; Licence, P.; Jones, R. G. *ChemPhysChem* **2009**, *10*, 337.

(21) Gross, J. H. *J. Am. Soc. Mass Spectrom.* **2008**, *19*, 1347.

(22) de Andrade, J.; Böes, E. S.; Stassen, H. *J. Phys. Chem. B* **2002**, *106*, 13344.

(23) Köddermann, T.; Paschek, D.; Ludwig, R. *ChemPhysChem* **2008**, *9*, 549.

(24) Kroon, M. C.; Buijs, W.; Peters, C. J.; Witkamp, G.-J. *Thermochim. Acta* **2007**, *465*, 40.

(25) Kelkar, M. S.; Maginn, E. J. *J. Phys. Chem. B* **2007**, *111*, 9424.

(26) Frisch, M. J.; Trucks, G. W.; Schlegel, H. B.; Scuseria, G. E.; Robb, M. A.; Cheeseman, J. R.; Montgomery, J. A., Jr.; Vreven, T.; Kudin, K. N.; Burant, J. C.; Millam, J. M.; Iyengar, S. S.; Tomasi, J.; Barone, V.; Mennucci, B.; Cossi, M.; Scalmani, G.; Rega, N.; Petersson, G. A.; Nakatsuji, H.; Hada, M.; Ehara, M.; Toyota, K.; Fukuda, R.; Hasegawa, J.; Ishida, M.; Nakajima, T.; Honda, Y.; Kitao, O.; Nakai, H.; Klene, M.; Li, X.; Knox, J. E.; Hratchian, H. P.; Cross, J. B.; Bakken, V.; Adamo, C.; Jaramillo, J.; Gomperts, R.; Stratmann, R. E.; Yazyev, O.; Austin, A. J.; Cammi, R.; Pomelli, C.; Ochterski, J. W.; Ayala, P. Y.; Morokuma, K.; Voth, G. A.; Salvador, P.; Dannenberg, J. J.; Zakrzewski, V. G.; Dapprich, S.; Daniels, A. D.; Strain, M. C.; Farkas, O.; Malick, D. K.; Rabuck, A. D.; Raghavachari, K.; Foresman, J. B.; Ortiz, J. V.; Cui, Q.; Baboul, A. G.; Clifford, S.; Cioslowski, J.; Stefanov, B.; Liu, G.; Liashenko, A.; Piskorz, P.; Komaromi, I.; Martin, R. L.; Fox, D. J.; Keith, T.; Al-Laham, M. A.; Peng, C. Y.; Nanayakkara, A.; Challacombe, M.; Gill, P. M. W.; Johnson, B.; Chen, W.; Wong, M. W.; Gonzalez, C.; Pople, J. A. *Gaussian 03*; revision C.02; Gaussian, Inc.: Wallingford, CT, 2004.

(27) Zhao, Y.; Truhlar, D. G. *Theor. Chem. Acc.* **2008**, *120*, 215.

(28) Gordon, M. S.; Schmidt, M. W. Advances in electronic structure theory: GAMESS a decade later. In *Theory and Applications of Computational Chemistry: the first forty years*; Dykstra, C. E., Frenking, G., Kim, K. S., Scuseria, G. E., Eds.;Elsevier: Amsterdam, The Netherlands, 2005; p 1167.

(29) Schmidt, M. W.; Baldridge, K. K.; Boatz, J. A.; Elbert, S. T.; Gordon, M. S.; Jensen, J. H.; Koseki, S.; Matsunaga, N.; Nguyen, K. A.; Su, S.; Windus, T. L.; Dupuis, M.; Montgomery, J. A. *J. Comput. Chem.* **1993**, *14*, 1347.

(30) Swiderski, K.; McLean, A.; Gordon, C. M.; Vaughn, D. H. *Chem. Commun.* **2004**, 2178.

(31) Kim, Y.-K.; Hwang, W.; Weinberger, N. M.; Ali, M. A.; Rudd, M. E. *J. Chem. Phys.* **1996**, *106*, 1026.

(32) Probst, M.; Deutsch, H.; Becker, K.; Märk, T. D. *Int. J. Mass. Spectrom.* **2001**, *206*, 13.

(33) Jagoda-Cwiklik, B.; Wang, X.-B.; Woo, H.-K.; Yang, J.; Wang, G.-J.; Zhou, M.; Jungwirth, P.; Wang, L.-S. *J. Phys. Chem. A* **2007**, *111*, 7719.

JP909423M

Appendix

This page intentionally left blank

Appendix

Thermochemistry of Species Potentially Formed During NTO/MMH Hypergolic Ignition

Antoine Osmont

ICARE-CNRS, 1C, Avenue de la Recherché Scientifique, 45071 Orleans Cedex 2 (France)

Laurent Catoire*

ICARE-CNRS, 1C, Avenue de la Recherché Scientifique, 45071 Orleans Cedex 2 and Department of Chemistry, University of Orleans, Orleans (France)

Thomas M. Klapötke

Department of Chemistry and Biochemistry, Ludwig-Maximilians University of Munich, Butenandtstr. 5-13 (Haus D), D-81377 Munich (Germany)

Ghanshyam L. Vaghjiani

Propellant Branch, Space and Missile Propulsion Division, Propulsion Directorate, Air Force Research Laboratory, AFRL/PRSP, 10 E. Saturn Boulevard, Edwards AFB, CA 93524 (USA)

Mark T. Swihart

Department of Chemical and Biological Engineering, 303 Furnas Hall, State University of New York at Buffalo, Buffalo, NY 14260-4200 (USA).

Abstract

This paper deals with the gas-phase thermodynamic properties of endothermic compounds potentially formed during monomethylhydrazine (MMH)/nitrogen tetroxide (NTO) hypergolic reactivity. The standard enthalpies of formation at 298.15 K are determined by means of quantum chemistry calculations along with protocols developed for these compounds. The resultant data, currently previously unavailable for almost all of these compounds, are potentially critical to the modeling of combustion chemistry of this bipropellant combination.

Keywords: Standard Enthalpies of Formation, Monomethylhydrazine, Nitrogen Tetroxide, Unsymmetrical Dimethyl Hydrazine

1 Introduction

Nitrogen tetroxide (NTO)/monomethylhydrazine (MMH), NTO/unsymmetrical dimethyl hydrazine (UDMH) and NTO/Aerozine 50 (MMH/UDMH mixture)

are chemical systems used for in-space liquid propulsion. These systems are very interesting because they are able to autoignite at low temperature (room temperature and below), i.e. they ignite without any external ignition device. This phenomenon is called hypergolicity. From a fundamental research point of view, much more work is needed to understand all the features of hypergolic ignition. Fuels are stored in the liquid state but, as usual for liquids, ignition (hypergolic or not) occurs in the gas-phase above the liquids. This has been recently shown for a hypergolic system by Alfano et al. [1]. Gas-phase species and condensed-phase species form during the reaction between NTO and MMH or UDMH. Experimental observations show that condensed species form when the reaction does not lead to ignition and that condensed species form when hypergolic ignition occurs, i.e. during the ignition delay [2]. The chemical nature of these compounds is not clearly established, despite numerous studies. In fact, the NTO/MMH chemistry depends on the experimental conditions: equivalence ratios, temperature, and pressure. Liquid-liquid reactions at low temperature lead to condensed methylhy-

* Corresponding author; e-mail: catoire@cnrs-orleans.fr

Appendix

A. Osmont, L. Catoire, T. M. Klapötke, G. L. Vaghjiani, M. T. Swihart

drazinium nitrate. It can also be the case that methylhydrazinium azide forms. However, even if these species can play a role in other related topics, such as hard starts, their role in hypergolic ignition is not completely clear. A detailed chemical kinetic model was proposed to interpret the gas-phase NTO/MMH reactivity [3]. This mechanism includes a sub-mechanism devoted to MMH thermal decomposition, validated with MMH profiles observed in shock tube experiments [4] and a sub-mechanism devoted to the oxidation of MMH validated with MMH/O$_2$ [5] and MMH/O$_2$/H$_2$ [6] ignition delays. The formation of methyldiazene CH$_3$N=NH and its subsequent thermal decomposition together with the exothermic formation of nitrite and nitro compounds resulting from termolecular recombinations between methylhydrazyl radicals and NO$_2$ explain gas-phase hypergolic ignition and gas-phase non-ignition. It remains uncertain whether this model is sufficiently detailed, but it allows the simulation of gas-phase MMH/NTO self-ignition at low temperature (ambient and below), for any pressure, and this is certainly a major achievement. It is commonly the case that only about 10% of the reactions given in a detailed chemical kinetic model play a role on the ignition/combustion process and therefore the writing of all the likely reactions is not always appropriate. Sun and Law [7] recently proposed rate constants for some elementary reactions needed to simulate the thermal decomposition of MMH. These reactions are not expected to play a role in MMH/NTO hypergolic ignition, but this remains to be demonstrated. Nonnenberg et al. [8], and Frank et al. [9] used molecular dynamics to simulate NTO/MMH reactivity and found that methyldiazene can be assumed to be the main product during NTO/MMH hypergolic ignition. According to this paper, the recombination of methylhydrazyl radicals can lead to dimethyltetrazanes. Indeed these termolecular recombination reactions are exothermic and must be considered in the NTO/MMH detailed chemical kinetic model. Thermodynamic data needed for the writing of MMH-based detailed kinetic models are presented in Ref. [10] and [11]. The thermochemistry presented by Sun and Law [7] for methylhydrazyl radicals CH$_3$N'NH$_2$, CH$_3$NHNH' and CH$_2$'NHNH$_2$ is consistent with the data presented by Catoire and Swihart [10]. However, the thermochemistry of the dimethyltetrazanes is not available and remains to be studied. McQuaid et al. [12, 13] also present considerations for MMH/IRFNA hypergolic ignition, which partially validate the NTO/MMH detailed chemical kinetic model proposed. Finally, the formation of a number of nitroso, nitrite, nitro, and nitrate compounds, not previously taken into account, must be considered for completeness. Nitroso, nitrite, nitro, and nitrate compounds considered here have an −NO group, −NO$_2$ group, −ONO group, or −ONO$_2$ group attached to nitrogen atom, respectively. Experimental data for such derivatives of MMH and UDMH are scarce. The thermochemistry of these compounds is needed to allow the construction of more detailed chemical kinetic models able to simulate hypergolic ignition. The aim of this work is to present gas-phase standard enthalpy of formation of nitroso, nitro, nitrite, and nitrate derivatives of MMH and UDMH, not considered previously, and gas-phase standard enthalpy of formation of dimethyltetrazane compounds. These data are obtained by using two ab initio methods, specifically derived and validated for this purpose, one for compounds containing NO$_2$, ONO, ONO$_2$ groups and one for general organic compounds.

2 Computational Details

The gas-phase standard enthalpy of formation of molecule j at 298.15 K can be determined from the following equation:

$$\Delta_f H^0_{298.15K(g)} = 2625.5 \times \left(E_j + ZPE_j + \text{thermal corrections} + \sum_i \alpha_i c_i^* \right)$$

where α_i is the number of atoms i in molecule j and c_i^* the atomic correction for atom i. E_j and ZPE_j denote, respectively, the absolute electronic energy and zero-point energy, calculated using the Gaussian 98W [14] and Gaussian 03 [15] softwares. The units are Hartree molecule^{-1} for E_j, ZPE_j and thermal corrections, and Hartree atom^{-1} for c_i^*, whereas $\Delta_f H^0_{298.15K(g)}$ is in kJ mol^{-1}. Two classes of compounds are considered in this study: C/H/N/O compounds and C/H/N compounds. The method established and validated for nitroso, nitro, nitrite, and nitrate compounds, i.e. C/H/N/O compounds, is described in Osmont et al. [16]. The method established and validated for tetrazanes, i.e. C/H/N compounds, is described in Osmont et al. [17, 18].

3 Results

Experimental difficulties in isolating these compounds for calorimetric studies are substantial, and therefore estimation methods have to be used. Such methods can be more or less sophisticated. In this study, we used two ab initio methods with empirical atomic corrections. The details of these methods are beyond the scope of this paper. One of these methods was specifically established and validated with experimental data known on nitro, nitrite, and nitrate compounds. This method was derived with data from 28 compounds and validated with 16 compounds. The average absolute deviation between experiments and calculations is 7.1 kJ mol^{-1} for the derivation set and 10.0 kJ mol^{-1} for the validation set. Table 1 gives the comparison between calculated and experimental gas-phase standard enthalpies of formation at 298.15 K for some compounds included in the derivation and validation datasets. The agreement between experiments and calculations is good. The average absolute deviation for this method, in general, is expected to be ± 13 kJ mol^{-1}. In Table 1, the average absolute deviation is 5.4 kJ mol^{-1} for the nitrite compounds, 8.8 kJ mol^{-1} for the nitro compounds and 11.3 kJ mol^{-1} for the nitrate com-

Appendix

Table 1. Comparison between experimental and calculated (within parenthesis) gas-phase standard enthalpy of formation at 298.15 K for nitrite, nitro, and nitrate compounds from the validation database. Units are kJ mol^{-1}.

-X	-ONO	-NO$_2$	-ONO$_2$
CH$_3$X	-65.3 (-65.3)	-80.7 (-82.0)	-122.2 (-129.3)
C$_2$H$_5$X	-108.4 (-102.9)	-102.5 (-117.1)	-154.8 (-166.5)
C$_3$H$_7$X	-118.8 (-128.9)	-124.7 (-138.5)	-174.0 (-187.9)
CH$_3$-CHX-CH$_3$	-133.5 (-141.0)	-140.2 (-150.2)	-190.8 (-202.5)
(CH$_3$)$_3$C-X	-171.5 (-167.4)	-177.0 (-180.7)	No experimental data

Table 2. Calculated gas-phase standard enthalpies at 298.15 K for nitroso, nitrite, nitro, and nitrate derivatives of MMH and UDMH. Units are kJ mol^{-1}.

-X	-NO	-ONO	-NO$_2$	-ONO$_2$
CH$_3$-NH-NH-X	197.9	173.6	102.1	142.3
CH$_3$-NX-NH$_2$	158.2	173.6	95.8	113.8
CH$_3$-NH-NX$_2$	342.7	292.0	183.8	172.4
CH$_3$-NX-NH-X	278.7	284.9	143.9	167.4
CH$_3$-NX-NX$_2$	427.6	387.0	247.7	232.6
(CH$_3$)$_2$-N-NH-X	174.9	187.9	103.8	123.8
(CH$_3$)$_2$-N-NX$_2$	319.2	288.3	182.0	177.0

Table 3. Gas-phase standard enthalpy of formation at 298 K of nitro and nitrite derivatives of MMH calculated by McQuaid et al. [12, 13]. Units are kJ mol^{-1}.

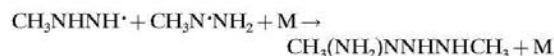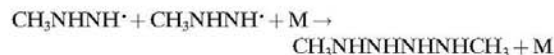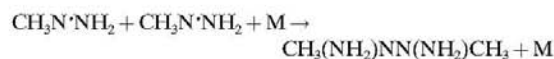| -X	-ONO	-NO$_2$
CH$_3$-NX-NH$_2$	161.1	101.3

Table 4. Gas-phase standard enthalpy of formation at 298 K of hydrazine, MMH, and UDMH calculated by using a ab initio method developed for this study. Units are kJ mol^{-1}.

Compound	Method used here	Experimental data
Hydrazine	95.4	95.4
MMH	93.3	94.1

Table 5. Gas-phase standard enthalpy of formation at 298 K of three dimethyltetrazanes by using a ab initio method developed for this study. Units are kJ mol^{-1}.

Compound	Method used here	Experimental data
CH$_3$(NH$_2$)NN(NH$_2$)CH$_3$	269.4	-
CH$_3$NHNHNHNHCH$_3$	258.6	-
CH$_3$(NH$_2$)NNHNHCH$_3$	262.3	-

pounds. It is to be noted that experimental determination is often unique and therefore experimental uncertainties are often underestimated. The same method, once applied to nitroso, nitro, nitrite, and nitrate compounds derived from MMH and UDMH, leads to data given in Table 2. McQuaid et al. [12, 13] used another ab initio method to compute the gas-phase standard enthalpy of formation of some of the CH$_3$-NX-NH$_2$ species given in Table 2. Comparisons of methods are always interesting especially when no experimental data are available. Their results are given in Table 3 for two of the 28 compounds presented in Table 2. Results given in Tables 2 and 3 are consistent for the nitro and nitrite compounds considered. Therefore, the data presented for 26 remaining compounds presented in Table 2 can be considered to be reliable. These results, and the reappraisal of some thermodynamic data, may help to explain hypergolic ignition. All the compounds in Table 2 are endothermic compounds, i.e. their enthalpies of formation are positive. Such compounds are able to decompose exothermically under thermal stress and this may be of interest to explain ignition or reactivity characteristics and to interpret hard start phenomenon observed occasionally in engines using NTO/MMH.

Another theoretical method specifically devoted to general organic compounds not containing NO, NO$_2$, ONO, and/or ONO$_2$ groups was then used to compute the thermochemistry of dimethyltetrazanes. These compounds

are formed through the termolecular recombination of two methylhydrazyl radicals, namely CH$_3$N·NH$_2$ and CH$_3$NHNH·. Their termolecular recombination reactions lead to three different dimethyltetrazanes according to:

$$CH_3N\cdot NH_2 + CH_3N\cdot NH_2 + M \rightarrow CH_3(NH_2)NN(NH_2)CH_3 + M$$

$$CH_3NHNH\cdot + CH_3NHNH\cdot + M \rightarrow CH_3NHNHNHNHCH_3 + M$$

$$CH_3NHNH\cdot + CH_3N\cdot NH_2 + M \rightarrow CH_3(NH_2)NNHNHCH_3 + M$$

The agreement between experiments and calculations is shown in Table 4 for hydrazine and MMH. Table 5 gives the calculated data for the three dimethyltetrazanes given above. The formation of these tetrazanes is exothermic and these compounds are endothermic, i.e. they can decompose exothermically. These species can play a role in ignition and this role needs to be further studied.

4 Conclusion

Protocols have been derived and validated for predicting the thermodynamic data needed for thermochemical calcu-

Appendix

lations and for building detailed chemical kinetic models to simulate hypergolic ignition and combustion. The level of theory, hybrid density functional theory with a modest basis set, plus empirical corrections, is found appropriate for the current state of knowledge (quite minimal) of their thermochemistry. This paper provides thermochemical data for 31 molecules potentially formed during the MMH/NTO reactivity. No experimental data are available for these compounds. The model previously proposed to explain hypergolic NTO/MMH ignition can be improved, as can almost all kinetic models. Detailed kinetic models developed for mixtures easier to study, and therefore intensively studied, such as premixed methane/air or hydrogen/air, have been continuously improved over the past 50 years, and new models have been proposed in recent years to explain ignition characteristics of these mixtures. Therefore, complementary studies need to be performed for the complex MMH/NTO combustion chemistry. The impact of the thermochemistry proposed in this study on the predictions of the MMH/NTO detailed kinetic model must be examined. Alternative reaction paths also need to be considered. The development of visualization techniques and of new analytical techniques, along with the development and application of methods for calculating the thermochemistry of reactants, products, and intermediate species should lead in the near future to a better understanding of the features of hypergolic ignition and to new tools for the design and screening of new hypergolic fuels.

5 References

[1] A. J. Alfano, J. D. Mills, G. L. Vaghjiani, Highly Accurate Ignition Delay Apparatus for Hypergolic Fuel Research, *Rev. Sci. Instrum.* **2006**, *77*, 045109.

[2] L. Catoire, N. Chaumeix, S. Pichon, C. Paillard, Visualizations of Gas-Phase NTO/MMH Reactivity, *J. Propul. Power* **2006**, *22*, 120.

[3] L. Catoire, N. Chaumeix, C. Paillard, Chemical Kinetic Model for Monomethylhydrazine/Nitrogen Tetroxide Gas-Phase Combustion and Hypergolic Ignition, *J. Propul. Power* **2004**, *20*, 87.

[4] L. Catoire, X. Bassin, G. Dupré, C. Paillard, Experimental Study and Kinetic Modeling of the Thermal Decomposition of Gaseous Monomethylhydrazine. Application to Detonation Sensitivity, *Shock Waves* **1996**, *6*, 139.

[5] L. Catoire, T. Ludwig, X. Bassin, G. Dupré, C. Paillard, Kinetic Modeling of the Ignition Delays in Monomethylhydrazine/Oxygen/Argon Mixtures, *27th International Symposium on Combustion*, Boulder, Colorado, USA **1998**, *27*, p. 2359.

[6] L. Catoire, T. Ludwig, G. Dupré, C. Paillard, Kinetic Modelling of the Ignition Delays in MMH/Hydrogen/Oxygen/Argon Gaseous Mixtures, *J. Aerospace Eng.* **1998**, *212*, 393.

[7] H. Sun, C. K. Law, Thermochemical and Kinetic Analysis of the Thermal Decomposition of Monomethylhydrazine: An Elementary Reaction Mechanism, *J. Phys. Chem. A* **2007**, *111*, 3748.

[8] C. Nonnenberg, I. Frank, T. M. Klapötke, Ultrafast Cold Reactions in the Bipropellant Monomethylhydrazine/Nitrogen Tetroxide: CPMD Simulations, *Angew. Chem. Int. Ed.* **2004**, *43*, 4586.

[9] I. Frank, A. Hammerl, T. M. Klapötke, C. Nonnenberg, Processes during the Hypergolic Ignition between Monomethylhydrazine (MMH) and Dinitrogen Tetroxide (N2O4) in Rocket Engines, *Propellants, Explos., Pyrotech.* **2005**, *30*, 44.

[10] L. Catoire, M. T. Swihart, Thermochemistry of Species Produced from Monomethylhydrazine in Propulsion and Space-Related Applications, *J. Propul. Power* **2002**, *18*, 1242.

[11] M. A. Bohn, T. M. Klapötke, DFT and G2MP2 Calculations of the N-N Bond Dissociation Enthalpies and Enthalpies of Formation of Hydrazine, Monomethylhydrazine and Symmetrical and Unsymmetrical Dimethylhydrazine, *Z. Naturforsch., B: Chem. Sci.* **2004**, *59*, 148.

[12] M. J. McQuaid, W. R. Anderson, A. J. Kotlar, M. J. Nusca, Y. Ishikawa, Computational Characterization of Reactions Employed to Model Monomethylhydrazine/Inhibited Red Fuming Nitric Acid Chemical Kinetics, *Proceedings of the 6th International Symposium on Special Topics in Chemical Propulsion* (6-ISICP), Santiago, Chile, March 8–11, **2005**.

[13] M. J. McQuaid, Y. Ishikawa, H-Atom Abstraction from CH₃NHNH₂ by NO₂: CCSD(T)/6-311++G(3df,2p)//MPWB1K/6-31+G(d,p) and CCSD(T)/6-311+G(2df,p)//CCSD/6-31+G(d,p) Calculations, *J. Phys. Chem. A* **2006**, *110*, 6129.

[14] Gaussian 98, Revision A.6, M. J. Frisch, G. W. Trucks, H. B. Schlegel, G. E. Scuseria, M. A. Robb, J. R. Cheeseman, V. G. Zakrzewski, J. A. Montgomery, Jr., R. E. Stratmann, J. C. Burant, S. Dapprich, J. M. Millam, A. D. Daniels, K. N. Kudin, M. C. Strain, O. Farkas, J. Tomasi, V. Barone, M. Cossi, R. Cammi, B. Mennucci, C. Pomelli, C. Adamo, S. Clifford, J. Ochterski, G. A. Petersson, P. Y. Ayala, Q. Cui, K. Morokuma, D. K. Malick, A. D. Rabuck, K. Raghavachari, J. B. Foresman, J. Cioslowski, J. V. Ortiz, B. B. Stefanov, G. Liu, A. Liashenko, P. Piskorz, I. Komaromi, R. Gomperts, R. L. Martin, D. J. Fox, T. Keith, M. A. Al-Laham, C. Y. Peng, A. Nanayakkara, C. Gonzalez, M. Challacombe, P. M. W. Gill, B. Johnson, W. Chen, M. W. Wong, J. L. Andres, C. Gonzalez, M. Head-Gordon, E. S. Replogle, J. A. Pople, Gaussian, Inc., Pittsburgh, PA, **1998**.

[15] Gaussian 03, Revision D.01, M. J. Frisch, G. W. Trucks, H. B. Schlegel, G. E. Scuseria, M. A. Robb, J. R. Cheeseman, J. A. Montgomery, Jr., T. Vreven, K. N. Kudin, J. C. Burant, J. M. Millam, S. S. Iyengar, J. Tomasi, V. Barone, B. Mennucci, M. Cossi, G. Scalmani, N. Rega, G. A. Petersson, H. Nakatsuji, M. Hada, M. Ehara, K. Toyota, R. Fukuda, J. Hasegawa, M. Ishida, T. Nakajima, Y. Honda, O. Kitao, H. Nakai, M. Klene, X. Li, J. E. Knox, H. P. Hratchian, J. B. Cross, V. Bakken, C. Adamo, J. Jaramillo, R. Gomperts, R. E. Stratmann, O. Yazyev, A. J. Austin, R. Cammi, C. Pomelli, J. W. Ochterski, P. Y. Ayala, K. Morokuma, G. A. Voth, P. Salvador, J. J. Dannenberg, V. G. Zakrzewski, S. Dapprich, A. D. Daniels, M. C. Strain, O. Farkas, D. K. Malick, A. D. Rabuck, K. Raghavachari, J. B. Foresman, J. V. Ortiz, Q. Cui, A. G. Baboul, S. Clifford, J. Cioslowski, B. B. Stefanov, G. Liu, A. Liashenko, P. Piskorz, I. Komaromi, R. L. Martin, D. J. Fox, T. Keith, M. A. Al-Laham, C. Y. Peng, A. Nanayakkara, M. Challacombe, P. M. W. Gill, B. Johnson, W. Chen, M. W. Wong, C. Gonzalez, J. A. Pople, Gaussian, Inc., Wallingford, CT, **2004**.

[16] A. Osmont, L. Catoire, I. Gökalp, V. Yang, Ab Initio Quantum Chemical Predictions of Enthalpies of Formation, Heat Capacities, and Entropies of Gas-Phase Energetic Compounds, *Combust. Flame* **2007**, *151*, 262.

[17] A. Osmont, L. Catoire, I. Gökalp, Thermochemistry of Methyl and Ethyl Esters From Vegetable Oils, *Int. J. Chem. Kinet.* **2007**, *39*, 481.

[18] A. Osmont, L. Catoire, I. Gökalp, M. T. Swihart, Thermochemistry of C-C and C-H Bond Breaking in Fatty Acid Methyl Esters, *Energy Fuels* **2007**, *21*, 2027.

AFRL-RZ-ED-TR-2010-0048
Primary Distribution of this Report:

AFRL/RZSP   (3 CD + 2 HC)
Dr. Ghanshyam Vaghjiani
10 E. Saturn Blvd.
Edwards AFB CA 93524-7680

AFRL/RZSP   (1 HC)
Record Custodian
10 E. Saturn Blvd.
Edwards AFB CA 93524-7680

AFRL/RZ Technical Library (2 CD + 1 HC)
6 Draco Drive
Edwards AFB CA 93524-7130

Chemical Propulsion Information Analysis Center
Attn: Tech Lib (Mary Gannaway) (1 CD)
10630 Little Patuxent Parkway, Suite 202
Columbia MD 21044-3200

Defense Technical Information Center
(1 Electronic Submission via STINT)
Attn: DTIC-ACQS
8725 John J. Kingman Road, Suite 94
Ft. Belvoir VA 22060-6218